

# Single and Competitive Protein Sorption at Soft Polymeric Interfaces

vorgelegt von  
Diplom-Chemiker  
Michael Oberle  
geb. in Frankfurt am Main

von der Fakultät II - Mathematik und Naturwissenschaften  
der Technischen Universität Berlin  
zur Erlangung des akademischen Grades  
Doktor der Naturwissenschaften  
- Dr. rer. nat. -

genehmigte Dissertation

Promotionsausschuss:

Vorsitzender: Prof. Dr. Thorsten Ressler

Berichter/Gutachter: Prof. Dr. Matthias Ballauff

Berichter/Gutachter: Prof. Dr. Regine von Klitzing

Berichter/Gutachter: Prof. Dr. Gerhard H. Findenegg

Tag der wissenschaftlichen Aussprache: 6. Juni 2016

Berlin 2016



*«Die Fragen sind es, aus denen das, was bleibt, entsteht»  
Erich Kästner*



*Meiner Mutter*



Spherical nanoparticles with polymer coatings or entirely composed of polymers have their own technological importance as drug carriers. These nanostructures can be constructed as stimuli-responsive devices that deliver a drug in spatial-, temporal- and dosage-controlled fashion. The nanoparticles rapidly form a protein corona as soon as they get immersed in biological fluids like blood or plasma. Ultimately, the composition of the protein corona will modify the physical/chemical properties of the nanoparticle and will determine its biological fate. The fact is that competitive and cooperative adsorption of different proteins play a pivotal role in this process.

In this thesis charged and uncharged core-shell microgels were used as model systems to study single and competitive protein adsorptions. The microgels consist of a solid polystyrene core, a highly swollen poly-(N-isopropylacrylamide) shell and defined amounts of acrylic acid to introduce charge. Experimental data for the adsorption of single type proteins were obtained by Isothermal Titration Calorimetry (ITC). The challenges of using ITC as a method to characterize protein nanoparticle interactions are discussed. Finally, the evaluation of ITC data with the Langmuir model and a cooperative binding model are compared. In contrast to the Langmuir model this model offers a more quantitative interpretation of binding isotherms with the advantage to show more details regarding the driving forces contributing to the adsorption process. In a second part experimental data for the competitive adsorption from binary mixtures were obtained by fluorescence spectroscopy and compared to the predictions from the cooperative binding model. It was demonstrated that for the proteins lysozyme, papain, RNase and cytochrome c the experimental data are in good agreement with the predictions and the expansion to multi-component mixtures is possible.

The remaining parts of the thesis are concerned with the structural properties of the core-shell microgels. For this purpose the polymers were investigated by Atomic Force Microscopy (AFM) and Anomalous Small Angle X-ray Scattering (ASAXS). The AFM images in air revealed a strongly collapsed structure on a silicon surface. Moreover, the adsorption of lysozyme onto the shell of the microgel changed the phase of the AFM signal indicating a change in the mechanical properties. For the measurements in liquid it was shown that the microgels can be attached via electrostatic interactions with a functionalized silicon surface. Upon protein adsorption the shell of the surface-attached microgels began to shrink. For the ASAXS part the Fe-containing protein cytochrome c was adsorbed onto the microgel and analyzed in the energy range of the K-absorption edge of Fe at three different energies. From the pure-resonant scattering contribution the thickness of the protein layer is determined and correlated with the corresponding protein concentration.





Sphärische Nanopartikel mit Polymerbeschichtungen oder vollständig aus Polymeren zusammengesetzte Nanopartikel haben eine große technologische Bedeutung als Trägermaterialien für Medikamente. Diese Nanostrukturen können so konstruiert werden, dass durch einen äußeren Reiz die Wirkstofffreisetzung zeitlich und räumlich kontrolliert erfolgen kann. Ebenso kann über diesen Weg die Dosierung kontrolliert werden. Sobald Nanopartikel mit biologischen Flüssigkeiten wie Blut oder Plasma in Kontakt kommen, bildet sich um diese eine Protein Korona. Die Zusammensetzung der Protein Korona bestimmt jetzt die physikalischen- und chemischen Eigenschaften der Nanopartikel und die Wechselwirkungen mit einem Organismus. In diesem Prozess spielt die kompetitive und kooperative Adsorption verschiedener Proteine eine wichtige Rolle.

In dieser Arbeit wurde die Adsorption von einzelnen Proteinsorten und die kompetitive Adsorption aus Proteinmischungen auf geladene Kern-Schale Mikrogele untersucht. Die Mikrogele bestehen aus einem festen Polystyrolkern, einer stark gequollenen Schale aus Poly-(N-isopropylacrylamide) und definierten Mengen des Copolymers Acrylsäure, welches eine geladene Carboxylgruppe in das Mikrogel einführt. Die Adsorptionsisothermen einzelner Proteinsorten wurden mit der Isothermalen Titrationskalorimetrie (ITC) gemessen. In diesem Zusammenhang wurden die Herausforderungen dieser Methode zur Charakterisierung von Protein-Nanopartikel-Wechselwirkungen diskutiert. Ferner wurde die Auswertung der ITC-Daten mit dem Langmuir-Modell und einem "kooperativen" Bindungsmodell verglichen. Im Gegensatz zum Langmuir-Modell bietet dieses Bindungsmodell eine quantitative Analyse der Bindungsisothermen, mit der Möglichkeit mehr Details zu den treibenden Kräften, die zur Adsorption beitragen, zu verarbeiten. In einem weiteren Teil der Arbeit wurde die kompetitive Adsorption aus binären Proteinmischungen mit Fluoreszenzspektroskopie gemessen und mit Vorhersagen durch das "kooperative" Bindungsmodell verglichen. Es wurde gezeigt, dass die experimentellen Daten für die Proteine Lysozym, Papain, RNase und Cytochrome c in guter Übereinstimmung mit den Vorhersagen sind.

Die weiteren Teile der Dissertation beschäftigen sich mit den strukturellen Eigenschaften der Kern-Schale Mikrogele. Zu diesem Zweck wurden die Polymere mit Rasterkraftmikroskopie (AFM) und anomaler Kleinwinkelröntgenstreuung (ASAXS) untersucht. Die AFM-Bilder in Luft zeigten eine stark zusammengeschrumpfte Struktur auf einer Siliziumoberfläche. Darüber hinaus konnte bei der Adsorption von Lysozym auf die Schale des Mikrogels eine Phasenänderung des AFM-Signals festgestellt werden, welches auf eine Änderung der mechanischen Eigenschaften des Polymers hinweist. Für die AFM Messungen in Flüssigkeit wurde gezeigt, dass die Mikrogele über elektrostatische Wechselwirkungen auf einer funktionalisierten Siliziumoberfläche immobilisiert werden können. Zusätzlich konnte gezeigt werden, dass die Proteinadsorption zu einem Schrumpfen des auf der Oberfläche gebundenen Mikrogels führt.

Für die ASAXS Messungen wurden das eisenhaltige Protein Cytochrom c auf das Mikrogel adsorbiert und die Probe wurde bei drei verschiedenen Energien am Rand der K-Kante von Eisen gemessen. Aus dem Betrag der rein resonanten Streuung der eisenhaltigen Proteins konnte sowohl die Dicke der Proteinschicht ermittelt werden als auch die entsprechende Proteinkonzentration pro Nanopartikel.



# Contents

<b>1</b>	<b>Introduction</b>	<b>1</b>
1.1	Protein Material Interactions . . . . .	1
1.2	Competitive Protein Adsorption and the Protein Corona . . . . .	2
1.3	Non-Competitive Protein Adsorption: The Langmuir Model . . . . .	5
1.4	Competitive Protein Adsorptions: Models . . . . .	7
<b>2</b>	<b>Objective of this Thesis</b>	<b>8</b>
<b>3</b>	<b>Fundamentals and Theory</b>	<b>9</b>
3.1	Stimuli-Sensitive Microgels - Model Systems for Protein Material Interactions . . . . .	9
3.1.1	Introduction . . . . .	9
3.1.2	Poly-NIPAM based Core-Shell Microgels . . . . .	10
3.1.3	Interactions of Proteins with Poly-NIPAM based Core-Shell Microgels . . . . .	11
3.1.4	Swelling behaviour of Poly-NIPAM based Core-Shell Microgels . . . . .	14
3.1.5	Interactions of Microgels with Surfaces . . . . .	14
3.2	Characterization of Single Protein Adsorptions to Core-Shell Microgels . . . . .	15
3.2.1	Isothermal Titration Calorimetry (ITC) . . . . .	15
3.2.2	Evaluation of ITC data . . . . .	17
3.2.3	Problems of ITC . . . . .	19
3.2.4	Small Angle Scattering (SAS) . . . . .	22
3.2.4.1	Theory of SAS . . . . .	23
3.2.4.2	ASAXS . . . . .	25
3.3	Characterization of Competitive Protein Adsorptions to Microgels . . . . .	26
3.3.1	Fluorescence Spectroscopy . . . . .	26
3.4	The Cooperative Binding Model (CB-model) . . . . .	27
3.4.1	Derivation of the Cooperative Binding Model . . . . .	28
3.4.1.1	Electrostatic Interactions . . . . .	30
3.4.1.2	Pair Interactions . . . . .	32
3.4.1.3	Volume Effects . . . . .	32
<b>4</b>	<b>Results and Discussion</b>	<b>34</b>
4.1	Binding Isotherms of Core-Shell Microgels to Single Proteins (ITC) . . . . .	34
4.1.1	Langmuir Fits . . . . .	34

4.1.2	Cooperative Binding Model Fits . . . . .	40
4.2	Competitive Adsorption . . . . .	43
4.3	Cytochrome c Adsorption as measured by Anomalous Small Angle X-ray Scattering (ASAXS) . . . . .	46
4.4	Adsorption of Lysozyme as measured by AFM . . . . .	50
<b>5</b>	<b>Summary and Outlook</b>	<b>53</b>
<b>6</b>	<b>Materials and Methods</b>	<b>55</b>
6.1	Materials . . . . .	55
6.2	Proteins . . . . .	55
6.3	Synthesis and Characterization of Core-Shell Microgels . . . . .	55
6.3.1	Synthesis of the Polystyrene Cores . . . . .	55
6.3.2	Synthesis of the Shell . . . . .	56
6.3.3	Transmission Electron Microscopy (TEM) . . . . .	57
6.3.4	Conductometric and Potentiometric Titrations . . . . .	58
6.3.5	Dynamic Light Scattering (DLS) . . . . .	58
6.4	Isothermal Titration Calorimetry . . . . .	59
6.5	Fluorescence Spectroscopy . . . . .	60
6.5.1	Labeling with Fluorescein isothiocyanate . . . . .	60
6.5.1.1	Experimental Setup for a Binary Protein Mixture . . . . .	62
6.6	Atomic Force Microscopy . . . . .	62
6.6.1	Substrate Preparation . . . . .	62
6.6.2	AFM Measurements and Analysis . . . . .	63
6.7	SAXS . . . . .	63
6.8	ASAXS . . . . .	63
6.8.1	Sample Preparation . . . . .	63
6.8.2	Technical Details . . . . .	63
<b>7</b>	<b>Appendix</b>	<b>64</b>
7.1	Frequently used variables for the derivation of the Cooperative Binding Model . . . . .	64
<b>8</b>	<b>Bibliography</b>	<b>65</b>
<b>9</b>	<b>List of Abbreviations</b>	<b>77</b>
<b>10</b>	<b>List of Figures</b>	<b>79</b>
<b>11</b>	<b>List of Tables</b>	<b>81</b>
<b>12</b>	<b>List of Publications and Presentations</b>	<b>82</b>



# 1 Introduction

## 1.1 Protein Material Interactions

The effects of protein material interactions are of central importance in different fields of nanotechnology. The design of non-fouling surfaces, for example, is equally interesting for maritime industries and the development of new nano-scaled laboratory devices (see Figure 1.1 a and Figure 1.1 b). In nanomedicine controlled drug release by nanoparticles requires no or little interference by unspecific protein interactions (see Figure 1.1 c). There are also not fewer important applications where a defined protein material interaction is necessary like the immobilization of proteins as catalysts or the purification of proteins by chromatography.<sup>1</sup> The goal of this section is to give a brief overview into this topic always keeping in mind how protein material interactions affect previously mentioned fields and that it remains a challenge to understand and control these interactions better.

Biofouling is defined as an undesirable accumulation of microorganisms on wetted artificial surfaces and represents a major economic issue regarding maritime industries.<sup>2</sup> In general, biofouling will increase the roughness of a surface leading to a higher frictional resistance. Thus, considering ships biofouling causes speed reduction, higher fuel consumption and maintenance costs. A common practice to suppress biofouling involves the use of toxic biocides. However, there are also different strategies to develop surface modifications, which are more environmentally friendly.<sup>3</sup> It is assumed, that in the first stage of biofouling a conditioning film mainly comprised of proteins adsorbs to the surface and catalyzes the attachment of microorganisms, which finally cause macrofouling of the surface.<sup>4</sup>

In the health sector advances in nanotechnology had opened a variety of nanomaterials to improve diagnosis, prevention and treatment of diseases. These nanomaterials have at least one dimension in the range of 1 to 100 nm and can be considered as intermediates between small molecules and bulk materials. Compared to their bulk material counterparts, the physio-chemical properties like size, surface charge, stability and solubility are crucial for their physiological interactions. Biomaterials, coated medical devices, and nanoparticles have enormous potential to improve medical treatments, but can cause adverse or even toxic side effects. It is a well-known fact, that implanted and blood-contacted biomaterials can induce adverse side effects like inflammation,<sup>5,6</sup> thrombosis<sup>7</sup> and infections.<sup>8</sup> These effects can be traced back to a quickly forming protein layer on the biomaterial. Furthermore, it is known that phagocytes interact with the adsorbed proteins rather than with the material itself.<sup>9</sup> It was also shown that formation of such a layer can limit the performance of so called protein micro-arrays.<sup>10</sup> These micro-arrays are supposed to detect analytes in very low concentrations from complex mixtures, such as serum or blood. Adsorption of other proteins than the antibodies used for detection will limit the sensitivity of such

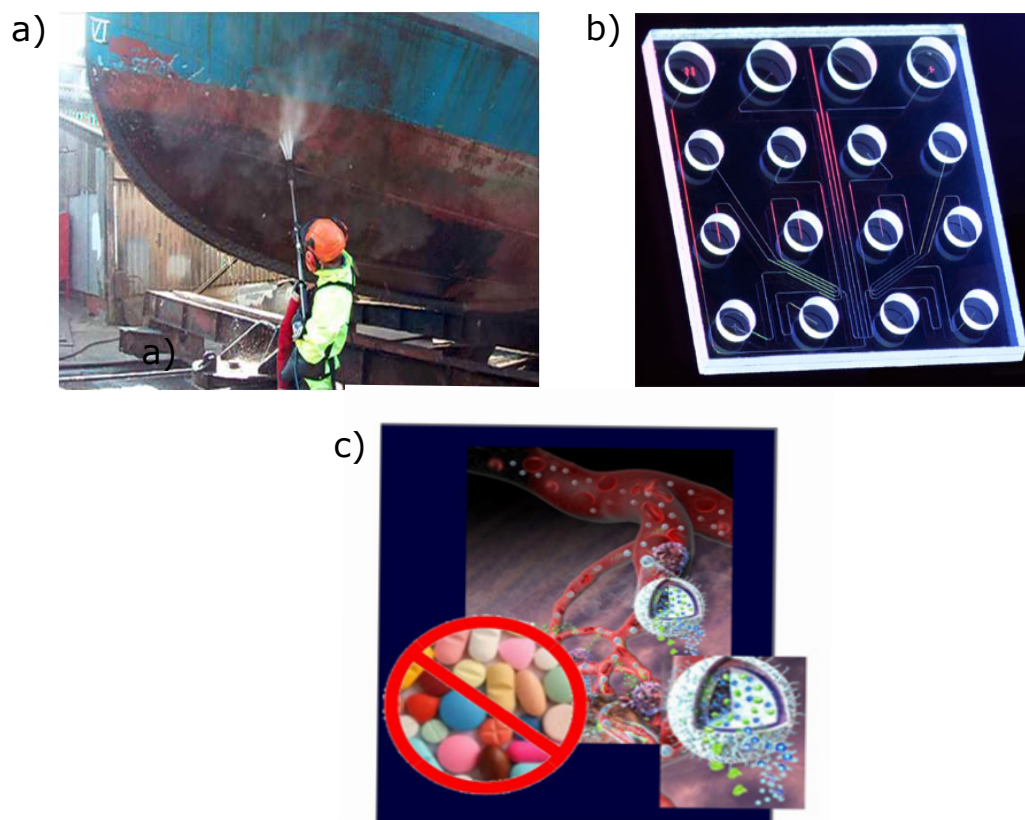


Figure 1.1: Protein adsorptions occurring in different technological fields: a) Ship hull covered with a biofilm. Here the biofilm is removed by an ultra-high pressure water jet. b) A lab on chip device using microfluidic technology. c) Scheme of a spherical nanoparticle loaded with a drug. In comparison to drugs in tablet form, nanoparticles offer the possibility of controlled and targeted drug release. Pictures reprinted from <http://www.hydroblasting.co.uk/hydroblasting-services/anti-fouling.html> <https://chemeng.adelaide.edu.au/losic-group/research/nanomedicine/> <http://www.bioprocessonline.com>

micro-arrays and are one of the key factors that control the limit-of-detection of the analyte. Thus, a better understanding of the protein adsorption process will help to improve diagnostics with such micro-arrays.

## 1.2 Competitive Protein Adsorption and the Protein Corona

The field of competitive protein adsorption has emerged in the 1960s by seminal contributions by Vroman and Adam, who investigated the adsorption of plasma proteins onto metal oxides, silicon, and polymer surfaces.<sup>11–14</sup>

It was found that fibrinogen adsorbs preferentially at short to intermediate contact time and then is replaced by a number of different proteins from blood serum like kinogen or factor XII sequentially. Sequential adsorption is not limited to fibrinogen and can be regarded as a general trend for many other proteins.<sup>15,16</sup> In general, under equilibrium conditions proteins with higher mobility arrive first at the surface and are later sequentially replaced by less mobile proteins that have a higher affinity for the surface.

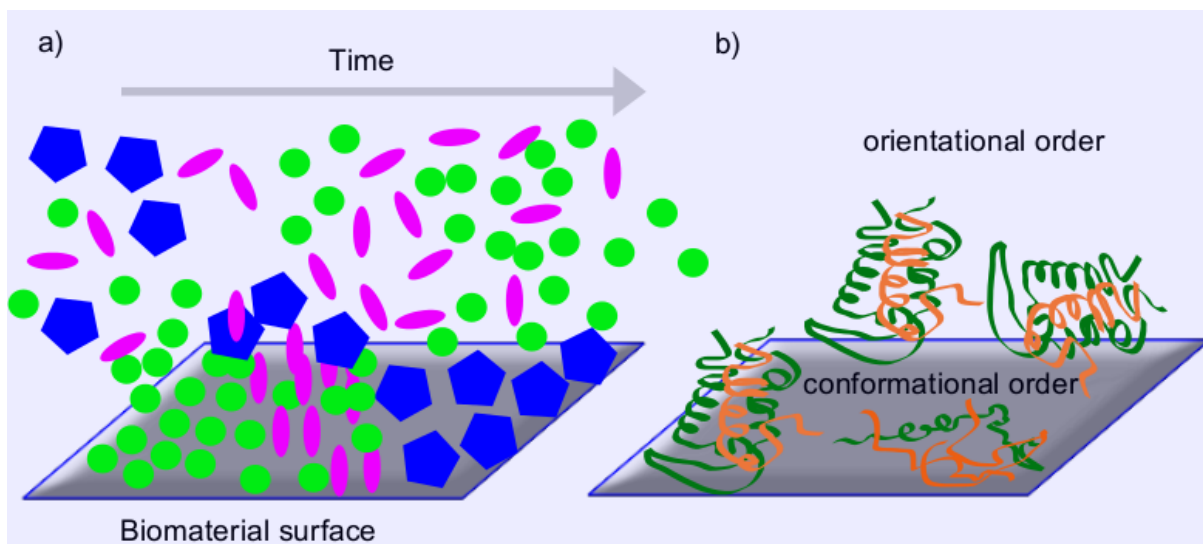


Figure 1.2: a) Illustration of the Vroman effect. Proteins which are present in high concentrations in the medium adsorb first on the surface and get replaced over time by proteins with lower abundance in the medium but higher affinity to the surface. b) Illustration of orientation and conformational changes of proteins which can occur during adsorption.

In Figure 1.2 a the sequential replacement of proteins over time, commonly termed as "Vroman effect", is illustrated. Figure 1.2 b illustrates how proteins adsorbed at surfaces can undergo conformational and orientational changes. The structural perturbations are dependent on the nature of the surface. For example, Norde and Giacomelli showed that BSA completely regains its native structure and stability after being replaced from a hydrophilic surface but not in the case of a hydrophobic surface.<sup>17</sup> On the other hand, lysozyme seems to be able to regain its native configuration even after desorption from hydrophobic teflon surfaces.<sup>18</sup> These results show that the mechanisms behind competitive proteins adsorption are not fully understood yet.

Competitive protein adsorption can be measured by different techniques including surface plasmon resonance,<sup>19</sup> atomic force microscopy,<sup>20</sup> quartz crystal microbalance,<sup>21</sup> ellipsometry,<sup>20,22</sup> reflectometric interference spectroscopy, and total internal reflection fluorescence spectroscopy.<sup>22,23</sup> Malmsten et al. investigated the adsorption of single proteins and the competitive adsorption of ternary protein mixtures on polymer surfaces.<sup>22</sup> For hydrophobic surfaces the protein layer was dominated by human serum albumin (HSA) and human IgG and no or little exchange was found. In contrast on charged hydrophilic surfaces human fibrinogen (Fgn) was preferentially adsorbed. Huang et al. investigated the adsorption of ternary solutions composed of the same plasma proteins on planar surfaces composed of poly-(carbonate-urethane) and polystyrene (PS).<sup>24</sup> They found that poly-(carbonate-urethane) has a preferential adsorption for HSA compared to PS. Riedel et al. looked into the anti-fouling properties of functionalized poly(ethylene glycol)-based (PEG) surfaces against human blood plasma proteins using LC-MS/MS analysis.<sup>25</sup> It was found that only a few plasma proteins including HSA were ubiquitous on the PEG surfaces. Furthermore, HSA was not adsorbed from single protein solutions but adsorption takes place from blood plasma, which indicates that HSA adsorption is mediated by some other plasma proteins. Mohr et al. analyzed the aggregation of polystyrene-based spherical nanoparticles and their interaction



with blood plasma by dynamic light-scattering techniques and LC-MS. Their experiments indicate that the composition of the protein layer determines their aggregation behaviour and their organ distribution *in vivo*.<sup>26</sup>

Up to now, much work has been devoted to the synthesis of nanomaterials and to their interaction with single protein types. However, biological media are multicomponent mixtures i.e. they usually contain more than one type of protein. For example, in human serum the most abundant proteins, albumin (70%), IgG (14%), transferrin (5.7%), fibrinogen (2.8%), and  $\alpha$ -antitrypsin (0.7%), cover 93% of the whole protein mass. In addition to these other proteins which function as enzymes and hormones are present. In such a complex mixture competitive and/or cooperative adsorption necessarily need to be considered. For spherical nanoparticles the competitive and/or cooperative adsorptions of different protein types will lead to the formation of a protein corona. The composition of the protein corona will determine the physical and chemical properties of the nanoparticle and in a biological medium will determine its biological fate in terms of cellular response, biodistribution, clearance and toxicity.<sup>9,26–34</sup> Figure 1.3 a shows schematically how a spherical nanoparticle encased with a protein corona interacts at a cellular level with a membrane. The formation of a protein corona is a dynamic process and the composition of proteins will evolve with time (see Figure 1.3b) in analogy to the Vroman effect for flat surfaces (see section 1.2). Although at some point equilibrium might be reached, i.e. association and

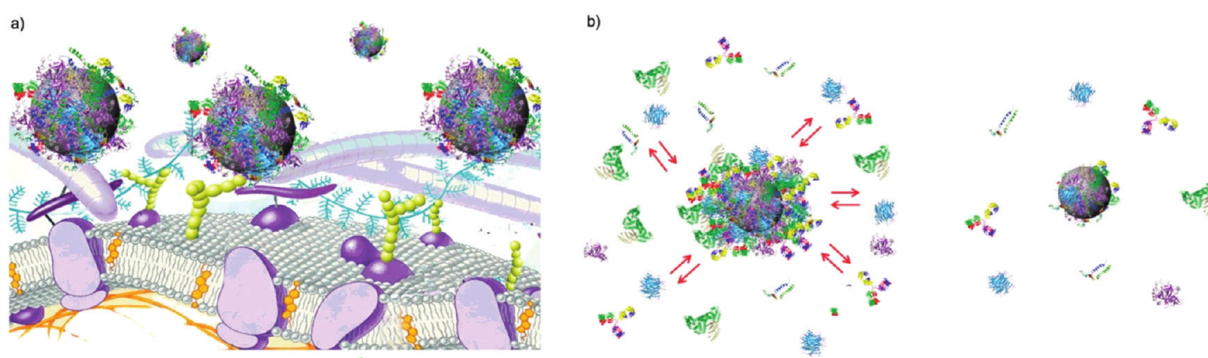


Figure 1.3: a) Sketch of spherical nanoparticle covered with a protein corona interacting with a cellular membrane. Composition of the corona will determine the biological identity of the nanoparticle. b) Sketch representing the dynamic nature of the protein corona. Higher affinity proteins will replace previously adsorbed proteins with time. Reprinted from Walczyk et al.<sup>33</sup>

dissociation rates have become equal, the corona will again change its composition if the nanoparticle is immersed in other fluids or compartments. Hence, the time evolution of the corona formation and also the time-scales on which the proteins adsorb and exchange is crucial to predict the biological response and need be considered in order to get a clear picture of the entire process.

Recently some groups subdivided the corona into a "hard" and "soft" corona.<sup>31,35,36</sup> The "hard" corona is mainly composed of proteins with high binding affinities that are tightly bound to the nanoparticle, while the "soft" corona consists of proteins which are loosely bound to the NPs surface. Moreover, it is conceivable that "hard" corona proteins can mediate binding of other proteins via protein-protein interactions. In practice, the majority of published studies investigate the composition of the corona by

employing washing or centrifugation steps and analyzing the residual protein concentration (solution depletion technique). With this technique only tightly and rather irreversibly bound proteins can be detected. Up to now, there are only few analytical methods like dynamic light scattering (DLS) or fluorescence correlation spectroscopy (FCS) which can measure the dynamic nature of the protein corona especially in a complex biological medium.<sup>26,37,38</sup> Therefore, the detection and discrimination of "hard" and "soft" corona proteins is a difficult task.

Nanoparticles can induce conformational changes to the adsorbed protein molecules which may affect its function. Deng et al. recently showed that negatively charged poly(acrylic acid)-conjugated gold nanoparticles bind to fibrinogen.<sup>39</sup> By unfolding the protein an entire signal cascade is triggered, which ultimately releases cytokines and promotes the inflammatory reaction. Hoshino et al. synthesized polymer nanoparticles that bind venomous molecules and neutralize their function.<sup>40</sup> However, the specificity and intended performance of these particles *in vivo* was suppressed by formation of an unspecific protein layer composed of plasma proteins. Salvati et al. showed that the targeting ability of a transferrin functionalized nanoparticle is lost as soon as the particle is immersed in a complex biological environment due to the interaction with the host proteins.<sup>41</sup> As a consequence, many ways have been investigated to prevent the formation of a protein corona in order to maintain the nanoparticles "bare" identity. One classical approach is the use of a non charged poly(ethylene glycol) (PEG) polymer.<sup>42,43</sup> However, it has been reported that PEG-functionalized NPs can interact with certain plasma proteins.<sup>44</sup> Another approach to suppress corona formation is the incorporation of zwitterion functionalities onto the NPs surface.<sup>45,46</sup> Moyano et al. demonstrated that sulfobetaine headgroups engineered with a short oligo(ethylene glycol) spacer on a Au NP do not adsorb proteins at moderate serum protein concentrations nor do they form a corona at physiological serum conditions.<sup>47</sup> The examples illustrate that engineering such polymer coated NPs protein repellent requires an in depth understanding of the driving forces of competitive and/or cooperative adsorptions. Driving forces, for instance, can be hydrophobic and electrostatic in nature and strongly depend on external conditions like pH, ionic strength and temperature.

### 1.3 Non-Competitive Protein Adsorption: The Langmuir Model

The analysis of protein adsorption usually begins by measuring the adsorption isotherm. To construct such an isotherm, the amount of protein adsorbed on a surface or onto a NP is plotted as a function of the equilibrium concentration. To obtain the amount of adsorbed protein different techniques like ellipsometry, surface plasmon resonance, fluorescence spectroscopy and isothermal titration calorimetry are available. The solution depletion technique was already described in previous section 1.2 and is one of the simplest methods to study protein adsorption. Ideally, the shape of the adsorption isotherm can then provide information on the thermodynamics of the protein adsorption process by fitting an appropriate adsorption model to the isotherm plot, from which thermodynamic parameters can be derived. There are several models including Langmuir, Freundlich, and Brunauer-Emmett-Teller (BET), each of which is based on a different physical principles and prerequisites to fit the isotherm. Among these models the Langmuir adsorption isotherm provides the simplest and most direct methods to quantify an adsorption

process. The Langmuir model states, that for a binary reaction  $A + B \rightarrow AB$  with the equilibrium binding constant  $K = \frac{[AB]}{[A][B]}$  all adsorption sites are equivalent in terms of their adsorption free energies, which can be calculated from its relationship to  $K$ . The Langmuir equation then relates the fraction of occupied adsorption sites  $\Theta$  to the binding constant  $K$  given by<sup>48</sup>

$$(1.1) \quad K = \frac{\Theta}{(1 - \Theta)c_p}$$

with  $c_p$  corresponding to the equilibrium concentration of protein in solution. For a microgel containing  $N$  adsorption sites,  $\Theta$  is defined as  $N_i/N$ , with  $N_i$  defined as the number of proteins bound per microgel. The Langmuir model assumes no interactions among the adsorbed molecules and most important equilibrium conditions between the amount of protein adsorbed on the surface or nanoparticle and the protein that is free in solution. Figure 1.4 a shows the typical shape of a Langmuir shaped isotherm. Even if

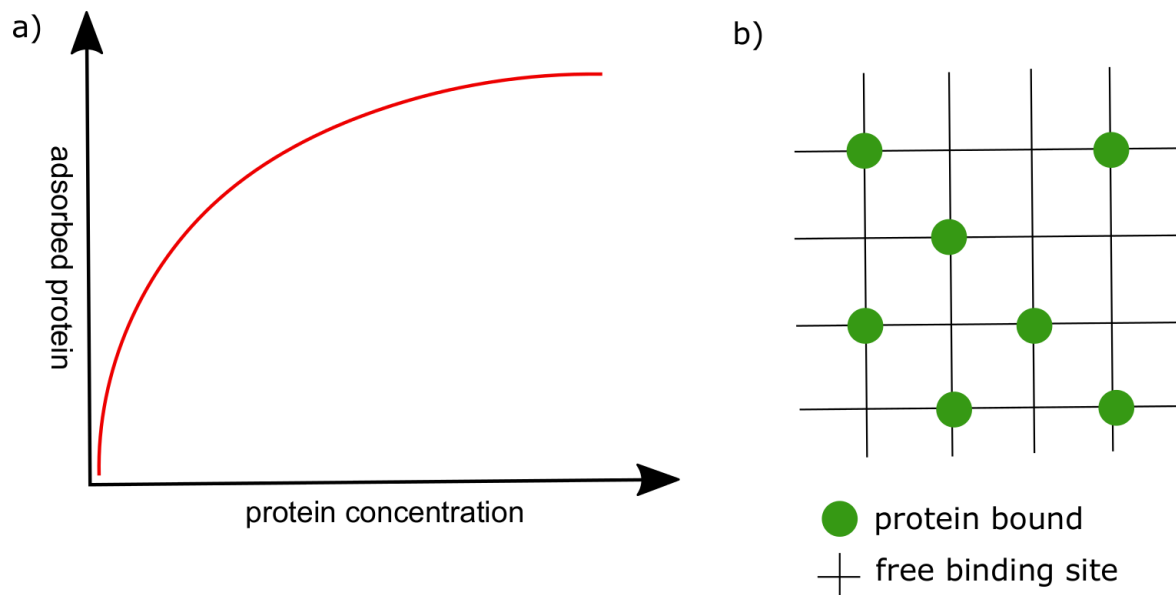


Figure 1.4: a) Scheme of a typical protein adsorption isotherm. b) Protein adsorption to fixed binding sites. See further explanation in the text.

protein adsorption isotherms often give the appearance of having the shape of a Langmuir isotherm, applying a Langmuir fit might often not be the best choice.<sup>49</sup> The parameters obtained from a Langmuir fit are only reliable under equilibrium conditions. However, most experimentally measured protein adsorption isotherms may not represent equilibrium conditions. As a consequence, the equilibrium constant,  $K$ , should rather be interpreted as an "effective" parameter that characterizes the shape of the isotherm and is not necessarily related to the free energy of protein adsorption.<sup>49</sup> Another drawback is the assumption of single, independent binding sites as depicted in Figure 1.4 b. The proteins are confined within their lattice position which is rather not fulfilled in most cases of protein adsorption. Actually, in multi-component mixtures the number of adsorbants (proteins) will vary in size and composition and the binding sites are difficult to define clearly. Moreover, mutual interactions between proteins can induce cooperative adsorption that cannot be treated in terms of single independent binding sites. Thus, with

the Langmuir model is not easy to include cooperative adsorption effects. These effects become very important in protein mixtures where competitive adsorption occurs. Therefore, there are present in all biological fluids.

## 1.4 Competitive Protein Adsorptions: Models

To overcome the limitations of the Langmuir model regarding the inclusion of cooperative effects and the expansion to competitive adsorption from protein mixtures various models have been developed. The currently existing models can be divided into three different approaches. Le Duc et al. developed a kinetic approach to describe the surface deposition of plasma proteins on a glass slide.<sup>50</sup> Very recently, Dell'Orco et al. devised a theory following a kinetic model to describe the corona formation on *N*-iso-propylacrylamide/*N*-tert-butylacrylamide nanoparticles.<sup>51,52</sup> Each of these models requires different adsorption and desorption rate constants which need to be determined experimentally. Furthermore, the authors need to make approximations, which not reflect the correct situation, e.g. proteins cannot diffuse on the surface. Brooks and Cramer devised a theory on competitive binding in ion-exchange systems based on mass action equilibria where the electroneutrality on the stationary phase is maintained.<sup>53</sup> Vogler et al. followed this approach with mass action equilibria to reproduce the Vroman effect. They stated that protein adsorption is mainly based on protein size discrimination and is only partially related to protein biochemistry or protein adsorption kinetics.<sup>54,55</sup> There are also models treating competitive adsorption more explicitly.<sup>56–58</sup> Fang and Szleifer used a molecular mean field theory explicitly including the size, shape and charge distributions in all molecular species adsorbed on charged planar surfaces.<sup>57</sup> Su et al. studied the adsorption of binary mixtures of bovine hemoglobin and serum albumin onto an anion exchanger.<sup>56</sup> Adsorption isotherms were fitted using a statistical thermodynamics approach based on model parameters. These parameters represent the interaction of the proteins and the surface and between two proteins. The proteins in this model are regarded as hard spheres which undergo short range interactions including lateral protein-protein interactions. Additional adjustable parameter had to be introduced to describe the interaction of a binary mixture of proteins with the anion exchanger. More recently, Vilaseca et al. modelled the competitive adsorption of HSA, Fgn and kininogen on a hydrophobic surface through coarse-grained molecular dynamics simulations.<sup>58</sup> Their results could reproduce the general trend of the Vroman effect.

To summarize, despite various experiments there is no general model describing the competitive adsorption of proteins onto nanoparticles and nanosurfaces and the results are not always independent of the underlying experiment.

## 2 Objective of this Thesis

The work of this thesis focuses on the analysis and interpretation of protein adsorption isotherms as obtained by ITC measurements. In the field of protein nanoparticle interactions ITC has emerged as a very common method to obtain the adsorption isotherm. In this thesis the adsorption isotherms of different globular proteins adsorbed onto well-defined core-shell microgels are measured with ITC. On this basis, ITC as a method to determine protein nanoparticle interactions, is discussed critically and pitfalls are described.

At the same time, the evaluation of the ITC data is discussed. Here, the analysis of the adsorption isotherm by the Langmuir model provides one of the simplest and most direct methods to quantify an adsorption process. However, as discussed in the introduction part 1.3 the thermodynamic information from the Langmuir isotherm is not quantitative. In a set of experiments the adsorption isotherms are fitted with the Langmuir Model and a cooperative binding model (CB-model) as developed by Yigit et al.<sup>59</sup> A detailed description of the cooperative binding model will follow in the next chapter. The results from both analysis are compared to each other with the aim to elucidate the limits of the Langmuir model.

Another main goal of this work was to test the predictive power of the cooperative binding model for the competitive adsorption from binary mixtures. As discussed in the introduction competitive protein adsorption and desorption processes play a pivotal role in the formation of the protein corona. In this case the Langmuir model assuming identical as well as independent binding sites is not applicable anymore.

In another part of this thesis the question of the spatial distribution of the protein in a core-shell microgel is addressed. For this purpose anomalous small angle X-Ray scattering on cytochrome c adsorbed on the microgels shell are performed. By analyzing the resonant scattering contribution the distribution of these within the shell can be derived. In addition, the amount of adsorbed protein can be quantified by this method.

In the last part the interactions of core-shell microgels immobilized on a surface are investigated. Interactions of stimuli-responsive microgels and surfaces are becoming more important for the applications of such particles as sensors or actuators. In this context it is also necessary to understand how the adsorption of protein affects the structure of the microgels on a surface. For this purpose AFM measurements of the protein loaded core-shell microgels in air and liquid were performed.

## 3 Fundamentals and Theory

### 3.1 Stimuli-Sensitive Microgels - Model Systems for Protein Material Interactions

#### 3.1.1 Introduction

In nanotechnology micron-sized and nano-sized hydrogels represent a versatile class of "smart" responsive materials. Hydrogels consist of an intramolecular cross-linked polymeric network which can absorb large amounts of solvent. Hydrogels have dimensions ranging from 10 to 1000 nm with gels in the lower range being termed nanogels and gels in the upper range being termed microgels. However, there is no clear definition and sometimes hydrogels having sizes in the micron regime are also referred as microgels. In this thesis the term microgel will be used for hydrogels with dimensions up to 600 nm. Due to their size and high surface area microgels are able to interact with cellular and subcellular domains. In addition, microgels show very distinct properties compared to their macroscopic counterparts. It is commonly accepted that microgels will react faster to chemically and/or physically changes caused by external stimuli. The characteristic time of swelling is proportional to the square of the linear dimension of the gel.<sup>60</sup>

Microgels are used for the regulated transport of (bio)molecules, switchable catalysts and for sensing applications.<sup>61,62</sup> Microgels also show interesting mechanical properties because their stiffness can be matched to natural tissues.<sup>63</sup> Adjustment of the cross-linker concentration is the most straightforward method to modulate the microgel stiffness. In general, increasing the amount of cross-linker will lead to a decreasing network flexibility and less pronounced swelling.<sup>64</sup> External stimuli like pH,<sup>65</sup> light,<sup>66</sup> temperature and ionic strength<sup>67,68</sup> can affect relative chain–chain and chain–solvent interactions, resulting in a reorganization of the polymer and solvent which finally induce a swelling or deswelling of the microgel.

Figure 3.1 depicts a core-shell microgel which responds to different stimuli by undergoing a volume phase transition in a shrunken more compact structure. Among the class of stimuli-responsive microgels thermoresponsive ones have been studied the most. The most prominent class of thermosensitive microgels is composed of N-isopropyl-acrylamide (NIPAM). At  $\approx 31\text{ }^{\circ}\text{C}$  poly-NIPAM undergoes an endothermic, entropically driven phase transition to a collapsed and deswollen state.<sup>69,70</sup> The transition occurs at a discrete temperature called lower critical solution temperature (LCST) or volume phase-transition temperature (VPTT). Below the VPTT poly-NIPAM interacts with water molecules primary through hydrogen bonding. By increasing the temperature over the VPTT chain-chain interactions are

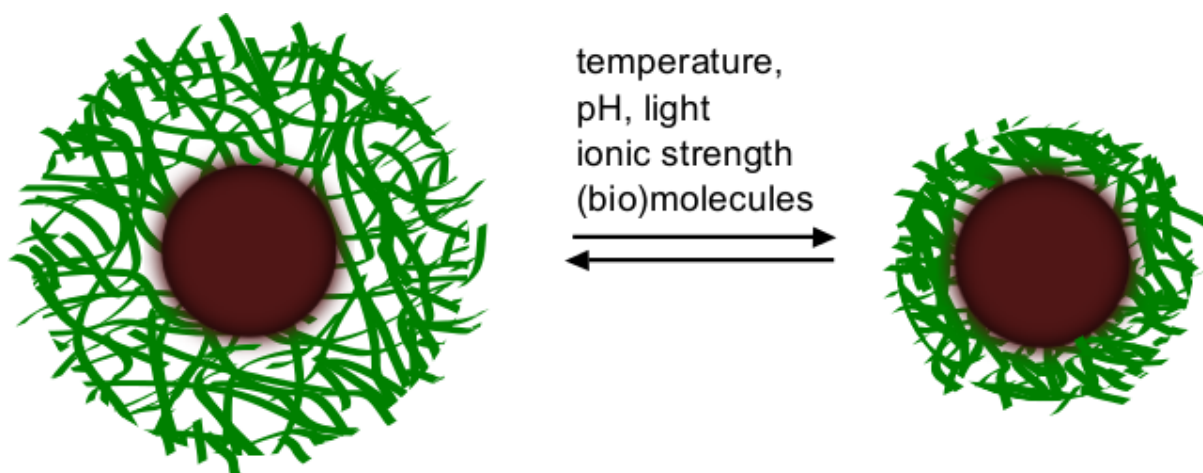


Figure 3.1: Scheme of stimuli responsive core-shell microgel with a solid core structure. The outer shell can rearrange to a more compact deswollen network under the influence of temperature and light or by adjusting solution conditions like ionic strength and pH. Furthermore, core-shell microgels can be designed to be stimuli-sensitive in the presence (bio)molecules.

favoured and water becomes a poor solvent for the microgel. Consequently, water is repelled from the inside of the microgel and the system rearranges to a more compact structure.<sup>71</sup>

### 3.1.2 Poly-NIPAM based Core-Shell Microgels

Core-Shell microgels are either composed of a hydrogel shell and a non-hydrogel core (mostly inert polystyrene or silica cores), or entirely of hydrogel compounds in both the core and shell.<sup>72</sup>

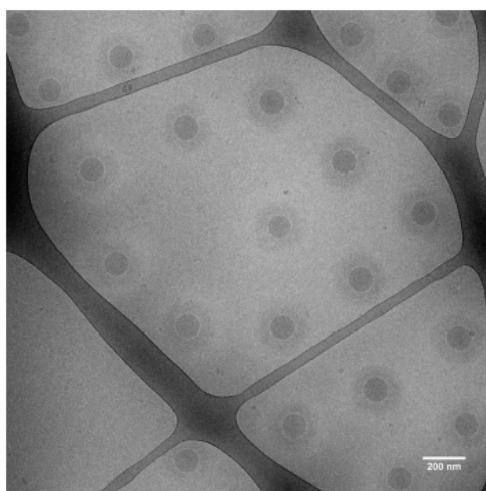


Figure 3.2: Cryo-TEM image of a 0.2 wt% aqueous suspension a negatively charged poly(NIPAM) core-shell microgel.

These colloidal particles can be analyzed by several techniques, including dynamic light scattering (DLS), cryogenic transmission electron microscopy (Cryo-TEM),<sup>73,74</sup> small angle x-ray scattering (SAXS),<sup>64,75,76</sup> small angle neutron scattering (SANS),<sup>64,77</sup> <sup>1</sup>H-NMR as well as rheology.<sup>78</sup>

Moreover, core-shell microgels present a class of model colloids with high potential for versatile applications. For instance, Lu et al. used core-shell microgels as "nanoreactors" by embedding metallic and catalytically active nanoparticles (such as Au, Rh and Pt) into the shell structure.<sup>79</sup> It was shown that the catalytic activity can be tuned by the volume transition of microgel particles.

Similar results have been also found for enzymatic activities as shown by Welsch et al.<sup>68</sup> Figure 3.2 shows a cryo-TEM image. The core-shell structure is clearly visible.

In this thesis responsive core-shell microgels have been synthesized and used as model systems to investigate the driving forces contributing to protein absorption. The microgel is composed

of a solid polystyrene core and a poly(NIPAM)-based shell. Poly(NIPAM) has a VPTT close to physiological temperature and is not cytotoxic. The synthesis of the core-shell microgel followed a two step procedure as established by Dingenouts and coworkers.<sup>75</sup> Figure 3.3 shows a scheme of the synthesis. In a first step, the PS-core was synthesised by emulsion polymerisation. In the second step the shell was attached via seeded polymerisation. The co-monomers N,N'-methylenebisacrylamide (BIS) and acrylic acid (AAc) were added in varying amounts to induce a higher cross-linking density or higher charge density, respectively. Size and morphology of the microgels are characterized by different techniques

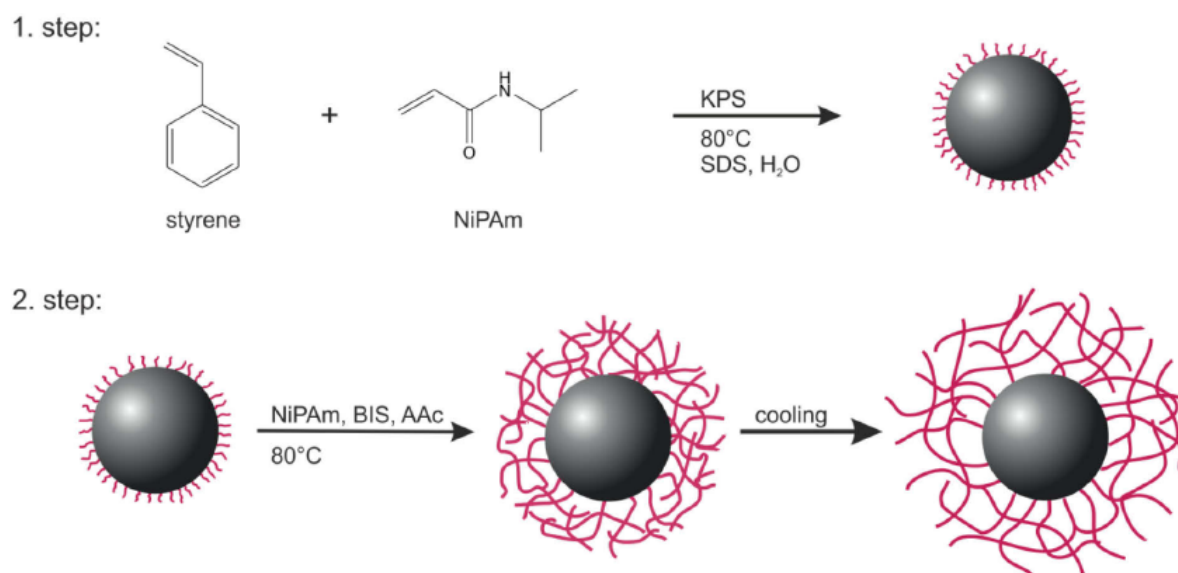


Figure 3.3: Scheme of the two-step synthesis of core-shell microgels. Reprinted from Nicole Welsch's PhD thesis.<sup>80</sup> See further explanation in the text.

like DLS, AFM, and cryo-TEM.

### 3.1.3 Interactions of Proteins with Poly-NIPAM based Core-Shell Microgels

Denaturation and concomitant loss of enzymatic activity is a problem often encountered when trying to immobilize proteins and enzymes on solid substrates. In contrast, core-shell microgels are excellent model systems to study protein adsorption, since proteins do not denature.<sup>68</sup> It has been reported that microgels even can enhance the catalytic activity of enzymes.<sup>81</sup> In addition, the colloidal dimension of the microgel shell ensures that the system responds very rapidly to environmental stimuli and protein adsorption reaches its equilibrium on the time scales of most experiments. Protein adsorption onto poly-NIPAM-based microgels was first studied by Kawaguchi et al. In their pioneering work they found out that the amount of adsorbed protein can be modulated by the VPTT and is higher for the shrunken and hydrophobic state.<sup>82</sup> Decreasing the temperature of the aqueous medium to lower than the VPTT resulted in the desorption of proteins from the network. Several other studies obtained similar results for poly-NIPAM-based microgels.<sup>83,84</sup> Lindmann et al. demonstrated that by increasing the content of hydrophobic co-monomer results in increased protein adsorption.<sup>85</sup> According to all these findings it could be inferred that the dominant driving force for protein adsorption must be hydrophobic in nature.



However, the situation changes if the network contains charged units, which will shift the VPTT to higher temperatures and will lead to electrostatic interactions between the network and the protein. For lysozyme it was shown that the binding isotherms to charged core-shell microgels substantially depend on ionic strength.<sup>59,86</sup> In particular, the uptake capacity decreases with increasing ionic strength due to charge screening effects. Smith and Lyon revealed that protein loading correlates with microgel charge. Under low ionic strength conditions the microgel with the highest amount of incorporated charges could uptake most proteins.<sup>87</sup> These findings again support the strong influence of electrostatic interactions on protein adsorption to charged microgels.

The attraction of a positively charged protein towards a negatively charged microgel is determined by the electrostatic potential difference described by a modified Donnan potential.<sup>48,59</sup> This potential originates from the phase boundary between the charged microgel and the bulk solution which leads to an unequal distribution of ions and causes the electric potential across the boundary. Under the assumption of electroneutrality the Donnan potential for monovalent ions can be expressed as follows:<sup>48,59</sup>

$$(3.1) \quad \Delta\bar{\phi} \equiv e\beta\Delta\phi = \ln \left[ y + \sqrt{y^2 + 1} \right]$$

with  $y = z_g c_g / 2c_s$  being defined as the charge ratio between gel and bulk charge densities.  $\Delta\bar{\phi}$  is the dimensionless Donnan potential scaled by  $e\beta$ . The Donnan potential leads to an osmotic pressure difference  $\pi_{ion}(y)$  between gel and bulk ions. In the ideal gas limit the osmotic pressure is given by the difference of internal and external ionic concentrations and can be expressed through:<sup>88</sup>

$$(3.2) \quad \beta\pi_{ion} = c_s \exp^{-\Delta\bar{\phi}} + c_s \exp^{\Delta\bar{\phi}} - 2c_s = 2c_s \left[ y + \sqrt{y^2 + 1} \right]$$

Figure 3.4 a shows a plot of the Donnan potential as a function distance ( $z$ ) from the surface. The potential is highest close to the phase boundary and rapidly decays towards the bulk solution and is only attractive if microgel and protein have opposite net charge. A closer look at equation 3.1 reveals that  $\Delta\bar{\phi}$

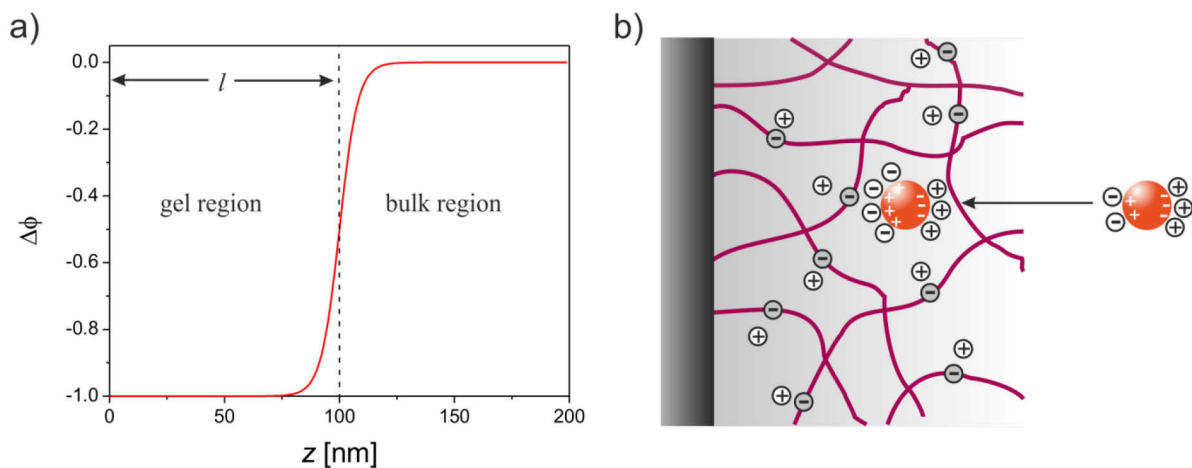


Figure 3.4: a) Local electrostatic potential difference  $\phi(z)$  of a negatively charged gel network with a gel thickness  $l$  of 100 nm as function of the distance  $z$  from the solid surface. b) Schematic representation of the charge regulation of a protein in proximity to a charged gel network. Reprinted from.<sup>80</sup>

decreases with an increase in salt concentration. By this means, the electrostatic interaction strength with the protein can be tuned. In case proteins adsorb to the microgel network the Donnan Potential defined in equation 3.1 needs to account for the change in total net charge by correcting  $y$  with the number of bound proteins  $N_i$

$$(3.3) \quad y = \left[ c_g z_g + \sum_i z_i N_i / V \right] / 2c_s$$

with  $i$  being the  $i$ -th type of protein in a mixture. It has been reported that negatively charged network can also adsorb proteins with negative net charge i.e. adsorption of a protein on the “wrong side” of the isoelectric point.<sup>68,89,90</sup> There are several driving forces which explain these like charge interactions. Counterion release, for instance, can play a major role in highly charged polyelectrolytes like spherical polyelectrolyte brushes, in which counterion condensation is favoured.<sup>91,92</sup> This is the case when Coulomb interactions dominate over the thermal interactions or more specifically for  $\Gamma = l_B / l_{charge} > 1$  with  $\Gamma$  defined as dimensionless Coulomb coupling strength with the  $l_B$  being the Bjerrum length and  $l_{charge}$  being the average distance between neighbouring charged monomers.

Adsorption of "wrong side" proteins is also facilitated by effects like charge regulation. In most cases the protein's charge distribution is set as fixed or treated as a single point net charge. This is a reasonable approach for proteins carrying a significant net charge, but when an approximately neutral protein,  $pH \approx pI$ , is approaching a charged surface, its charge distribution can be perturbed due to the local electrostatic potential on the interface.<sup>93,94</sup> For charged microgels another effect comes into play. The uneven ion distribution between the network and the bulk, as described by the Donnan potential, causes a local pH difference between the microgel network and the bulk solution.<sup>95</sup> As a consequence, proteins in proximity of the microgel network will adjust their charge according to the local pH value. In case of a negatively charged protein, the net charge can be even reversed upon adsorption if the local pH value is lower than the isoelectric point. This effect was already described for spherical polyelectrolyte brushes.<sup>92,96</sup> On the other hand, positively charged proteins can even increase their positive net charge upon binding leading to an even stronger adsorption to the microgel. Figure 3.4 b shows the mechanism of charge regulation for proteins adsorbing on a negatively charged microgel network. Counterion release and charge regulation strongly depend on ionic strength and might not be the most dominant driving forces at high salt concentrations. In addition, Bysell et al. observed the highest protein uptake in a charged microgel for the least charged peptide.<sup>97</sup> From these experiments it can be concluded that hydrophobic interactions can also be a driving force for protein adsorption.

Microgels are also useful materials to study the dynamics of protein adsorption. For the poly(NIPAM)-based core-shell microgels used in this thesis the binding kinetics have already been elucidated. Using fluorescence spectroscopy Welsch et al. were able to proof that the protein uptake in these microgels is a true equilibrium process with equilibration times in the millisecond regime and is fully reversible.<sup>98</sup> For the binding a two-step process was suggested, a fast diffusion limited step (time constant: ca. 0.6 s) and a second slower step of several hundred of seconds. It was observed that nearly 90% of the proteins are bound in the first step. Simulations were able to reproduce the kinetics of protein uptake in the milliseconds regime in agreement with the first binding step.<sup>99</sup> However, the second step could not be

observed in the simulations and is probably caused by some collective rearrangements of the proteins within the network.

### 3.1.4 Swelling behaviour of Poly-NIPAM based Core-Shell Microgels

The volume of a microgel  $V_g$  strongly depends on swelling and deswelling effects. In general, swelling of a polymer network is determined by the balance of osmotic and elastic pressure  $\pi_{elastic}$  and  $\pi_{osm}$ , respectively.<sup>88,100</sup>

$$(3.4) \quad \pi = \pi_{osm} + \pi_{elastic} = 0$$

The elastic pressure term can be represented by the shear modulus  $G$  using the theory of rubber elasticity. For weakly charged polymeric networks the powerlaw  $\pi_{el} \propto V^{-m}$  with  $m = 1/3$  is found.<sup>100–104</sup> The osmotic term has two different contributions. The first one emerges from the mixing entropy of polymer chains with solvent molecules that can be expressed by Flory-Rehner theory<sup>105,106</sup> or by using following powerlaw:<sup>101,107</sup>  $\pi_{mix} \propto V^{-n}$ . Below the VPTT water is a good solvent for NIPAM based gels and  $n = 9/4$ , but for gels above the VPTT and highly charged ones corrections may arise. The latter term is the osmotic ideal gas pressure  $\pi_{ion}$  resulting from the inhomogeneous ion distribution between bulk and gel and is expressed via equation 3.2

The expression for the total pressure then is:<sup>59</sup>

$$(3.5) \quad \pi = AV^{-n} + BV^{-m} + \pi_{ion}(y)$$

with A and B being volume independent constants. In the limit of high bulk salt concentration  $c_s$  the ionic contribution can be neglected and  $\pi_{ion}(y) = 0$ . The balance between osmotic and elastic pressure also determines the mechanical properties of the microgel in terms of the modulus  $K_{comp}$  defined as inverse compressibility  $K_{comp} = -V(\partial\beta\pi/\partial V)$ . By fitting equation 3.5 to various salt concentrations the values for A, B and  $K_{comp}$  are obtained. Generally, equation 3.5 is valid in the ideal gas limit, monovalent salts, and does not consider important contributions from adsorbed proteins. In principle, addition of proteins will lower the total net charge and inhomogenize the charge distribution in the network.<sup>59</sup> However, there is no general theory covering these effects.

### 3.1.5 Interactions of Microgels with Surfaces

Most published literature on stimuli-responsive microgels investigated the properties of microgels in bulk solution. However, for applications of such particles as sensors or for actuators it is necessary to attach the particles on a surface. For this reason, interactions of stimuli-responsive microgels and surfaces are becoming more important. Lu and Drechsler, for example, investigated the selforganization processes of monosized poly(NIPAM)-based microgels on a gold surface. It was found that the electrostatic interactions between the microgel particle and charged substrate surface dictate the pattern formation.<sup>108</sup> In particular, particles deposited under water evaporation onto a surface with opposite surface charges will form an ordered 2-D array, while particles deposited onto a surface with same charge will destroy

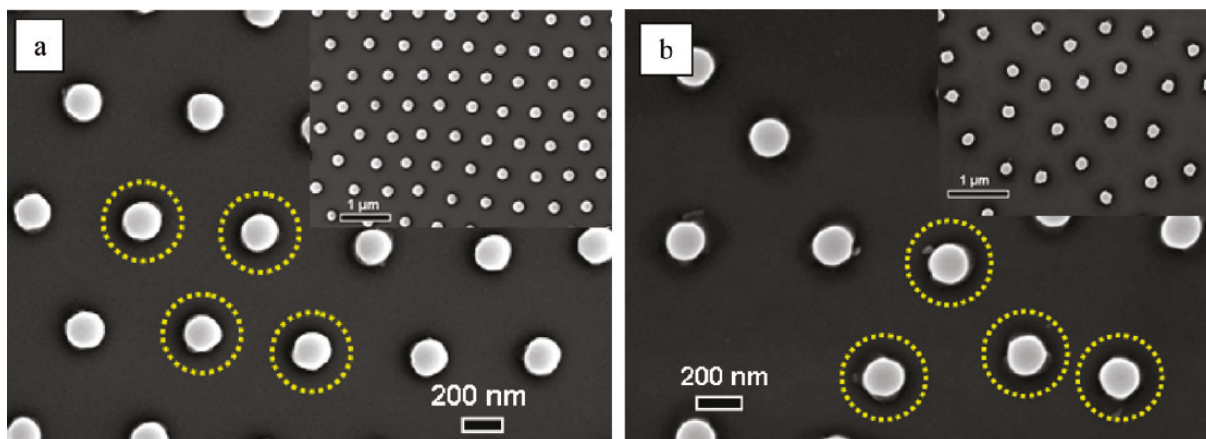


Figure 3.5: Field-emission scanning electron microscope images of positive microgel particles (a) and negative microgel particles (b) assembled on mica substrates. The dashed circles indicate the size of microgel particles in the wet state. Reprinted from Lu et al.<sup>108</sup>

the ordered structure due to strong electrostatic repulsion (see Figure 3.5) Adsorption to a surface also influences the volume phase transition of poly(NIPAM)-based microgels. AFM experiments could prove that adsorbed poly(NIPAM)-co-vinylacetic acid microgels are still thermo-sensitive with the same transition temperature, but the swelling capacity decreases by up to one order of magnitude compared to the swelling ratio in bulk solution.<sup>109</sup> In the collapsed state the microgel flattens considerably due to additional adhesive bonds to the surface. Thus, the adsorbed microgels capture the heterogeneity of chain deformations that occur when surfaces with sub-micrometer roughness interact. Duner et al. studied the mechanical properties of microgel particles attached to a silicon surface. They found a non-monotonic behaviour of the elastic modulus measured by AFM, exhibiting a softening through the transition and then a stiffening above the transition.<sup>110</sup>

In this context it is interesting to find out how protein loading affects the modulus of the microgel particles, because the microgel changes from a highly-swollen network, to a condensed, protein-rich material. Up until now, there are just a few published experiments which investigated the interactions and mechanical properties of stimuli-responsive microgels being attached to a surface and loaded with protein. Huo et al., for example, were able to show that microgel particles attached to a glass substrate underwent bridging aggregation when being loaded with BSA.<sup>89</sup>

## 3.2 Characterization of Single Protein Adsorptions to Core-Shell Microgels

### 3.2.1 Isothermal Titration Calorimetry (ITC)

Isothermal titration calorimetry (ITC) is a fast, precise and widely used technique for measuring binding thermodynamics of a chemical or biochemical ligand binding in solution. ITC is applicable to any reaction involving a heat change and due to its simplicity in operation it is used in different fields like biochemistry, drug design or material sciences. The technique is also sensitive to conformational re-

arrangements in macromolecules like DNA or proteins and can detect changes in protonation in these macromolecules. Moreover, it emerged as a reliable method determining the thermodynamics of protein nanoparticle interactions.

Figure 3.6 a shows the general setup of an ITC instrument. The instrument consists of a sample cell and a reference cell. The former one is usually filled with the nanoparticle suspension and the latter one is filled with ultrapure water. Before each titration the two cells need to be equilibrated in such a way that the temperature difference  $\Delta T$  between the cells approaches zero and the applied reference power  $dP$  of the feedback system shows a stable baseline. After this equilibration period a defined amount of protein

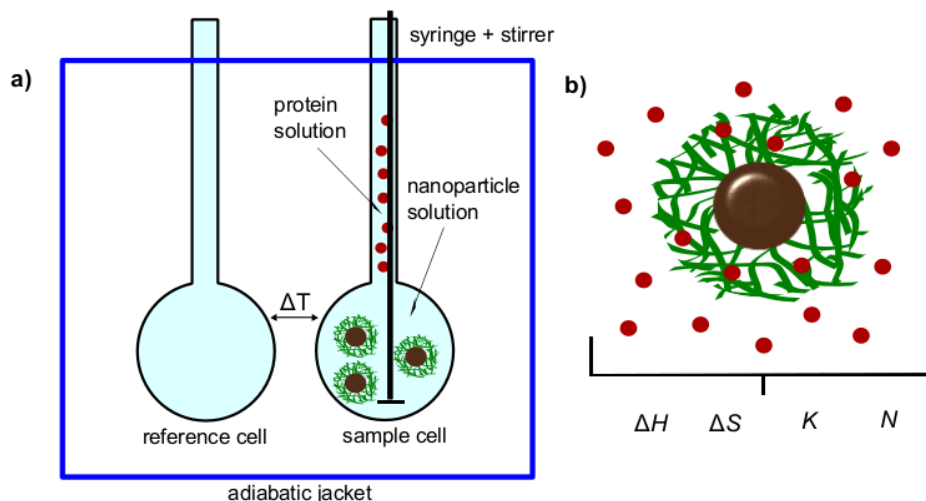


Figure 3.6: a) Schematic representation of an isothermal titration calorimeter. The instrument is made of a reference cell and a sample cell which are surrounded by an adiabatic jacket. Both cells consist of an efficient thermally conducting and chemically inert material. The sample cell is filled with the nanoparticle solution. Under constant stirring defined amounts of the ligand (in this case the protein solution) are injected with an automated syringe. Injection of the ligand will cause some heat difference between the sample cell and the reference cell. Depending on the nature of the reaction (i.e., exothermic or endothermic) in the sample cell the feedback power will either increase or decrease to maintain an equal temperature between the two cells. The output signal has the form of an incremental heat change per injection  $dQ/dx = Q'(x)$ . b) Scheme of a nanoparticle adsorbing proteins. Fitting of the ITC data with the Langmuir model reveals the thermodynamic parameters  $\Delta H$ ,  $\Delta S$ ,  $K$  and  $N$ .

solution is titrated into the sample cell and sensitive thermocouple circuits are used to detect temperature differences  $\Delta T$  between the cells. Depending on the type of reaction i.e exothermic or endothermic the feedback system will either decrease or increase the applied power  $dP$  in order to maintain the baseline. The output signal has the form of a differential heat change per injection  $dQ/dx = Q'(x)$ . The quantity  $x$  is defined as molar ratio  $x = c_p^{tot}$ . Fitting of  $Q'(x)$  with an appropriate binding model e.g. Langmuir model reveals the thermodynamic parameters  $\Delta H$ ,  $\Delta S$ ,  $K$  and  $N$  for the binding of the protein onto the NP (Figure 3.6 b).

Table 3.1 summarizes recent experiments using ITC to investigate protein adsorption onto nanoparticles. Dawson et al., for example, investigated the adsorption of  $\beta 2$ -microglobulin, a protein playing a key role in amyloid diseases, onto *N*-isopropylacrylamide (NIPAM) and *N*-tert-butylacrylamide (BAM).

They showed that  $\beta$ 2-microglobulin forms multiple layers around the NP with the first layer forming in an endothermic process.<sup>111</sup> Further ITC studies within this group included the adsorption behavior of human serum albumin HSA to NIPAM/BAM nanoparticles of varying hydrophobicity and curvature.<sup>85</sup> It was shown that the protein preferentially adsorbs to nanoparticles with low curvature and high hydrophobicity. Henzler et al. studied the uptake of  $\beta$ -Lactoglobulin (BLG) onto spherical electrolyte brushes (SPBs) at different salt concentrations by ITC. The analysis confirmed that the adsorption is mainly entropy driven with the release of counterions from the SPB being the primary driving force.<sup>112</sup>

In an experiment from Welsch et al. ITC was even sensitive enough to proof a protonation of a protein while being adsorbed to a microgel.<sup>68</sup> Mohr et al. used ITC to investigate the adsorption of different plasma proteins on to hydroxyethyl starch nanocapsules.<sup>35</sup>

Table 3.1: Overview about ITC measurements used to obtain protein adsorption isotherms onto various types of nanoparticles (NPs).

	BSA <sup>a)</sup>	HSA <sup>b)</sup>	BLG <sup>c)</sup>	Pap <sup>d)</sup>	Lys <sup>e)</sup>	cytc <sup>f)</sup>	GOX <sup>g)</sup>	Apo-A1 <sup>h)</sup>	plasma	RNase
Si	113				113				113	
Au	23									
ZnO	114									
PS <sup>i)</sup>	115,116									
Chitosan NPs	117									
Magnetic NPs	118				118					
SPB <sup>j)</sup>	119,120		112,120	120						91
Nanocapsules		35						35	35,121	
Microgels	85			122	68,122	98,122	98			122

a) bovine serum albumin b) human serum albumin c)  $\beta$ -lactoglobulin d) papain e) lysozyme f) cytochrome c g) glucoseoxidase h) apolipoprotein A1 i) polystyrene j) spherical polyelectrolyte brush

### 3.2.2 Evaluation of ITC data

The main parameters that can be extracted from a typical ITC experiment are the binding enthalpy  $\Delta H$  and the binding constant  $K$ . From these it is then a simple procedure to calculate the Gibbs free energy  $\Delta G$  and entropy  $\Delta S$  via the common thermodynamic equations:<sup>123</sup>

$$(3.6) \quad \Delta G = -RT \ln K$$

$$(3.7) \quad \Delta G = \Delta H - T\Delta S$$

Injection of the protein solution into the cell containing the microgel is accompanied by a release of heat  $Q$  originating from the binding event and the heat of dilution. Figure 3.7 shows a typical dataset obtained from an ITC experiment. The upper panel depicts to the raw data recorded as incremental heat  $dQ/dt$  and the lower panel shows the adsorption isotherm and the corresponding Langmuir fit. It is assumed that the total heat per injection will be linear to the number of bound protein  $N_b$ :

$$(3.8) \quad Q(N_b) = \Delta H c_m V_{tot} N_b$$

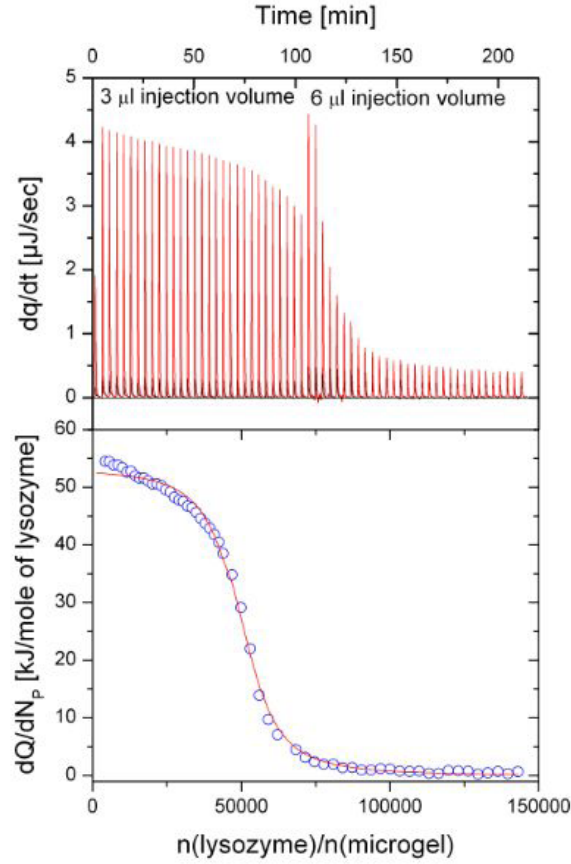


Figure 3.7: ITC titration of lysozyme binding to microgel NW15 in 10 mM MOPS buffer at pH = 7.2 and 298 K. The upper panel shows the ITC raw data for each injection with the differential heat  $dQ/dt$  emerging as the red peaks. The blue circles in the lower panel show the integrated peaks/signal, which correspond to the differential heat per mol of injectant  $dQ/dx$ . The red line is the Langmuir fit. Values have been corrected for the heat of dilution by subtraction from the overall heat.

After correcting the raw signal for the heat of dilution it is more convenient to extract  $\Delta H$ ,  $N$  and  $K$  by fitting the incremental heat  $Q'(x) = \partial Q / \partial x$  to a binding model:

$$(3.9) \quad Q'(x) / (V_{tot} c_p^{tot}) = \Delta H N_b(x) / x$$

The manufacturer microcal offers an analysis tool which is based on the Langmuir framework called model of single independent binding sites (SSNI model) and is compatible with the Origin®7.0 software. As already discussed in section 1.3 the Langmuir equation is often applied, if the assumption of  $N$  independent and identical binding sites is valid to a considerable degree. The binding constant in the Langmuir model is defined as (see section 1.3):

$$(3.10) \quad K = \frac{\Theta}{(1 - \Theta)c_p}$$

The concentration of the unbound protein outside the gel  $c_p$  is not known, but can be expressed by the total protein concentration  $c_p^{tot}$  and the binding fraction  $\theta$  through

$$(3.11) \quad c_p = c_p^{tot} - N\Theta c_p$$

With this definition  $c_p$  in equation 3.10 can be substituted leading to a quadratic equation for  $\Theta$  which can be solved leading to

$$(3.12) \quad \Theta = \frac{1}{2} \left[ 1 + \frac{x}{N} + \frac{1}{NKc_m} - \sqrt{\left( 1 - \frac{x}{N} + \frac{1}{NKc_m} \right)^2 - \frac{4x}{N}} \right]$$

If we assume  $\Delta H$ ,  $N$  and  $K$  being independent of the protein concentrations equation 3.8 and 3.12 can be combined to give the total heat  $Q(x)$

$$(3.13) \quad Q(x) = \frac{1}{2} N_b \Delta H c_m V_{tot} \left[ \xi - \sqrt{\xi^2 - 4x/N} \right]$$

with  $\xi = 1 + \frac{x}{N} + \frac{1}{NKc_m}$ . Fitting of the differential heat  $Q'(x)/(V_{tot}c_p^{tot})$  with respect to the molar ratio finally reveals the values for  $N$ ,  $\Delta H$  and  $K$ . Typically, a curve of  $Q'(x)$  resembles a sigmoidal form. In general, for small  $x$  a plateau is observed and the intersection with the y axis determines  $\Delta H$ .  $N$  is defined as the inflection point where the molar ratio equals the number of binding sites and  $K$  is the sharpness of the transition at the inflection point for  $x = N$ . In particular, for the first injections  $Q'(x)$  is constant and proteins enter the network immediately and continuously. With  $N(x) \simeq x$  here the fitting is not very sensitive to the binding constant. For high values of  $x$  the number of binding sites saturates and  $Q'(x) = 0$ . Hence, the fitting procedure is most sensitive at the inflection point.

### 3.2.3 Problems of ITC

ITC is a sensitive method to obtain the adsorption isotherm of proteins adsorbing to a nanoparticle.

However, the shape and the quality of the ITC isotherms can be strongly influenced by different conditions and in order to avoid pitfalls there are certain prerequisites which need to be considered. First of all the protein needs to be available in high concentrations so that the heat of the adsorption process is sufficient enough to produce a detectable signal higher than the background noise. Experience shows that in most experiments protein concentrations in the mg range were used.<sup>35,81,91</sup>

It is also necessary to check, if the protein and the nanoparticle under investigation have stable structures under experimental conditions where pH, temperature or salt strength are varied. In particular, high molecular weight proteins can exist as monomers, dimers or higher oligomers and their structure can vary depending on the external conditions. As a consequence, a mixture of different protein structures can be present and the underlying adsorption isotherm reflects the average adsorption of the different protein structures. Furthermore, it need to checked, whether the proteins and the nanoparticles do not form aggregates.

Another pitfall is the heat of dilution which needs to be measured carefully and subtracted from the measurement of protein and nanoparticle. The heat of dilution is defined as the change in enthalpy when an infinitesimal amount of solvent or solute is added to a solution at constant pressure. For an ideal solution the heat of dilution is zero, but in a non ideal case the heat of dilution depends on activity coefficient of the  $i$ -th solute,  $\gamma_i$ , and can be written as:<sup>124</sup>

$$(3.14) \quad \Delta H_{dil} = \sum_i v_i RT \ln \gamma_i \left( 1 + \frac{T}{\epsilon} \frac{\partial \epsilon}{\partial T} \right)$$



Here,  $\nu_i$  is the stoichiometric coefficient and  $\epsilon$  is the relative permittivity. In an ideal case the heat of dilution is constant, i.e. the amount of heat generated or consumed after each injection of the solute is the same. However, the activity coefficients for already dissolved ions can change since the ionic strength increases with the addition of proteins. Moreover, water-mediated effects between the protein and salt molecules come into play and reorganize solvent structures. Both effects can lead to a heat of dilution which is not constant, but varies with the amount of injected protein. After subtraction of the heat of dilution the adsorption isotherm in the saturation regime should approach zero as depicted in Figure 3.8 a (green curve), i.e. the ITC signal in this regime is equal to the heat of dilution. The experiment should be repeated carefully, if this is not the case. Especially, the fitting will be difficult and care needs to be taken in the interpretation of the thermodynamic parameters.

To obtain a good shaped adsorption isotherm by ITC the concentration of the protein and the nanoparticle should be in a certain range. The optimal concentration of the microgel  $c_m$  to be titrated depends on the binding constant  $K$  and the number of binding sites  $N$  and is calculated from the dimensionless parameter  $C$  also referred as C-value or Weitzmann parameter<sup>125,126</sup> defined as

$$(3.15) \quad C = K \cdot c_m \cdot N$$

In Figure 3.8 b simulated isotherms for a 1:1 binding stoichiometry for different binding constants determining the  $C$ -value are depicted. Two conclusions can be drawn from this simulation: First, very large  $C$ -values lead to very tight binding and the binding enthalpy  $\Delta H_{ITC}$  is determined accurately, but for  $C$ -values  $> 500$  the isotherm shape is invariant with  $K$ . Secondly, when  $C < 10$ , the titration isotherm

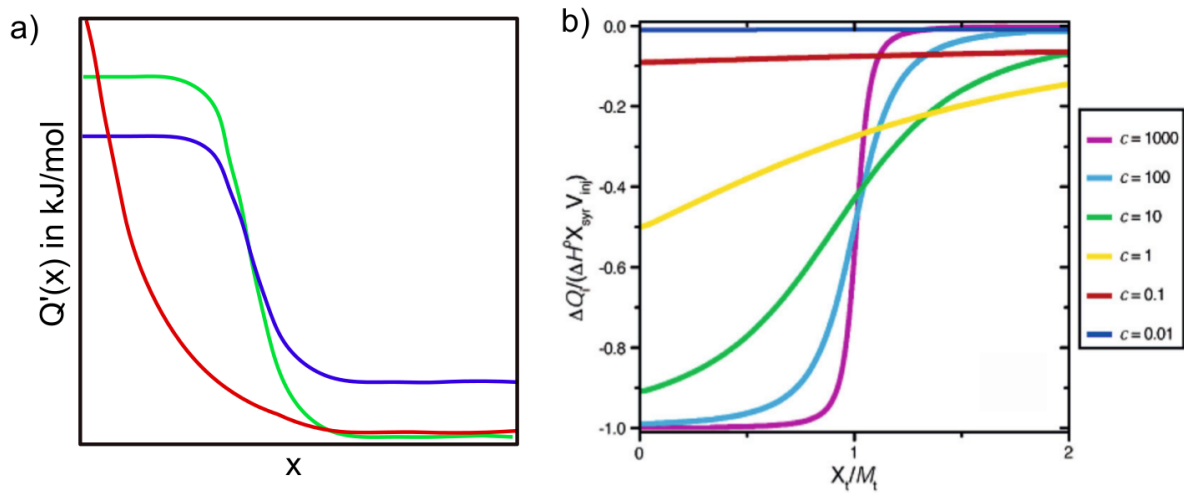


Figure 3.8: The shape of ITC curves: Problems and Pitfalls: a) Normalized ITC titration curves for i) a sigmoidal curve with pronounced plateau (green line), ii) sigmoidal curve with pronounced plateau, but with no saturation regime (blue line) and iii) curve without plateau (red line) b) Simulated ITC titration curves for varying values of  $C$  and for  $N=1$ . Graph reprinted from reference<sup>126</sup>

becomes less confident in the fitting of  $K$  and especially in the fitting of  $\Delta H_{ITC}$ . Thus, the most ideal range for measuring a reliable adsorption isotherm is for  $20 < C < 500$ .

However, in case of the adsorption of proteins to (polymer-coated) nanoparticles  $C$ -values in the right

range do not guarantee a sigmoidal isotherm and isotherms with rather exponential shapes (see Figure 3.8 a (green and red curve, respectively) have been measured.<sup>35,116,127</sup> As a consequence, fitting of  $\Delta H_{ITC}$  becomes difficult since there is no plateau in the isotherm and values of  $\Delta H_{ITC}$  can become unrealistically high. In general, for the plateau region of the isotherm the incremental heat per injection  $Q'(x)$  is constant. In other words, the injected proteins are immediately adsorbed from the nanoparticle with a constant heat  $Q = \text{constant}$ . Thus, the missing plateau can originate from strong cooperative effects which change  $Q'(x)$ .

In summary, ITC is a reliable method to study the interactions of proteins and nanoparticles if certain prerequisites are fulfilled. These include: i) a sufficiently high protein concentration to obtain a good ITC signal ii) a concentration of the nanoparticle lying in a reliable range of the  $C$ -value and iii) a careful subtraction of the heat of dilution.

### 3.2.4 Small Angle Scattering (SAS)

Small-angle scattering experiments are either carried out with X-rays (SAXS) or neutrons (SANS) and are a powerful and widely used method to gain insight in nanostructure and structural dynamics of biological macromolecules, polymers and nanocomposite materials. SAS has become also the method of choice to investigate the spatial distribution of proteins on functionalized and non-functionalized nanoparticles. At the same time the total amount of bound protein to the NP can be determined and compared to results from ITC or ultrafiltration.

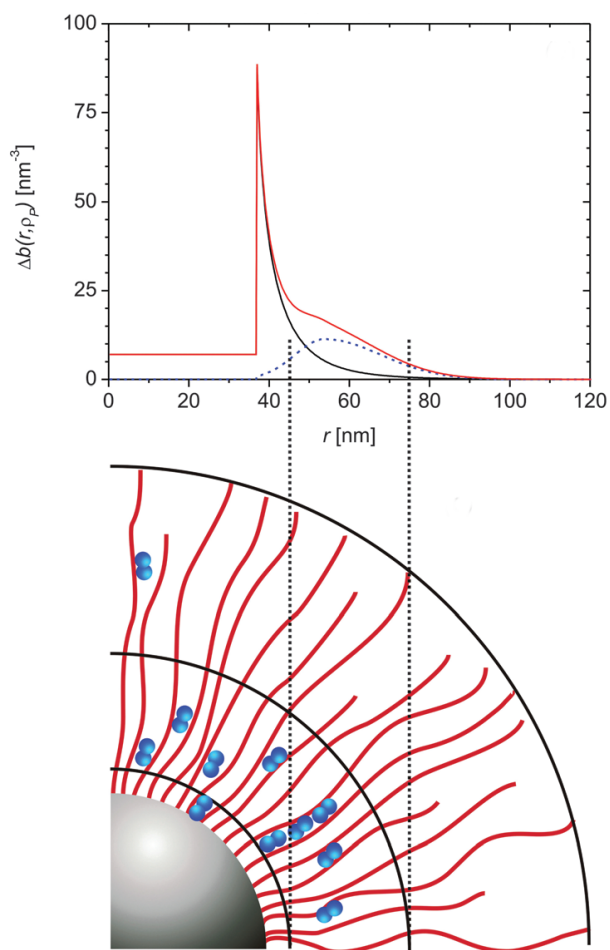


Figure 3.9: 2-dimensional representation of the SPB with the distribution  $\beta$ -lactoglobulin (lower panel) derived from the electron density profiles of the pure brush evaluated from the SAXS data (upper panel). Reprinted from Henzler et al.<sup>128</sup>

In the 1990s Mackie et al. studied the adsorption of  $\beta$ -casein on a polystyrene lattices with SAXS. They found that the protein forms a monolayer on the particle surface and adopts a more compact structure than in solution.<sup>129</sup> Vauthier et al. investigated the adsorption of bovine serum albumin (BSA) on block copolymers composed of a hydrophobic core and a hydrophilic dextran shell by SANS. The number density and configuration of the adsorbed BSA molecules was determined from the SANS scattering curves. It was demonstrated, that BSA adsorbs onto the NP in a flat configuration.<sup>130</sup> The uptake of  $\beta$ -lactoglobulin, BSA, and RNase to poly(styrene sulfonic acid, PSS) and poly(acrylic acid, PAA) grafted spherical polyelectrolyte brushes (SPB) has been studied by Henzler et al. and Rosenfeldt et al.<sup>119,128,131,132</sup> In the case of  $\beta$ -lactoglobulin and the PSS grafted SPB the proteins are adsorbed in layerlike structures. While the proteins in the layers close to the core are tightly bound, those ones located in the outer layers are only weakly bound and can be washed out.<sup>128</sup> Figure 3.9 shows a sketch of the proteins distributed onto the SPB. From the electron density profiles it can be concluded that most of the proteins adsorb to

the inner layers close to the core.

SAXS is also a method to monitor the uptake of proteins in a time-resolved manner. The adsorption of BSA, for example, was monitored by time-resolved SAXS<sup>132</sup> with high temporal and spatial resolution with the result that the protein uptake scales with time with  $t^{1/4}$ . More recently, Bharti et al. investi-

gated  $\beta$ -lactoglobulin and lysozyme onto negatively charged silica particles as a function of pH.<sup>133</sup> The study provided strong evidence that lysozyme can promote bridging of the silica particles which cause aggregation.

### 3.2.4.1 Theory of SAS

In the following section the basic concepts of SAS are illustrated briefly. The interpretation of scattering data is based on the general relation between the measured scattering intensity as a function of momentum transfer  $q = 4\pi \sin\Theta/\lambda$  with  $\lambda$  being the wavelength of the X-ray radiation and  $2\theta$  the scattering angle.

$$(3.16) \quad I(q) = N(\Delta\rho)^2 F(q)S(q)$$

Here,  $N$  are the number of particles in the scattering volume,  $\Delta\rho = \rho_p - \rho_s$  is the contrast between the particle (p) and the solvent (s),  $F(q)$  is the form factor, and  $S(q)$  is defined as the structure factor. For small angle X-Ray scattering the contrast originates from the electron scattering length densities while for small angle neutron scattering the contrast depends on the nuclei's characteristics; i.e. the scattering length density of the nuclei. Thus, both techniques can be treated within the same theoretical framework. The scattering intensity can be expressed via the amplitude square averaged over the solid angles  $\Omega$

$$(3.17) \quad I(\vec{q}) = \langle I(\vec{q}) \rangle_{\Omega} = \langle A(\vec{q})A^*(\vec{q}) \rangle_{\Omega}$$

Here the scattering amplitude  $A(\vec{q})$  is defined as

$$(3.18) \quad A(\vec{q}) = \int_0^{\infty} \rho(\vec{r}) \cdot \exp[-i\vec{q}\vec{r}] d^3r$$

and averaging over all orientations in a two-phase system leads to

$$(3.19) \quad A(q) = 4\pi \int_0^{\infty} \Delta\rho \frac{\sin qr}{qr} r^2 dr$$

An easy and straight forward way of analysis of the scattering which is often applied in small angle scattering is the Guinier analysis. The general Guinier relation states that

$$(3.20) \quad I(q) = I(0) \cdot \exp\left(-\frac{1}{3}R_g^2 q^2\right)$$

where the radius of gyration and the forward scattering intensity are defined as  $R_g$  and  $I(0)$ , respectively. The latter one is related to the molecular mass of the macromolecule. The values  $R_g$  and  $I(0)$  are usually obtained by plotting  $\ln[I(q)]$  vs.  $q^2$ , whereby the slope of the Guinier plot corresponds to  $-R_g^2/3$  and the intersection with the ordinate to  $I(0)$ . The Guinier analysis is only valid for small angles, i.e.  $qR_G \ll 1$  and requires monodisperse particles. If the particles in the sample have different sizes the sizes of the smaller particles will be difficult to determine since the scattering will be dominated by the larger particles.

A method to analyze the adsorption of proteins onto core-shell nanoparticles like brushes and microgels was devised from Breininger and Rosenfeldt et al.<sup>131</sup> In their analysis the scattering intensity for core-shell systems can be split into three terms<sup>131</sup>

$$(3.21) \quad I(q) = I_{CS}(q) + I_{fluc}(q) + I_{PS}$$

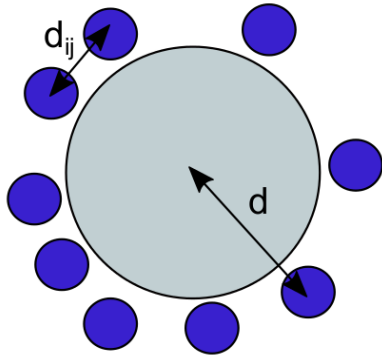
The first term  $I_{CS}(q)$  originates from the overall structure of the core-shell microgel. Usually the polystyrene core has a small SAXS contrast while the shell has a higher contrast. The term  $I_{fluc}(q)$  accounts for the fluctuations of the polyelectrolyte layer on the surface and can be expressed via<sup>131</sup>

$$(3.22) \quad I_{fluc}(q) = \frac{I_{fluc}(0)}{1 + \xi^2 q^2}$$

where  $\xi$  denotes the spatial extent of the fluctuations. The fluctuation term contributes mainly at high scattering vectors and is rather negligible if the low  $q$ -part is chosen for the analysis.<sup>128,131</sup>  $I_{fluc}(0)$  determines the contribution at the vanishing scattering vector. The term  $I_{PS}$  accounts for differences of the electron density in the solid polystyrene core. Its contribution to the overall scattering intensity is negligibly small.

At this point it is necessary to discuss how the adsorption of protein will change the overall scattering intensity as defined in equation 3.21. At high  $q$  there is no visible fine structure of the shell and adsorbed proteins will simply increase the electron density. However, at low and intermediate  $q$  a different theoretical approach is necessary.

Breininger et al. could demonstrate that the scattering function of such a composite system can be treated as one big sphere and several small spheres - i.e. the proteins - attached to the surface of the big sphere<sup>131</sup> as depicted schematically in Figure 3.10. The scattering intensity can then be rewritten as:



$$(3.23)$$

$$I(q) = A_{large}^2(q) + \sum_i A_{small,i}^2(q) + \sum_i A_{small,i}(q) A_{large}(q) \frac{\sin qd}{qd} + 2 \sum_{i \neq j} A_{small,i}(q) A_{small,j}(q) \frac{\sin qd_{ij}}{qd_{ij}}$$

Figure 3.10: Scheme of the model used for the calculation of the scattering function of the composite system consisting of a spherical nanoparticle and adsorbed protein. See further explanations in the text

where  $d$  is defined as the distance between the centers of gravity between the large and the small sphere and  $d_{ij}$  are the distances between the small spheres (see Figure 3.10). The first term in equation 3.23 originates from the scattering of the big sphere and will fall off as  $q^{-4}$ . The second term can be seen as the intensity of a suspension of noninteracting small spheres. The remaining sum terms are both function of  $qd$  and will mainly contribute at high  $q$ -values. The third term oscillates with  $\sin qd/qd$  and a small polydispersity will cancel its

contribution for sufficiently high  $q$ . The second sum in equation 3.23 will vanish as well if the small spheres (proteins) are assumed to be distributed randomly around the big sphere with the distance  $d_{ij}$ . Consequently, for intermediate and low  $q$ -values the intensities of the big spheres (core-shell) and small spheres (proteins) simply add up.

### 3.2.4.2 ASAXS

Anomalous small-angle X-ray scattering (ASAXS) serves as an additional method of contrast variation. The method utilizes the dependence of the atomic scattering factor  $f$  if the energy of the incident radiation is near the absorption edge of an atom or ion.

$$(3.24) \quad f_z(E) = f_{0,z} + f'_z(E) + if''_z(E)$$

The first term  $f_0$  corresponds to the nonresonant term. The second and third terms in are the real and imaginary part of the so-called anomalous dispersion corrections of the atomic scattering factors which show dramatic changes in the vicinity of the absorption edges. The scattering amplitude for an ASAXS experiment writes

$$(3.25) \quad A(\vec{q}) = \int_{V_p} \Delta\rho(\vec{r}) \cdot \exp[-i\vec{q}\vec{r}]d^3r + \int_{V_p} \Delta\rho_{ion}(\vec{r}) \cdot \exp[-i\vec{q}\vec{r}]d^3r$$

Here  $\Delta\rho$  and  $\Delta\rho_{ion}$  are the excess electron densities of the macromolecule and the ions and  $V_p$  is the particle volume. Calculating the scattering intensity  $I(\vec{q}) = |A(\vec{q})|^2 = A(\vec{q}) \cdot A^*(\vec{q})$  and averaging over all orientations of the macromolecule yields a sum of three contributions with the three partial intensities:<sup>134</sup>

$$(3.26) \quad \begin{aligned} |A(q)|^2 &= \Delta f_0^2 \int_{V_p} \int u(\vec{r})u(\vec{r}') \frac{\sin(q|\vec{r}-\vec{r}'|)}{q|\vec{r}-\vec{r}'|} \\ |A_{mix}(q, E)|^2 &= 2\Delta f_0 \cdot (f_{0,ion} - \rho_m V_{ion} + f'(E)) \int_{V_p} \int u(\vec{r})v(\vec{r}') \frac{\sin(q|\vec{r}-\vec{r}'|)}{q|\vec{r}-\vec{r}'|} \\ |A_{ion}(q, E)|^2 &= |\Delta f_{ion}(E)|^2 \int_{V_p} \int v(\vec{r})v(\vec{r}') \frac{\sin(q|\vec{r}-\vec{r}'|)}{q|\vec{r}-\vec{r}'|} \end{aligned}$$

Here  $|A(q)|^2$  is the non-resonant scattering originating from the macromolecule, the crossterm  $|A_{mix}(q, E)|^2$  or mixed-resonant scattering originating from the superposition of the scattering amplitudes of the macromolecule and ions, and  $|A_{ion}(q, E)|^2$  the pure-resonant scattering term which just includes contributions from the ions. The quantities  $u(\vec{r})$  and  $v(\vec{r})$  are the particle densities of the macromolecule and the ions, respectively, and  $\rho_m$  is the electron density of the solvent;  $V_{ion}$  is the volume of the ion;  $\Delta f_0$  and  $\Delta f_{0,ion}$  are the contrast of the polymer and ion with respect to the solvent. By measuring the scattering curves at at least three energies ( $E_1$ ,  $E_2$  and  $E_3$ ) in the vicinity of the absorption edge of the present ion it is

possible to extract the pure-resonant scattering term  $|A_{ion}(q, E)|^2$ .<sup>134</sup>

$$(3.27) \quad |A_{ion}(q)|^2 = \int_{V_p} \int v(\vec{r})v(\vec{r}') \frac{\sin(q|\vec{r} - \vec{r}'|)}{q|\vec{r} - \vec{r}'|} =$$

$$\left[ \frac{I(q, E_1) - I(q, E_2)}{f'_{ion}(E_1) - f'_{ion}(E_2)} - \frac{I(q, E_1) - I(q, E_3)}{f'_{Fe}(E_1) - f'_{Fe}(E_3)} \right] \cdot \frac{1}{F(E_1, E_2, E_3)}$$

with

$$F(E_1, E_2, E_3) = f'_{ion}(E_2) - f'_{ion}(E_3) + \frac{f''_{ion}(E_1) - f''_{ion}(E_2)}{f'_{ion}(E_1) - f'_{ion}(E_2)} - \frac{f''_{ion}(E_1) - f''_{ion}(E_3)}{f'_{ion}(E_1) - f'_{ion}(E_3)}$$

Equation 3.27 is an analytical solution to extract the pure-resonant scattering contribution from an ASAXS experiment measured at three energies. Structural information of the ions like their distribution can be obtained from the analysis of the form factor. Hence, the separation of the resonant scatterer makes ASAXS an effective tool for the analysis of polyelectrolytes. In particular, ASAXS has been applied in numerous publications to study the distribution of counterions around a polyelectrolyte.<sup>134–136</sup> Additionally, it was shown that ASAXS can quantify the amount of resonant scatterers i.e the ions in the scattering volume by utilizing the following integral

$$(3.28) \quad Q_{ion} = |\Delta f_{ion}(E)|^2 \int_Q |A_{ion}(q)|^2 d^3q$$

Here  $Q_{ion}$  is the resonant invariant and is related to the number density of the ions  $\bar{v}_{ion}$  defined as:<sup>137</sup>

$$(3.29) \quad \bar{v}_{ion} = \frac{1}{2V_{ion}} \pm \sqrt{\frac{1}{4V_{ion}^2} - \frac{1}{(2\pi)^3 r_0^2} \int_Q |A_{ion}(q)|^2 d^3q}$$

where  $V_{ion} = \frac{4\pi}{3} R_{ion}^3$  is the volume of the ion and  $r_0$  is the classical electron radius.

### 3.3 Characterization of Competitive Protein Adsorptions to Microgels

#### 3.3.1 Fluorescence Spectroscopy

Fluorescence based methods are commonly applied to determine protein nanoparticle interactions. Boulos et al. used static fluorescence quenching to study the adsorption of BSA on differently functionalized gold nanoparticles.<sup>138</sup> They found similar binding constants for all NPs independent of the surface functionalization, which indicates the stickiness of the protein. Following this approach, Bunz et al. used the quenching effect to study the exchange of green fluorescent protein by serum proteins in gold nanoparticle based sensor platforms.<sup>139</sup> Röcker et al. have quantitatively analysed the adsorption of HSA onto polymer-coated FePt and CdSe/ZnS nanoparticles by using fluorescence correlation spectroscopy.<sup>37</sup> It was shown, that HSA binds by forming a monolayer of a few nm thickness. Moreover, time-resolved fluorescence quenching experiments revealed, that HSA binds the NP for  $\approx 100$ s. With the same method Maffre et al. investigated the adsorption of three plasma proteins onto polymer-coated FePt nanoparticles. For all three proteins, a step-wise increase in hydrodynamic radius with protein concentration was observed in accordance with their molecular shapes.<sup>38</sup>

In this thesis the quenching of a pH sensitive protein label - fluorescein - is used to determine the amount of adsorbed proteins onto the negatively charged microgel. The method was developed by Welsch et al.<sup>98</sup> and was already used to determine the adsorption isotherms of lysozyme adsorbing on negatively charged core-shell microgels. The compound shows high fluorescence at neutral and alkaline conditions whereas the fluorescence intensity drops in more acidic solutions due to different protonation states. Because of its high quantum yield and sensitivity fluorescein is frequently used to measure the pH of intracellular compartments.<sup>140</sup> The addition of fluorescein-labelled protein to the microgel strongly decreases the fluorescence signal. The decrease is probably a combination of two major effects. The first one is a quenching effect, which is due to a local pH difference between the microgel network and the bulk solution. In particular, the concentration of protons located in the microgel is expected to be higher and the environment becomes more acidic. This leads to a fast protonation of fluorescein as soon as the labelled protein approaches the surface layer of the particle. The second effect can be traced back to self-quenching of fluorescein due to a resonance energy transfer (homo RET). This effect will be more pronounced at higher protein load, because the Förster distance for homo RET between the fluorescein molecules is in the order of the protein diameter (42-56 Å).<sup>141,142</sup> In general, labeling a protein can change its conformation, which may lead to reduced function and activity. It was previously determined that a 1:1 labeling ratio between fluorescein and lysozyme is sufficient and keeps its activity around 70%.<sup>98</sup>

In summary, a combination of two quenching effects will decrease the fluorescence signal for adsorbing proteins, while desorbing proteins, which compete for binding sites on the microgel, will increase the signal. By this means the amount of adsorbed protein can be monitored over time. Figure 3.11 b shows a general scheme of the fluorescence experiment in the case of a binary protein mixture. In a time-dependent fluorescence experiment it was already shown, that a 1:1 mixture of labelled and unlabelled lysozyme and vice versa will lead to the same intensity.<sup>98</sup> It can therefore be concluded, that protein binding to the charged microgel is a reversible process and all components are in equilibrium.

### 3.4 The Cooperative Binding Model (CB-model)

Yigit et al. developed a coarse-grained model, hereafter referred as cooperative binding model (CB-model), to describe the protein adsorption to charged, polymer-coated nanoparticles.<sup>59</sup> It was already demonstrated that under equilibrium conditions the model is able to rationalize the adsorption thermodynamics of lysozyme onto PNIPAM coated NPs and separate interactions into non-specific, global electrostatic and protein specific.<sup>59</sup> The proteins and the NPs are treated as charged spheres. In this case the global electrostatic interactions can be tackled with a Poisson-Boltzmann approach. Protein interactions are described as pair interactions on the level of the second virial coefficient. The non-specific interactions are represented as a free energy  $\Delta G_0$  which is extracted from the adsorption isotherm obtained by isothermal titration calorimetry. It was shown that  $\Delta G_0$  is virtually salt-independent and includes contributions from hydrophobic forces.<sup>59</sup> In case of multi-component adsorption the model by Yigit et al. uses  $\Delta G_0$  as the only fit parameter. In addition, this model can also describe the adsorption kinetics



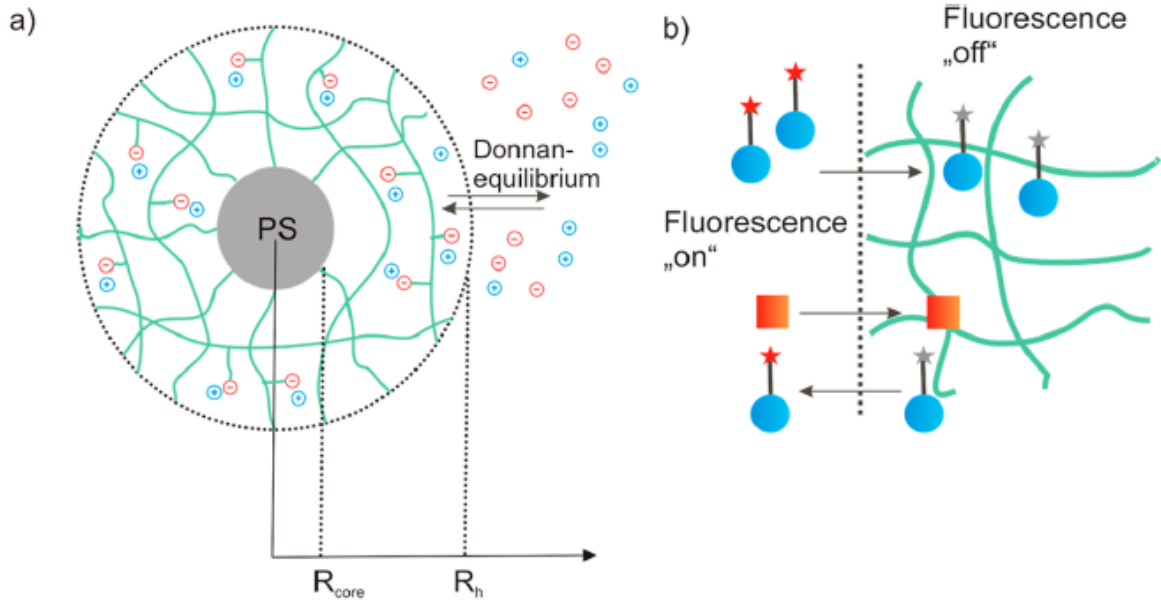


Figure 3.11: General scheme of the fluorescence-based competitive adsorption experiment in the case of a binary protein mixture. a) The Core-shell microgel is depicted with the radius of the polystyrene core  $R_{core}$  and with the hydrodynamic radius  $R_h$  of the entire colloid. The size of the colloid specifically depends on external conditions like salt concentration and the protein load. The system maintains its overall charge neutrality by a Donnan equilibrium. Basically, for all fluorescence experiments the microgel NW15 was used with  $R_h \approx 70nm$  and  $R_h \approx 180nm$  as determined by DLS in 10 mM MOPS, 2 mM  $NaN_3$  solution at pH = 7.2 and at 298K. b) The fluorescence of the labeled protein<sup>FITC</sup> (blue spheres) shows a significant decrease in intensity as it enters the microgel network. Sequential adsorption of a second competing protein (red rectangles) will increase the fluorescence signal proportional to the number of released protein<sup>FITC</sup> in solution.

of globular proteins onto poly(NIPAM) coated NPs on the basis of Dynamic Density Functional Theory (DDFT).<sup>99</sup>

Figure 3.12 shows the simplified procedure how the cooperative binding model for one protein type (one-component case) and for more than one protein type (multi-component case) is applied. In the one-component case the calculation needs the protein specific values, radius  $R_p$ , charge  $z_p$  and the second virial coefficient  $B_2$ , which are either known from literature or are accessible by scattering techniques. Providing microgel properties and bulk properties are known, the number of bound protein  $N_i$ ,  $\Delta G_{el,i}$  and  $\beta\mu$  can be calculated with the CB-model using  $\Delta G_0$  as the only fit parameter. The principle in the multi-component case is similar except that  $\Delta G_0$  for every single protein type needs to be determined.

### 3.4.1 Derivation of the Cooperative Binding Model

In the model the distribution of proteins between microgel and bulk solution is described by the central equation

$$(3.30) \quad \frac{N_i}{V_g} = c_i \cdot \exp[-\beta\Delta G_{el,i}(N_i) - \beta\Delta G_{0,i}] \exp[-\beta\mu_i(N_i)] = c_i \cdot \exp[-\beta\Delta G_{tot,i}]$$

where  $N_i/V_g$  is the number density of the  $i$ -th type protein from a multicomponent protein mixture with  $V_g$  being the volume of the microgel. The number density is calculated from the total free energy  $\Delta G_{tot,i}$

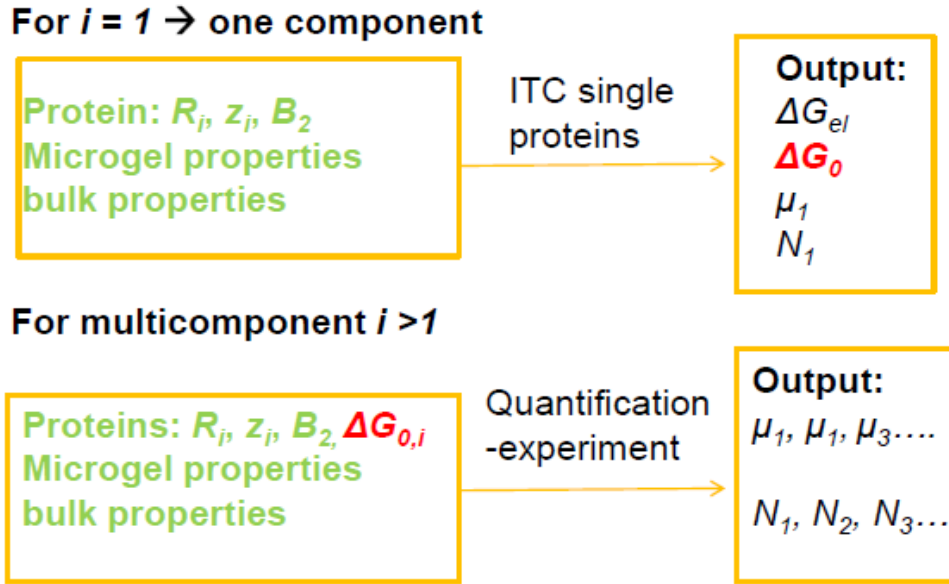


Figure 3.12: Simplified scheme of the Cooperative Binding Model (CB-Model) applied in the one-component and multi-component case.

composed of three terms with term i)  $\Delta G_{el,i}$  considering electrostatic interactions, term ii)  $\Delta G_{0,i}$  being a non-electrostatic, protein specific interaction and term iii)  $\beta\mu$  accounting for protein-protein interactions. Here,  $\Delta G_{el,i}$  and  $\beta\mu$  are functions of the protein load  $N_i$  itself and cooperative effects are not unlikely.

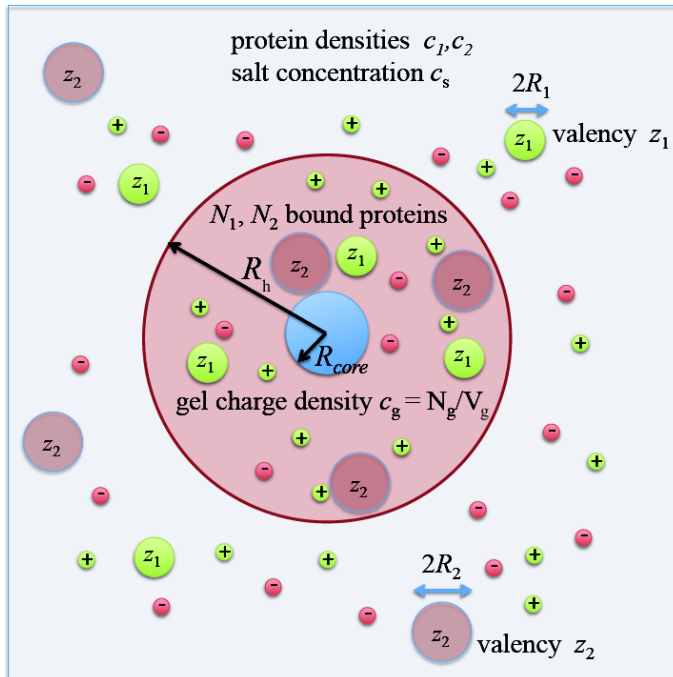


Figure 3.13: Sketch of the core-shell microgel in a binary mixture of proteins with concentrations  $c_1$  and  $c_2$ , valencies  $z_1$  and  $z_2$  and radii  $R_1$  and  $R_2$ . Reprinted from reference<sup>122</sup>

In the cooperative binding model the microgel is considered as a sphere with an overall radius  $R_h$  in a binary protein mixture with the protein densities  $c_1$  and  $c_2$  (see Figure 3.13). In table 7.1 in the appendix frequently used constants and variables are listed for the sake of clarity.

The radius of the polystyrene core is fixed with  $R_{core} \approx 60$  nm. The core-shell microgel is immersed in a monovalent salt medium with  $c_s = c_+ = c_-$  with  $c_+$  and  $c_-$  the concentrations of cations and anions, respectively. Proteins are depicted as charged monopolar spheres with an experimentally determined radius  $R_i$  and charged  $z_i$ . Non electrostatic contributions as well as contributions from dipolar and multipolar interactions are neglected. The overall radius  $R_h$  varies from  $\approx 130$ -180 nm de-

pending on salt and/or protein concentrations. The charged polymeric network of the shell has a volume of  $V_g = 4\pi(R_h^3 - R_{core}^3)$  and is the only part accessible for the protein uptake. By incorporating units of acrylic acid the network is weakly negatively charged at neutral pH (weakly dissociated polyelectrolyte). Conductometric and potentiometric measurements revealed an incorporation of  $N_g = 4.9 \cdot 10^5$  charged units per microgel.

The Bjerrum length  $l_B = \frac{e^2}{4\pi\epsilon\epsilon_0 k_B T}$  is defined as the separation distance of two elementary charges where the electrostatic energy is the thermal energy. In this system  $l_B = 0.7$  nm, i.e. the Bjerrum length of water. The mean separation between two charged monomers on the same polymer within the microgel is estimated about 2.2 nm. Thus, charge regulation effects in term of counterion condensation play a minor role and the charge valency of the monomers is  $z_g = -1$ . This leads to a total charge density of  $z_g c_g = z_g N_g / V_g$ . Furthermore, in agreement with small angle scattering data it is assumed that the charged units are homogeneously distributed in the network. The remaining parts of the microgel and buffers are treated as a continuum background with fixed dielectric, elastic and osmotic properties.

### 3.4.1.1 Electrostatic Interactions

Electrostatic interactions can not be neglected in the adsorption of proteins to a charged microgel network and are the most dominant contributions. The transfer of a charged protein in a salt bath with concentration  $c_s$  into the gel with the charge  $c_g$  is associated with a transfer in free energy of the particle. If we consider the proteins as polyelectrolytes with spherical symmetry the difference in free energy can be described through<sup>59</sup>

$$(3.31) \quad \beta \Delta G_{el,i} = z_i \Delta \phi(y) - \frac{z_i^2 l_B}{2R_i} \left( \frac{\kappa_g R_i}{1 + \kappa_g R_i} - \frac{\kappa_b R_i}{1 + \kappa_b R_i} \right)$$

with  $\kappa_g$  and  $\kappa_b$  defined as the inverse Debye Screening length. The first term accounts for the energy needed to transfer a charged protein against the difference in the electrostatic potential (Donnan potential) between the gel and bulk solution. The second term, the Born energy, relates to the difference in the energy of charging the sphere of radius  $R_i$  in bulk and gel because of the different screening properties in both media.

For weak perturbations i.e low salt concentration, low protein loading and not too high protein net charge the electrostatic interactions can be treated by the Poisson-Boltzmann cell model. In the cell model, the proteins are treated as homogeneously charged spheres with radius  $R_i$  and valency  $z_p$ . The proteins occupy a spherical cell with radius  $R_c$  and volume  $V_c$  and the dimension of the cell in terms of  $R_c$  is determined by the number of proteins  $N_i$  by the following relation:

$$(3.32) \quad R_c = \left( \frac{3V_c}{4\pi} \right)^{1/3} = \left( \frac{3V_c}{4\pi N_i} \right)^{1/3} \propto N_i^{1/3}$$

Each cell has a fixed number of charges  $N_c$  defined by the number of monomer charges and proteins  $N_c = N_g / N_i$ . Furthermore, each cell is in contact with the bulk solution containing a monovalent salt with the concentration  $c_s$ . Thus, on average the electroneutrality condition must be fulfilled by every cell.

$$(3.33) \quad c_s \exp(-\Delta \bar{\phi}) - c_s \exp(\Delta \bar{\phi}) + z_g c_g + z_p N_i / V = 0$$

If we neglect the small protein concentration outside the gel the solution for  $\delta\bar{\phi}$  is the modified Donnan potential as defined already defined in equation 3.3. The Donnan potential originates from an unequal distribution of ions between bulk and microgel which causes a mean electrostatic potential compared to the bulk reference state  $\phi = 0$ . For the proteins inside the cell we assume, that the gel network behaves fluid-like and the charge entities are comparable to mobile counterions to the proteins. Hence, the Poisson-Boltzmann equation in spherical coordinates can be applied to these system written as

$$(3.34) \quad \frac{1}{r}(r\bar{\phi})'' = -4\pi l_B \left[ (z_g c \exp(-z_g \bar{\phi}_1) - c_s \exp(\Delta\bar{\phi} + \bar{\phi}_1) + c_s \exp(-\Delta\bar{\phi} - \bar{\phi}_1)) \right]$$

where  $\Delta\bar{\phi}$  is the modified Donnan potential defined in equation 3.3 and  $\phi_1$  is a perturbation caused by the adsorbing proteins. The constant  $c$  is defined via the overall charge number  $N_c$

$$(3.35) \quad N_c = \int_{V_c} d^3r \exp(-z_g \bar{\phi}_1)$$

For small perturbations  $\bar{\phi}_1 \ll 1$  as it is the case for a weakly charged protein equation (3.34) can be linearized.

$$(3.36) \quad \frac{1}{r}(r\bar{\phi})'' = 4\pi l_B z_i N_i / V_g + \kappa^2(\bar{\phi} - \Delta\bar{\phi})$$

We define  $\kappa = \sqrt{4\pi l_B c_{in}}$  as the internal inverse screening length with  $c_{in} = c_g + c_s \exp(-\Delta\bar{\phi}) + c_s \exp(\Delta\bar{\phi})$ . The final solution of equation (3.36) is:

$$(3.37) \quad \bar{\phi}(r) = \Delta\bar{\phi} - z_i N_i / (V c_{in}) + A \frac{\exp -\kappa r}{r} + B \frac{\exp -\kappa r}{r}$$

with the constants:

$$A = \frac{z_i l_B \exp \kappa R_i}{1 + \kappa R_i} \left[ 1 - \exp -2\kappa(R_c - R_i) \frac{(\kappa R_i - 1)(\kappa R_c - 1)}{(\kappa R_i + 1)(\kappa R_c + 1)} \right]$$

$$B = \frac{z_i l_B}{1 + \kappa R_i} \left[ \exp \kappa(2R_c - R_i) \frac{(\kappa R_i - 1)(\kappa R_c - 1)}{(\kappa R_i + 1)(\kappa R_c + 1)} \right]$$

Since we assume a large cell size ( $R_c \rightarrow \infty$ ) or a low protein load ( $N_i \rightarrow 0$ ), respectively, it follows that  $B \rightarrow 0$ , and  $A \rightarrow z_i l_B \exp(\kappa R_i) / (1 + \kappa R_i)$ . Thus, equation 3.37 can be simplified to

$$(3.38) \quad \bar{\phi}(r) = \Delta\bar{\phi} - z_i N_i / (V c_{in}) + \frac{z_i l_B}{1 + \kappa R_i} \frac{\exp -\kappa(r - R_i)}{r}$$

With the co-ion concentration in the microgel expected to be rather small, that is  $c_{in} \simeq c_g$ , a further simplification to equation 3.38 is made leading to

$$(3.39) \quad \bar{\phi}(r) = \frac{z_i l_B}{1 + \kappa_b R_i} \frac{\exp -\kappa(r - R_i)}{r}$$

where  $\kappa_b$  is the inverse screening length in the gel  $\kappa_b = \sqrt{8\pi l_B c_g}$ . Following this theoretical framework the free energy or Gibbs energy  $\Delta G$  is simply the difference of work needed to transfer a sphere charged  $z_i$  from bulk solution to the gel against different surface potentials.

$$(3.40) \quad \beta \Delta G = \int_0^{z_i} dz_i [\phi_g(R_i) - \phi_b(R_i)]$$

In the low salt and low protein load limit the leading order contributions can be summarized to:

$$(3.41) \quad \beta\Delta G_{el,i} = z_i\Delta\bar{\phi} - \frac{z_i^2 N_i}{2c_g V_g} - \frac{z_i^2 l_B}{2R_i} \left( \frac{\kappa_g R_i}{1 + \kappa_g R_i} - \frac{\kappa_b R_i}{1 + \kappa_b R_i} \right)$$

So far the free energy only considers ionic contributions to fixed lattices. However, the proteins are not confined and behave fluid-like. The free energy needs to be corrected for protein-protein interactions in terms of an excess chemical potential  $\mu$ .

### 3.4.1.2 Pair Interactions

The third term in equation 3.30, namely  $\mu_i$ , considers excluded volume interactions (pair interaction) between the densely packed hard spheres (proteins). In contrast, to the Langmuir model the proteins are not condensed to fixed binding sites and are allowed to move translational within the microgel under the restraint of pair interactions. For a one-component hard sphere system with  $i = 1$  the excluded volume term can be accurately expressed by the Carnahan-Starling potential<sup>143</sup>

$$(3.42) \quad \beta\mu_{CS} = \frac{8\eta - 9\eta^2 + 3\eta^3}{(1 - \eta)^3}$$

with the following definition of  $\eta = (N_i/V_g)\pi\sigma_i^3/6$ . The quantity  $\sigma_i = 2R_i$  is an effective hard sphere diameter. In the CB model it makes sense to replace the effective diameter by the diameter of gyration or hydrodynamic diameter, which are either known from literature or can be measured by scattering techniques. An expansion of the Carnahan-Starling potential to multi-component systems is not easy to obtain. However, in the limit of low protein loading  $\mu_i$  or  $\mu_{CS}$  can be expressed in terms of the second virial coefficient,<sup>59</sup> which can be calculated from  $\sigma_i$  via

$$(3.43) \quad B_2 = \frac{2}{3}\pi\sigma_i^3$$

in the case of one component or via

$$(3.44) \quad B_2^{ij} = \frac{2}{3}\pi \left[ \frac{\sigma_i + \sigma_j}{2} \right]^3$$

the second coefficient in case of two interacting proteins  $i$  and  $j$ . With this approximation we end up with the general equation:

$$(3.45) \quad \begin{aligned} \frac{N_i}{V_g} &= c_i \cdot \exp[-\beta\Delta G_{el,i}(N_i) - \beta\Delta G_{0,i}] \exp[-\beta\mu_i(N_i)] \\ &= c_i \cdot \exp[-\beta\Delta G_{el,i}(N_i) - \beta\Delta G_{0,i}] (1 - 2B_2 \frac{N_i}{V_g}) \end{aligned}$$

### 3.4.1.3 Volume Effects

As already described in detail in section 3.1.4 the volume of the microgel  $V_g$  is determined by the balance of osmotic and elastic pressure (see equation 3.4). However, it does not include contributions from the proteins being adsorbed. Addition of proteins will lower the total net charge and inhomogenize the charge distribution in the network. On the other side, the monomer charge density  $c_g = N_g/V$  increases with

shrinking and contributions from  $\Delta G_{el,i}$  will be affected. It is also conceivable that protein adsorption can swell the network again. Nevertheless, a theory covering the volume effects caused by protein adsorption was out of scope in this thesis and the protein specific volume shrinkage was described using the empirical formula

$$(3.46) \quad R_h(x) = \frac{R_{max} - R_{min}}{2} \left[ 1 - \tanh \frac{x - x_0}{\Delta} \right] + R_{min}$$

with  $R_h(x)$ , the hydrodynamic radius measured precisely in a DLS experiment.

In the multicomponent case the situation becomes even more challenging - e.g. the shrinkage might deviate compared to the one -component case - and the gel volume becomes a function the molar ratios of  $i$ -th proteins  $V_g = V_g(x_i)$ . In the case of a binary mixture the volumes are estimated by a linear interpolation of the form, which describes the measured data sufficiently.

$$(3.47) \quad V_g(x_1, x_2) = \frac{V_g(x_1) \cdot N_1 + V_g(x_2) \cdot N_2}{N_1 + N_2}$$

## 4 Results and Discussion

### 4.1 Binding Isotherms of Core-Shell Microgels to Single Proteins (ITC)

In Table 4.2 the main properties of the microgels are summarized. The microgels vary in size, the content of the charged copolymer acrylic acid and in the number of absolute charges per microgel particle. The synthesis for all microgels followed a two step procedure.<sup>75</sup> First the polystyrene core was synthesized by emulsion polymerisation. In a second step the shell is grafted on by seeded emulsion polymerisation (see further explanation in chapter 6). The microgels were cleaned by ultrafiltration and characterized by DLS, TEM and conductometric measurements as described in detail in chapter 6. Table 4.2 gives

Table 4.1: Microgels Overview

microgel	AAc [mol-%]	$M_w$ [g/mol]	$R_{core}$	$R_h$ [nm]	$N_g$
NW15	10	$1.18 \cdot 10^9$	$62.2 \pm 0.7$	$185 \pm 10$	$4.9 \cdot 10^5$
OM5UF	0	$1.21 \cdot 10^8$	$34 \pm 5$	$90 \pm 5$	0
OM6UF	7.5	$5.79 \cdot 10^9$	$100 \pm 7$	$284 \pm 7$	$2.66 \cdot 10^6$

$R_{core}$  = Hydrodynamic radius of PS-core,  $R_h$  = Hydrodynamic radius of microgel,  $N_g$  = number of charged units

an overview on the protein-microgel combinations for which ITC experiments were carried out. For microgel NW15 the adsorption isotherms were fitted by the Langmuir model and by the CB-model. For microgels OM5UF and OM6UF fitting with the Langmuir model was sufficient due to the fact that these microgels were not used for competitive adsorption experiments.

Table 4.2: Overview: Protein-microgel combinations for ITC Experiments

microgel	Langmuir Model	Cooperative Binding Model
NW15	Lysozyme, RNase A, Papain, Glucosidase, Cytochrome c	Lysozyme, RNase A, Papain, Cytochrome c
OM5UF	Cytochrome c	-
OM6UF	Lysozyme	-

#### 4.1.1 Langmuir Fits

Figure 4.1 shows the adsorption isotherms for cytochrome c binding to microgels NW15 and OM5UF at varying temperature. The binding isotherms were fitted with the Langmuir model. Thermodynamic parameters are listed in Table 4.3. The number of binding sites are all within the margin of error and

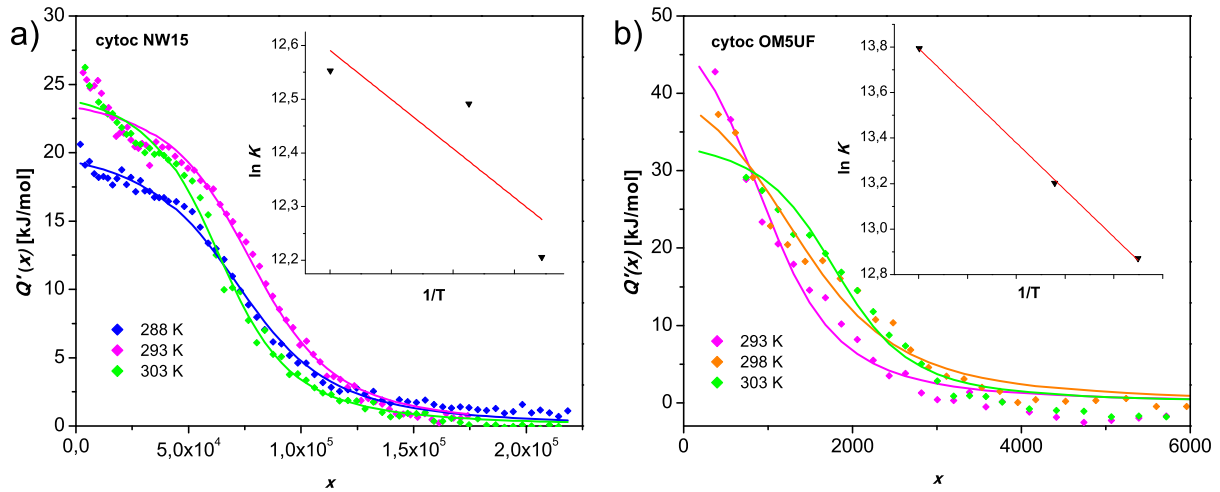


Figure 4.1: a) Binding isotherms of cytochrome c onto the charged microgel NW15 in 10 mM MOPS at pH = 7.2 at 288 K (blue), 293 K (magenta) and 303 K (green) and b) binding isotherms of cytochrome c onto the uncharged microgel OM5UF in same buffer at 293 K (magenta), 298 K (orange) and 303 K (green). Solid lines represent the Langmuir isotherm and  $\diamond$  are the experimental data points. The inset of the graphs shows the van't Hoff analysis of cytochrome c adsorption on the microgels.

Table 4.3: Adsorption of cytochrome c onto microgels NW15 and OM5UF at varying temperatures in 10 mM MOPS buffer, pH = 7.2. The overall salt strength is  $I = 7$  mM. Thermodynamic parameters were obtained by a Langmuir Fit.

Microgel	$T$ [K]	$N$	$K$ [ $M^{-1}$ ]	$\Delta H_{ITC}$ [kJ/mol]	$\Delta H_b$ [kJ/mol]
NW15	303	$66500 \pm 7400$	$2.8 \pm 0.3 \cdot 10^5$	$25 \pm 0.4$	
	293	$81500 \pm 9600$	$2.7 \pm 0.3 \cdot 10^5$	$24.5 \pm 0.4$	$15 \pm 9$
	288	$71100 \pm 7500$	$2.0 \pm 0.14 \cdot 10^5$	$20.3 \pm 0.3$	
OM5UF	303	$1820 \pm 88$	$9.8 \pm 3.4 \cdot 10^5$	$57 \pm 7$	
	298	$1470 \pm 95$	$5.42 \pm 1.8 \cdot 10^5$	$46 \pm 4$	$86 \pm 2$
	293	$1003 \pm 100$	$3.89 \pm 0.88 \cdot 10^5$	$35 \pm 3$	

correlate well with the proportions of protein and microgel. In comparison to lysozyme with  $N \approx 60.000$  the smaller cytochrome c saturates microgel NW15 at  $N \approx 73.000$  binding sites. For microgel OM5UF the number of binding sites is much smaller due to the smaller size of the microgel ( $R_h \approx 90nm$ ). Moreover, this microgel does not contain charged groups and proteins adsorption is mediated via non-electrostatic interactions. As in previous works it can be demonstrated that  $K$  varies systematically with temperature, but in this case with rather high error margins due the quality of the fits. The binding constant is slightly higher for OM5UF but still in the same order of magnitude. However,  $K$  increases considerably with increasing temperature indicating strong hydrophobic interactions. It is well known that as temperature increases, the strength of hydrophobic interactions increases also. Binding of the proteins is endothermic for both microgels with  $\Delta H_{ITC} > 0$ .

At this point it is necessary to discuss the values of  $\Delta H_{ITC}$  in Table 4.3.  $\Delta H_{ITC}$  represents the overall heat of a titration process and includes heat contributions which may not exclusively being related to the binding enthalpy. Such contributions can be traced back to protonation effects, conformational changes,



and possible side contributions other than "pure" protein binding. Consequently, the enthalpy measured by ITC can be expressed as a sum of the binding enthalpy  $\Delta H_b$  and some residual enthalpy  $\Delta H_{res}$  which accounts for all effects not related to the "pure" protein binding.<sup>68</sup>

$$(4.1) \quad \Delta H_{ITC} = \Delta H_b + \Delta H_{res}$$

The binding enthalpy  $\Delta H_b$  can be extracted from the van't Hoff relation, i.e. the temperature dependence of  $K$  defined as

$$(4.2) \quad \left( \frac{d(\ln K)}{dT^{-1}} \right)_p = -\frac{\Delta H_b}{R}$$

The difference between  $\Delta H_{ITC}$  and van't Hoff enthalpy is system-specific. In some cases they do not differ from each other significantly, while in other cases the differences can be large. For example, the adsorption of RNase A onto a spherical electrolyte brush was endothermic with  $\Delta H_{ITC} > 0$  while  $\Delta H_b$  was negligibly small, i.e.  $K$  is temperature-invariant. This led to the conclusion that  $\Delta H_{ITC}$  and  $K$  were not related to the same equilibrium process<sup>91</sup> and  $\Delta H_{ITC}$  originated from processes other than protein binding. Similarly, by analysis of both enthalpies Welsch et al. could proof an additional protonation reaction of the adsorbed lysozyme which contributed to  $\Delta H_{ITC}$  (see section 3.2.1).<sup>68</sup> The van't Hoff plots of cytochrome c adsorbing onto NW15 and OM5UF are shown in the insets of Figure 4.1. From the slope of the regression line  $\Delta H_b$  was calculated with  $15 \pm 9$  kJ/mol for NW15 and  $86 \pm 2$  kJ/mol for OM5UF (see Table 4.3). In this case  $\Delta H_b$  differs about a factor of 6 indicating a strong binding of cytochrome c to microgel OM5UF. In this case, the adsorption probably is accompanied by a strong exothermic reaction like a deprotonation step or unfolding of the protein because  $\Delta H_b$  is higher than  $\Delta H_{ITC}$ .

Besides temperature the adsorption of proteins to charged microgels strongly depend on the salt concentration. Figure 4.2 shows the adsorption isotherms for cytochrome c and glucosidase binding to microgel NW15 at varying salt strength. The inset of the graph shows the shrinkage of the microgel with respect to the molar ratio  $x$ . Experimental values for  $R_h$  for both proteins ( $\blacktriangledown$ ) at 7 mM ionic strength and 298 K as measured by DLS. The solid line is a fit according to equation 3.46. Experimental values ( $\blacklozenge$ ) from ITC measurements were fitted with a Langmuir isotherm and the values for  $N$ ,  $K$ , and  $\Delta H_{ITC}$  are listed in Table 4.4. Cytochrome c is a small rather globular protein with a positive netcharge at pH = 7.2.

Table 4.4: Adsorption of cytochrome c and glucosidase onto NW15 microgel at varying ionic strength in 10 mM MOPS buffer, pH = 7.2 and at T = 298 K. Thermodynamic parameters were obtained by a Langmuir Fit.

Protein	Ionic strength [mM]	$N$	$K$ [ $M^{-1}$ ]	$\Delta H_{ITC}$ [kJ/mol]
Cytochrome c	7	$68900 \pm 640$	$2.8 \pm 0.2 \cdot 10^5$	$25 \pm 1$
	17	$35100 \pm 830$	$1.44 \pm 0.14 \cdot 10^5$	$31 \pm 1$
	32	$9240 \pm 3900$	$5.6 \pm 1.1 \cdot 10^4$	$60 \pm 27$
Glucosidase	7	$10200 \pm 91$	$3.5 \pm 0.3 \cdot 10^6$	$113 \pm 2$
	17	$8340 \pm 320$	$6.4 \pm 1 \cdot 10^5$	$157 \pm 9$
	32	$11100 \pm 210$	$1.0 \pm 0.1 \cdot 10^6$	$163 \pm 4$

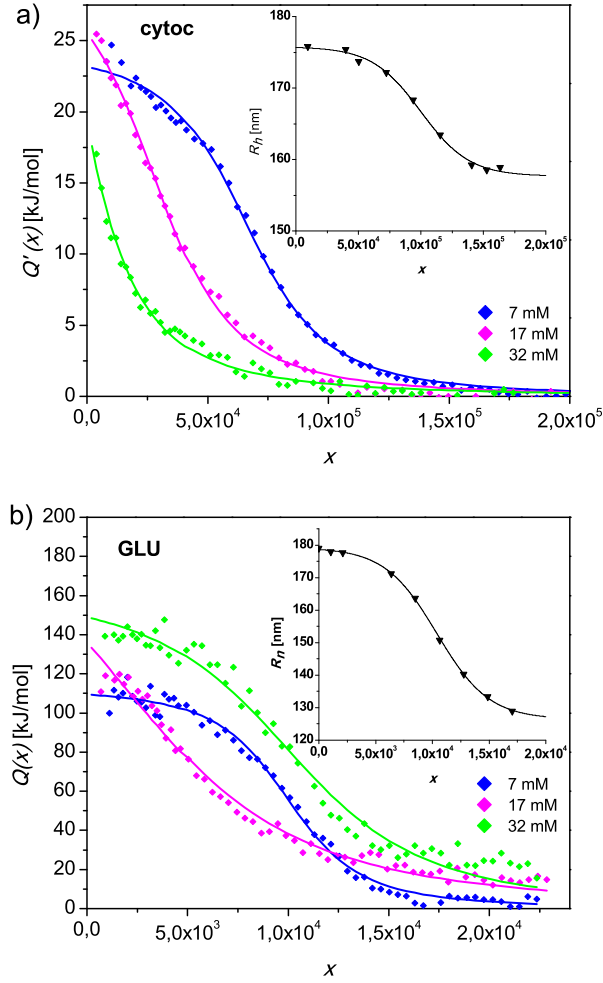


Figure 4.2: Adsorption isotherms of a) Cytochrome c and b) Glucosidase. The differential heat  $Q(x)$  (kJ/mol) is plotted versus the molar ratio  $x$  of the protein measured at 7 mM (blue), 17 mM (magenta) and 32 mM (green) ionic strength and 298 K. See further explanation in the text.

At 7 mM ionic strength the number of binding sites  $N$  is  $\approx 70.000$ . This packing density correlates well with the size of the protein. Increasing the ionic strength leads to a significant decrease in the number of binding sites and the binding strength  $K$ . The same trend can also be observed for lysozyme which has been studied extensively in previous works.<sup>68,81</sup> This effect can be traced back to screening interactions which finally lower the Donnan potential and reduce the electrostatic attraction between protein and microgel (see section 3.1.3). Despite the fact that lysozyme and cytochrome c have roughly the same size and netcharge the binding strength is about one order of magnitude lower for cytochrome c ( $K(\text{Lysozyme}) = 2.6 \cdot 10^6 [\text{M}^{-1}]$  and  $K(\text{cytochrome c}) = 2.8 \cdot 10^5$  at 298 K and 7 mM ionic strength). Consequently, non electrostatic effects like the charge distribution on the protein surface as well as specific interactions, such as hydrophobic binding, are also decisive for the thermodynamics of adsorption. However, the incorporation of such contributions is not possible within Langmuir model and a detailed analysis including a quantitative assignment of different driving forces using another model will follow in the next section.

Glucosidase binds endothermic to the microgel with  $\Delta H > 0$  for all salt strengths ( $I = 7, 17, 32$  mM).

The protein occurs as a homodimer with a molecular weight of  $M_w \approx 130.000$ . At nearly neutral pH as used in the experiments the protein has an overall negative netcharge with an isoelectric point at 4.4. It was already discussed in section 3.1.3 that proteins can adsorb a negatively charged polymeric network from the "wrong side" of the isoelectric point. Generally, the adsorption of like charge proteins is driven either entropically by counterion release if Manning condensation is possible or by charge regulation of the protein. In this particular case the microgel is a weakly charged polyelectrolyte and Manning condensation does not occur.

In contrast to cytochrome c the adsorption isotherms of glucosidase are not easy to interpret since the values of  $K$  and  $N$  do not vary systematically with increasing salt concentrations and show a maximum at  $I = 32$  mM. An explanation for the unusual trend in  $K$  and  $N$  initially was traced back to a dimer-monomer equilibrium for glucosidase. In particular, glucosidase was assumed to form a dimer at  $I = 7$  mM and a monomer at  $I = 32$  mM. To proof this assumption small angle scattering experiments were performed to elucidate the size of glucosidase in terms of the gyration radii  $R_g$  at varying ionic strength.

In Figure 4.3 a-d the SAXS intensity profiles for glucosidase and the Guinier plots are shown.  $R_g$  was extracted by Guinier analysis with  $3.3 \pm 0.2$  nm for  $I = 7$  mM and  $3.2 \pm 0.2$  nm for  $I = 100$  mM. Thus, a switch between dimer and monomer within this range in ionic strength does not occur and the different adsorption behaviour of glucosidase can either be traced back to charge regulation or some other effect which have been not treated within present models.

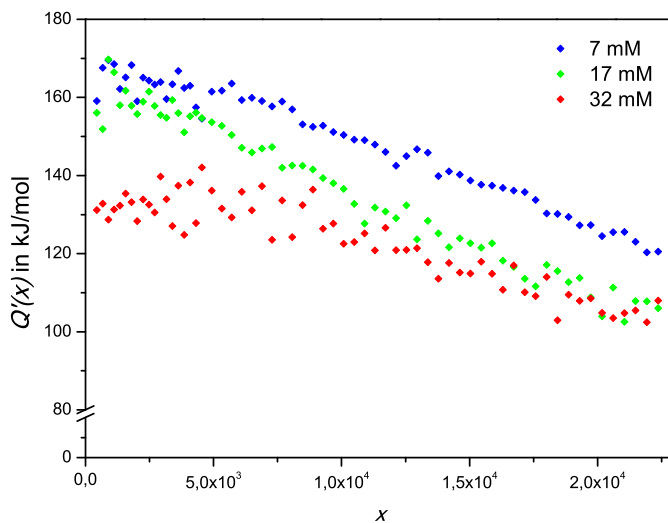


Figure 4.4: Heats of dilution for glucosidase measured by ITC at different salt strength in 10 mM MOPS at pH = 7.2 at 298 K

It was already discussed in section 3.2.1 that the heat of dilution can be a critical parameter to obtain a good quality of the isotherm. Figure 4.4 shows the heats of dilution for glucosidase measured at different salt strengths in 10 mM MOPS buffer. The heat of dilution is endothermic and shows values up to 170 kJ/mol. This is about a factor of ten higher compared to the heats of dilution of proteins like lysozyme or cytochrome c. The effect can be explained by the bigger size of the molecule. Moreover, it can be concluded that the heat of dilution is not a constant, but decreases with increasing ionic strength. Here, water-

mediated effects between the protein and salt molecules change the solubility of the protein and thus the heat of dilution. Finally, the heat of dilution decreases with increasing injections of the protein solution. As explained in section 3.2.1 addition of more protein influences the ionic strengths of the solution which influences the activity coefficients for the already dissolved ions.

The microgel OM6UF was chosen for atomic force microscopy measurements. Thermodynamic parameters for the adsorption of lysozyme onto OM6UF at 298 K were obtained by fitting the ITC isotherm

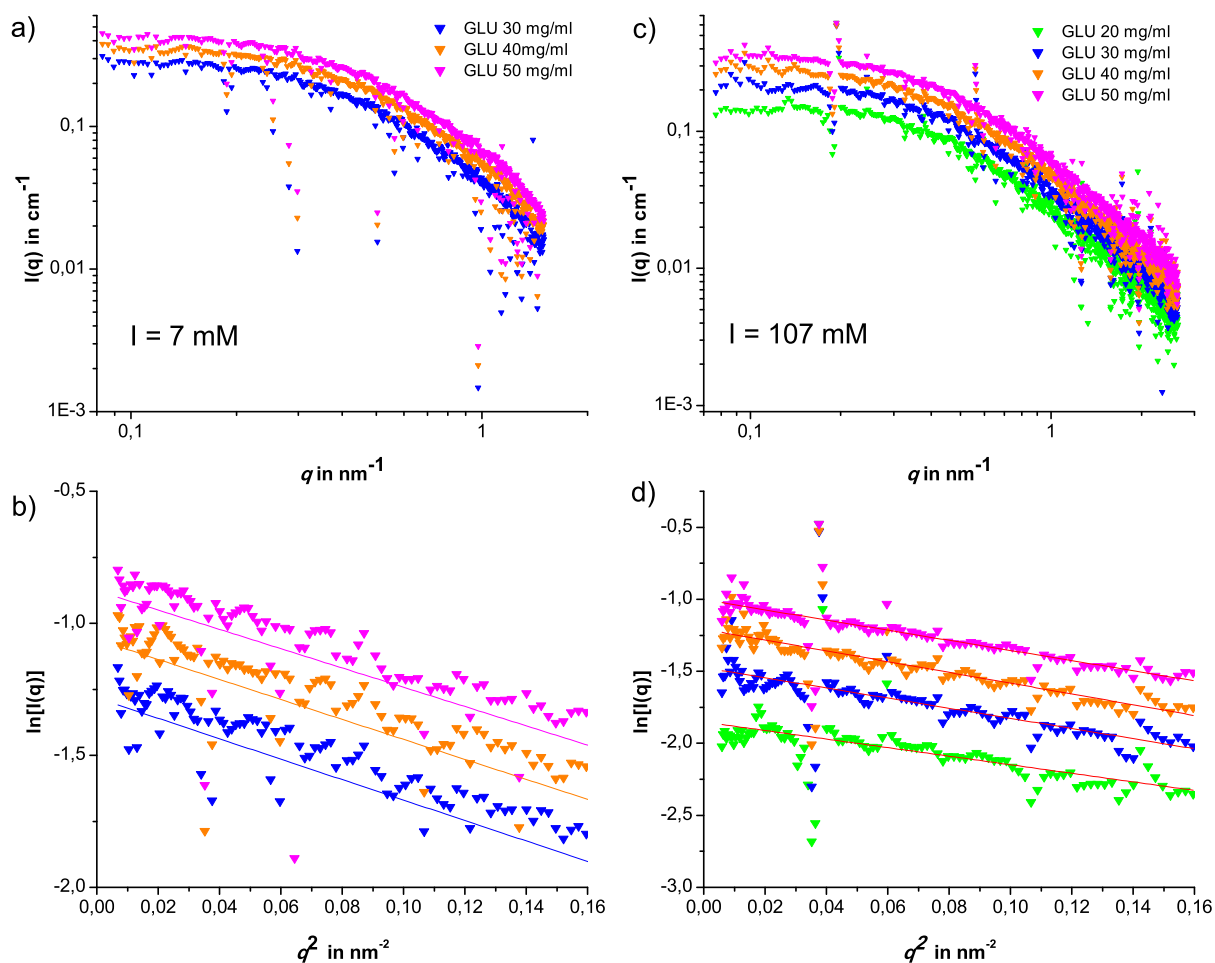


Figure 4.3: SAXS intensity profiles  $I(q)$  for Glucosidase in 10 mM MOPS at pH 7.2 and a) for varying protein concentrations and 10 mM NaCl added ( $I = 7$  mM) b) and corresponding Guinier plot  $\ln[I(q)]$  vs.  $q^2$ . c) scattering profile for varying concentrations and 100 mM NaCl added ( $I = 107$  mM) and d) corresponding Guinier plot. All measurements were taken at  $T = 298$  K.

in Figure 4.5 a with the Langmuir model. Values for  $N$ ,  $K$  and  $\Delta H$  are listed in the graph. The inset graph in Figure 4.5 a shows the volume shrinkage of the microgel induced by the modified Donnan potential.

Figure 4.5b illustrates the relation between size and the number of binding sites for the three different microgels. It can be concluded that the uptake of protein scales linear with their size.

In summary, it was shown that the adsorption isotherm for single types of proteins binding to core-shell microgels can be fitted with the Langmuir model and general trends concerning the binding process can be derived from this approach. For instance, the binding constant  $K$  and the number of binding sites  $N$  critically depend on temperature and ionic strength. Moreover, van't Hoff analysis showed that the enthalpies  $\Delta H_b$  can differ from  $\Delta H_{ITC}$  significantly. In this case  $\Delta H_{ITC}$  does not only originate from the pure protein binding but also includes effects like protonations and conformational rearrangements of the protein.

However, the Langmuir model was not able to extract more quantitative information on the binding processes. In particular, it was shown that the binding affinities of cytochrome c and lysozyme vary

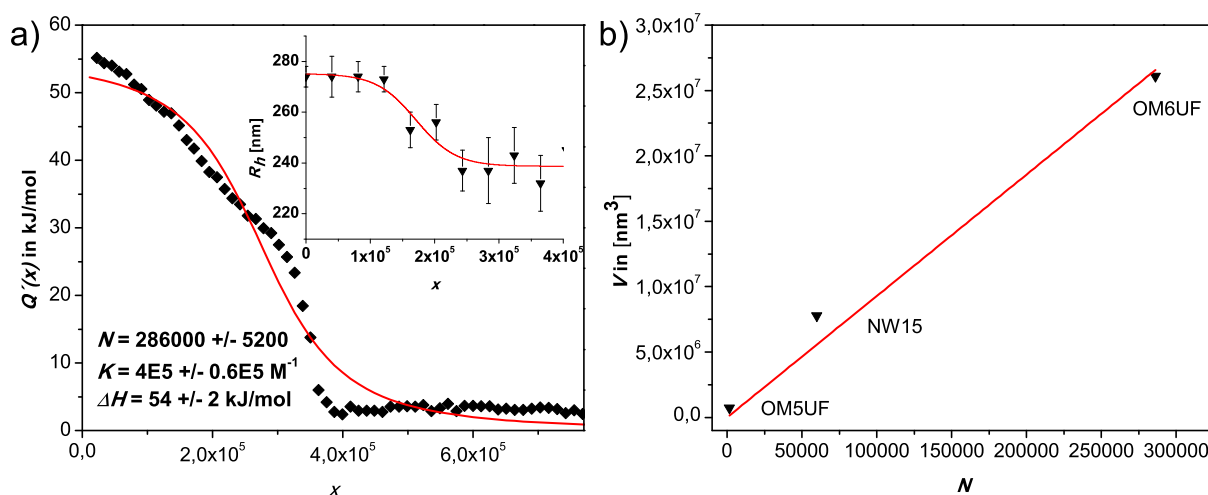


Figure 4.5: a) Adsorption isotherm for lysozyme onto OM6UF microgel particles in 10 mM MOPS at pH = 7.2 and T = 298 K. Solid lines represent the Langmuir isotherm and  $\blacklozenge$  are the experimental data points. In the inset of the graph the hydrodynamic radius is plotted against the molar ratio. b) Relation between microgel volume and number of binding sites for lysozyme.

about one order of magnitude, although the proteins are nearly similar in charge and size. A detailed explanation of this effect cannot be provided on the basis of the Langmuir model. Thus, in the following chapter the cooperative binding model is applied to fit the adsorption isotherms. As explained in section 3.4 the CB-model is able to evaluate electrostatic and intrinsic contributions to the binding free energy by fitting the isotherm and thus provides a more quantitative description of protein binding.

#### 4.1.2 Cooperative Binding Model Fits

In this chapter the adsorption isotherms of the proteins lysozyme, cytochrome c, papain, and RNase A onto core-shell microgel NW15 are analyzed with the CB-binding model. Glucosidase was not chosen as a model protein since as already discussed in section 4.1.1 the adsorption isotherms showed an unusual adsorption behavior, i.e. the binding affinity in terms of  $K$  did not vary systematically with increasing salt strength.

The analysis of the adsorption isotherms of lysozyme, cytochrome c, papain, and RNase A demonstrates a strong binding of these proteins. The resulting binding isotherms and bound proteins at 7 mM ionic strength are presented in Figure 4.6 while the corresponding binding parameters are summarized in Table 4.5. As shown in Figure 4.6 the uptake of all proteins by the microgel is endothermic, since  $\Delta H \geq 0$ . For large molar ratios  $x > 10^5$ , saturation takes place and ultimately leads to ca. 65 000 bound lysozyme, ca. 70 000 bound cytochrome c and RNase A, and ca. 50 000 bound papain molecules. The inset in Figure 4.6 shows the shrinkage of the microgel upon protein adsorption in terms of the molar ratio  $x$ . All four proteins lead to a different response of the microgel network. Lysozyme and papain lead to shrinkage up to 25%, but the effect is significantly less pronounced for RNase A and cytochrome with 5% and 10%, respectively. For the adsorption of papain, aggregates were noticed at molar ratios higher than  $x = 80.000$  and all further experiments with papain were carried out not exceeding this molar ratio.

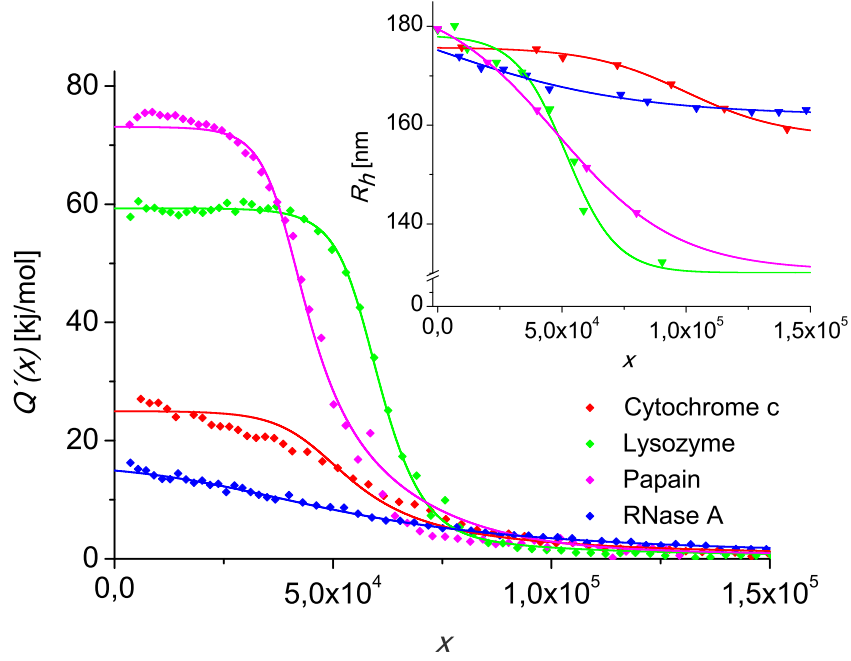


Figure 4.6: Adsorption isotherms of four proteins measured at 7 mM ionic strength and 298 K. The differential heat  $Q'(x)$  (kJ/mol) is plotted versus the molar ratio  $x$  of papain (magenta), lysozyme (green), cytochrome c (red), and RNase A (blue). Experimental values ( $\diamond$ ) from ITC measurements were fitted with equation 3.30. The inset of the graph shows the shrinkage of the microgel NW15 with respect to the molar ratio  $x$  for all four proteins at 7 mM ionic strength and 298 K. The points correspond to experimental values measured by DLS, while the solid lines are empirical fits according to equation 3.46.

Table 4.5: Results for the adsorption isotherms of single proteins onto NW15 microgel particles at 298 K and pH 7.2 using the cooperative binding model

protein	$R_i$ [nm]	$z_i$ [e]	$\Delta H_{ITC}$ [kJ/mol]	$N_i$	$\Delta G_{0,i}[k_b T]$
lysozyme	1.9 (1.9) <sup>a</sup>	+7 (+7) <sup>b</sup>	59	65000	-6.5
papain	2.2 (2.0) <sup>a</sup>	+8 (+7) <sup>b</sup>	73	50000	-4.5
RNase	1.8 (1.9) <sup>a</sup>	+4 (+6) <sup>b</sup>	16	70000	-4.1
cytochrome c	1.7 (1.8) <sup>a</sup>	+6 (+7) <sup>b</sup>	25	70000	-4.7

<sup>a</sup>Hydrodynamic radii (literature values). <sup>b</sup>Protein charge calculated from crystal structure (PDB 193L, lysozyme; PDB 1PPN, papain; PDB 1AFU, RNase A; PDB 2B4Z, cytochrome c).

The adsorption of proteins on the microgel critically depends on the net charge  $z_i$  determined from the charged groups on the surface of the proteins. In order to assess the influence of this parameter in more detail, it is used as an adjustable parameter in the fits of the adsorption of a single protein. In Table 4.5 the net charges  $z_i$  as used in the cooperative binding model are compared to values calculated on the basis of structures with atomistic resolution taken from the Protein Data Bank (PDB). The results show that  $z_i$  agrees within an error of  $\pm 1$  with the data obtained from these isotherms. In principle,  $z_i$  can be taken directly from structural data and presents no adjustable parameter. In the case of lysozyme it has already been shown that the intrinsic binding energy  $\Delta G_0$  is constant and independent of the ionic strength.<sup>59</sup>

Although this trend has only been evaluated for lysozyme it is safe to assume that  $\Delta G_0$  for other proteins will show the same characteristics. Values of  $\Delta G_{0,i}$  vary from  $-6.5$  to  $-4 k_B T$ , which corresponds to 2-3 hydrophobic protein-poly(NIPAM) interactions, if methane-methane interactions are taken as reference with attractions on the order of  $2-3 k_B T$ .<sup>59</sup> The analysis of  $\Delta G_0$  also explains the different binding constants of lysozyme and cytochrome c as obtained from the Langmuir Model (see section 4.1.1). In particular, the stronger binding of lysozyme to the microgel results from an approximately  $2 k_B T$  lower intrinsic binding energy. Hence, non-electrostatic interactions are more pronounced for this protein.

In Table 4.5 the effective hard-core radius of protein  $i$ ,  $R_i$ , is compared to literature values of the hydrodynamic radius or radius of gyration. The packing density also depends on the size of the protein. Values do not differ more than  $\pm 0.2$  nm and in the case of lysozyme even match exactly. The results support the assumption that  $R_i$  can be approximated by the radius of gyration or hydrodynamic radius and can be used in the cooperative binding model without further adjustments.<sup>144–147</sup> The model also accounts for a weak dependence of  $R_i$  on ionic strength as already shown for lysozyme.<sup>59</sup>

The cooperative binding as defined with equation 3.30 splits the total binding affinity  $\Delta G_{tot,i}$  into its partial components. Thus, it is interesting to discuss the contribution of each component to  $\Delta G_{tot,i}$  at different molar ratios  $x$ . Figure 4.7 a presents the total binding affinity  $\Delta G_{tot,i}(x)$  of the four proteins at 7

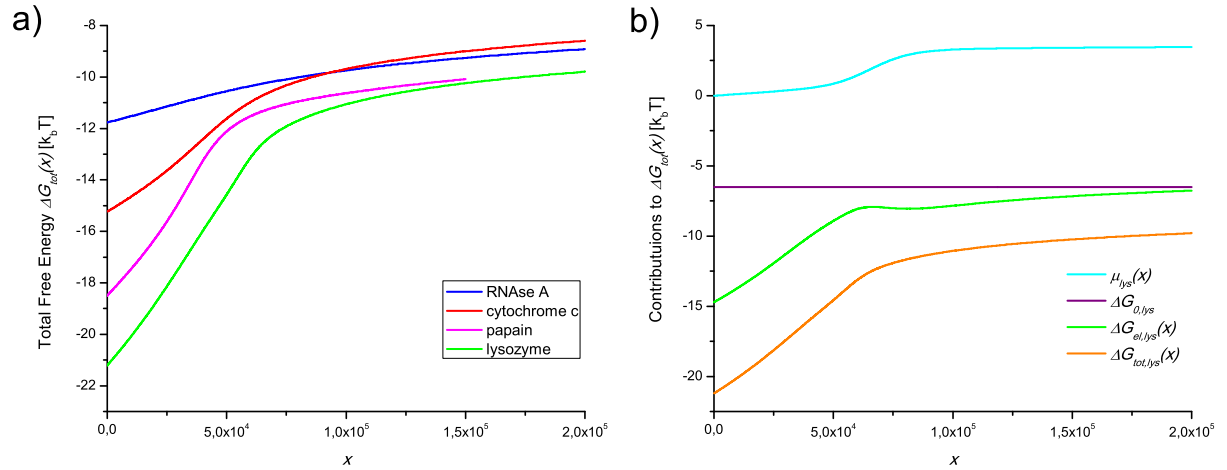


Figure 4.7: (a) Total free energy of binding  $\Delta G_{tot,i}(x)$  as a function of the molar ratio  $x$  at 7 mM ionic strength. At low molar ratios, lysozyme binds strongly to the microgel followed by papain, cytochrome c, and RNase A. (b) The binding affinity of lysozyme to the charged microgel is decomposed into its contributions.  $\Delta G_0$ , intrinsic adsorption free energy;  $\Delta G_{el}(x)$ , electrostatic contribution;  $\mu_{lys}(x)$ , the entropic penalty due to hard sphere packing

mM ionic strength as a function of molar ratio  $x$ . For all four proteins,  $\Delta G_{tot,i}(x)$  depends strongly on  $x$  as expected. At low molar ratios, the binding affinity of lysozyme and papain are the largest with about  $-21 k_B T$  and  $-18.5 k_B T$ , respectively. Cytochrome c and RNase A bind less strongly to the microgel, which is reflected by the parameters like lower  $\Delta G_0$  and lower charge  $z_i$ . It is notably that all four proteins saturate at a different value of  $\Delta G_{tot,i}(x)$  for high molar ratios. At first glance, this seems to appear unreasonable, since from equilibrium thermodynamics we would expect saturation at the same value of  $\Delta G_{tot,i}(x)$ . However, the calculation of  $\Delta G_{tot,i}(x)$  depends on the volume  $V_g$  (compare equation 3.30). Because  $V_g$  itself is a function of  $x$  and is specific for each type of protein,  $\Delta G_{tot,i}(x)$  saturates at different

values.

Figure 4.7 b shows the different contributions to the binding affinity done for lysozyme. By definition, the intrinsic adsorption free energy  $\Delta G_0$  is a constant contribution and incorporates local interactions, while the electrostatic  $\Delta G_{el,i}(x)$  and excluded-volume contributions depend explicitly on the molar ratio  $x$ . The excluded-volume contribution is negligible at low molar ratios but increases to approximately  $3 k_B T$  at higher  $x$ . Thus, it is clear that the electrostatic contribution is the main contributor to the binding affinity.

In summary, the CB-model showed a good performance to fit the adsorption isotherms of single type proteins obtained by ITC measurements. In contrast, to the Langmuir Model it was possible to get a more quantitative description of the adsorption process and the driving forces. In the CB-model the total adsorption free energy  $\Delta G_{tot,i}(x)$  originates from three different contributions, an electrostatic contribution  $\Delta G_{el,i}(x)$ , an intrinsic contribution  $\Delta G_0$  and  $\mu(x)$ , a contribution from packing effects. Moreover, the CB-model showed that  $\Delta G_{tot,i}(x)$  depends on the protein load expressed as molar ratio  $x$ . This is a marked contrast to the Langmuir model, in which the binding energy is calculated from the binding constant  $K$  being independent of the protein load.

## 4.2 Competitive Adsorption

So far only the adsorption of one component - i.e, only one type of protein was present in solution - was considered. However, adsorptions of one component adsorptions will not reflect a realistic scenario for a nanoparticle immersed in a biological fluid. Here, a multi-component mixture is present and the formation of a protein corona will depend on competitive and cooperative adsorptions. At this point the Langmuir model is definitely reaches its limits and the assumption of single and independent binding sites is not reasonable anymore.

In contrast, the CB-model is easily expandable to multi-component mixtures providing protein specific parameter like size as well as charge are known and the intrinsic binding energy  $\Delta G_0$  has been determined for each type of protein in the mixture. The theoretical framework of the CB-model including its expansion to multi-component mixtures has already been explained in section 3.4.

In Figure 4.8 the results of the competitive adsorption experiments for the proteins lysozyme, cytochrome c, papain and RNase A are shown. Experimental data were obtained by fluorescence spectroscopy. The details of the experiment have been already described in section 3.3.1.

Briefly described, the fluorescence of labeled lysozyme is quenched by binding to the microgel with a concomitant decrease in the fluorescence intensity. When a second protein is bound, a certain amount of labeled lysozyme is released into the bulk again, which can be seen from an increase of the intensity of the fluorescence. For the experiments labeled lysozyme (lysozyme<sup>FITC</sup>) is adsorbed onto the microgel in solution with a binding fraction of  $\Theta_1 \approx 0.6$ . The binding fraction for lysozyme<sup>FITC</sup> was calculated with the values from the Langmuir fit with  $N_{max} = 65\ 000$ . For the binding fraction of the other proteins  $\Theta_2$ , a mean value for the number of binding sites  $N_{max} = (N_1 + N_2)/2$  is assumed (compare Table 4.5 for the number of binding sites). First the competitive adsorption of unlabeled lysozyme to a microgel



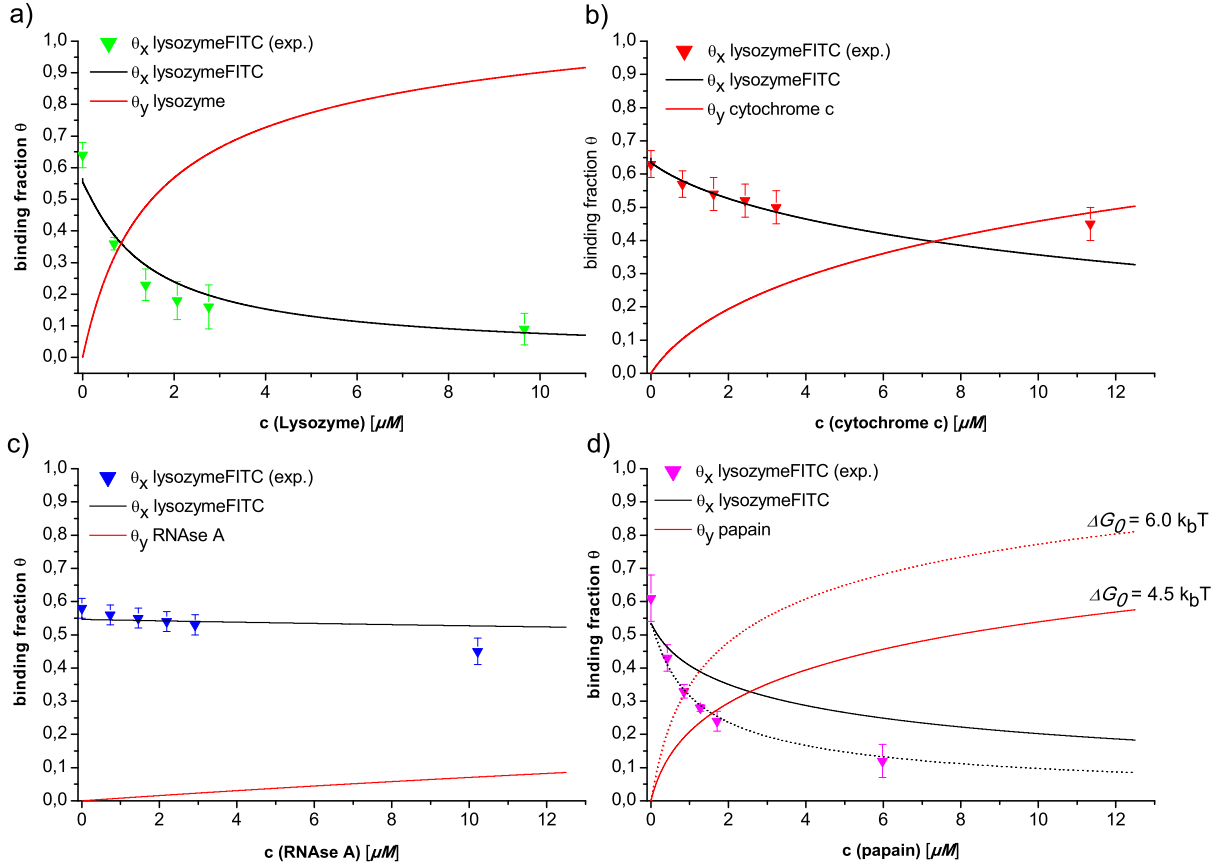


Figure 4.8: Competitive protein adsorption measured with fluorescence spectroscopy of (a) lysozyme<sup>FITC</sup> vs lysozyme, (b) lysozyme<sup>FITC</sup> vs cytochrome c, (c) lysozyme<sup>FITC</sup> vs RNase A, and (d) lysozyme<sup>FITC</sup> vs papain. Solid and dotted lines predict the competitive adsorption based on the cooperative binding model (equation 3.30).

loaded previously with lysozyme<sup>FITC</sup> was investigated (see Figure 4.8 a). In this case,  $N_{max} = N_1 = N_2$  and there is no change of the gel volume. Thus, this experiment presents a sensitive check of whether equilibrium is reached or not. Figure 4.8 a shows that the lysozyme-lysozyme exchange exhibits the expected intersection point at nearly half the initial binding fraction at  $\Theta_1 = \Theta_2 = 0.38$ . This unequivocally shows that protein adsorption to charged microgels is an equilibrium process which can be treated within the cooperative binding model.

For the other proteins, the fraction of liberated lysozyme is monitored and compared to the calculated value. In this case changes in the volume  $V_g$  are considered using the interpolation as defined in equation 3.47. Figure 4.8 shows that the predictions by theory are quantitative, and in the case of cytochrome c and RNase A within the limits of error. For papain, the theory is not fully quantitative but gets the correct trend. The comparison of these data with the parameters gathered in Table 4.5 now gives quantitative insight into the process of competitive adsorption: RNase A which has the lowest binding constant replaces the bound lysozyme<sup>FITC</sup> (Figure 4.8 c) less strongly than cytochrome c (Figure 4.8 b). In the case of papain having a similar binding constant as lysozyme, the replacement is strong (Figure 4.8 d). Here the prediction with  $\Delta G_0 = 4.5 k_B T$  as obtained from the ITC single adsorption isotherm does not work fully quantitatively, but full agreement can be reached by adjusting  $\Delta G_0 = 6.0 k_B T$ . The reasons for

this discrepancy are not yet fully understood but could be traced back to a strong mutual attraction of the bound proteins within the network not treatable by the present model.

To conclude, the Cooperative Binding Model showed a good performance in the prediction of the competitive adsorption from binary mixtures. The proteins lysozyme, cytochrome c, papain and RNase A were chosen because of their robust and characterized structures and their availability. In contrast to the Langmuir model the CB-model is very general and can be used for all globular proteins, providing their radii and charges can be determined and if  $\Delta G_0$  is available from an ITC experiment.

### 4.3 Cytochrome c Adsorption as measured by Anomalous Small Angle X-ray Scattering (ASAXS)

Small-angle X-ray scattering (SAXS) is a suitable method to investigate the spatial distribution of the proteins within polymer coated nanoparticles and can be used as an additional method to quantify the amount of adsorbed protein. In this work the adsorption of cytochrome c was measured by anomalous X-Ray small angle scattering in the vicinity of the adsorption edge of  $\text{Fe}^{3+}$ . The resonant scattering contribution to the overall scattering intensity allows to extract the formfactor and locate the distribution of the cytochrome c within the shell of microgel OM5UF. Moreover, the intensity of the resonant scattering part can be correlated with the concentration of  $\text{Fe}^{3+}$  ions and ultimately with the number of bound proteins per colloid. Cytochrome c is a small globular protein of  $\approx 12.300$  Da molecular weight and contains a porphyrin macrocycle with an iron atom, a complex called heme group. The heme group of cytochrome c can exist in an oxidized and reduced state. Figure 4.9 a shows the 3D structure of the protein with the porphyrin macrocycle containing the iron highlighted in the middle. The iron atoms in cytochrome c

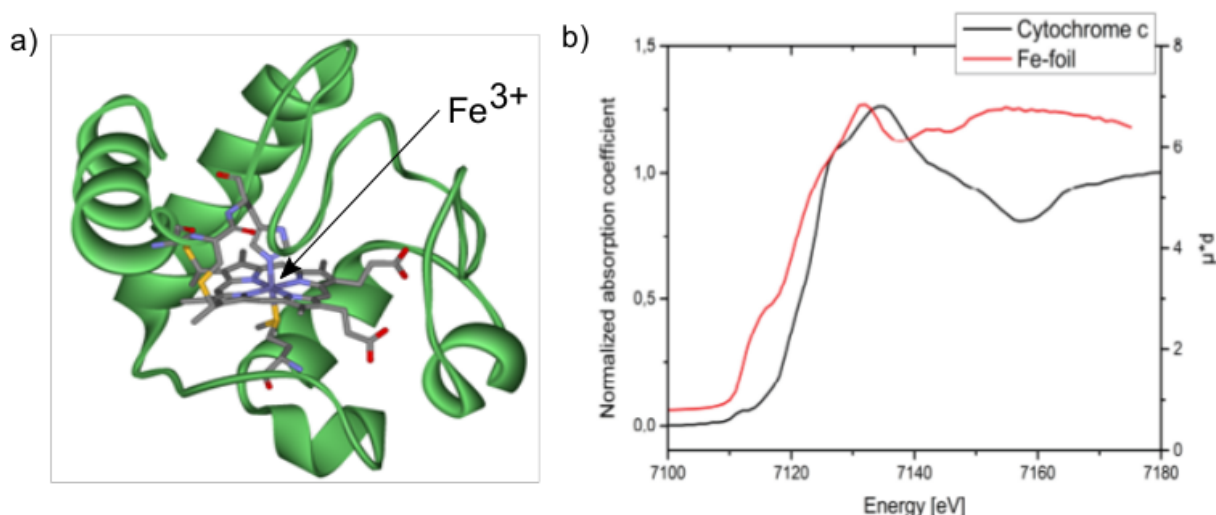


Figure 4.9: a) Crystal structure of cytochrome c shown here from PDB entry 3cyt. b) Comparison of the normalized adsorption spectrum of an iron foil and for cytochrome c.<sup>148</sup> See further explanation in the text.

is ionic and can exist as  $\text{Fe}^{3+}$  or  $\text{Fe}^{2+}$  referring to the oxidized and reduced state, respectively. In the ASAXS experiments there was no reducing species present and cytochrome c is in its oxidized state. Because of the overall low concentration of  $\text{Fe}^{3+}$  in the protein the ASAXS instrument is not sensitive enough to measure the adsorption spectrum and adsorption data were taken from literature.<sup>148</sup>

Figure 4.9 b shows the absorption spectrum of an iron foil (right axis) compared with the normalized absorption spectrum of the ionic iron in cytochrome C (left axis).<sup>148</sup> The K-absorption edge of the ionic iron in the protein complex is shifted (chemical shift) by nearly +10 eV when compared to the absorption edge of metallic Fe located at 7112 eV.

In anomalous X-ray scattering the scattering factor of an ion becomes a complex function of the energy

$E$  of the incoming radiation near the absorption edge

$$(4.3) \quad f_{ion} = f_0 + f'(E) + if''(E)$$

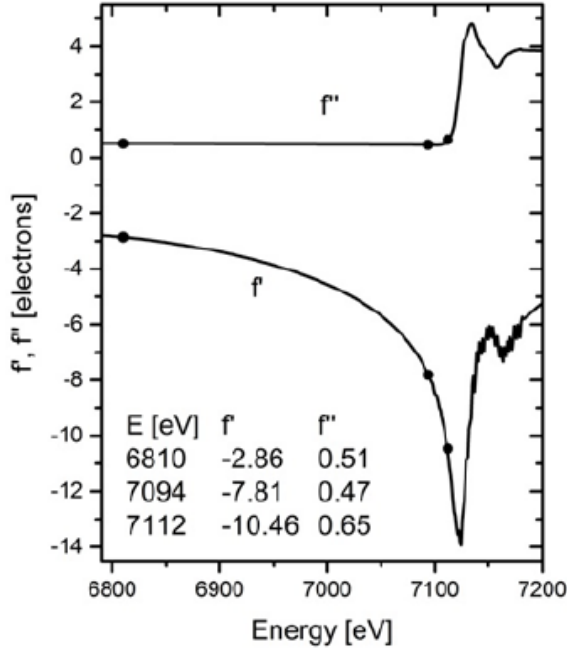


Figure 4.10: Anomalous dispersion corrections of  $\text{Fe}^{3+}$  based on the calculations of Cromer and Liberman.

Figure 4.10. The black dots represent the X-ray energies where the ASAXS measurements were performed. The Table in Figure 4.10 provides the anomalous dispersion corrections  $f'$  and  $f''$  for  $\text{Fe}^{3+}$  at the three energies  $E_1 = 6810$  eV,  $E_2 = 7094$  eV and  $E_3 = 7112$  eV. In Figure 4.11 the three the scattering curves are plotted against the scattering vector  $q$ . All scattering curves have been calibrated into absolute units; i.e. macroscopic scattering cross-sections in units of cross-section per unit volume  $[\text{cm}^2/\text{cm}^3] = [\text{cm}^{-1}]$ . The error bars for the scattering data are smaller than the line width and are not shown in Figure 4.11. The scattering curves show a systematic increase in intensity - as indicated by the arrow in Figure 4.11 a - when approaching the K-absorption edge at 7120 eV, thereby indicating a negative contrast of the microgel.

Calculating the scattering intensity  $I(\vec{q}) = |A(\vec{q})|^2 = A(\vec{q}) \cdot A^*(\vec{q})$  and averaging over all orientations of the colloid yields a sum of three contributions as described in detail in section 3.2.4.2. The calculated values for the dispersion corrections were used to separate the form factor of the pure-resonant scattering contribution of the Fe ions from the following equation which was already derived in section 3.2.4.2 (equation 3.27). Figure 4.11 b shows the total scattering and the pure resonant term as extracted with equation 3.27. The scattering cross section of the pure resonant term is about 3 order of magnitude smaller when compared to the overall scattering cross section. The distribution of the protein was derived from the fit of the pure resonant scattering cross section. In particular, the curve was fitted in the range

The first term  $f_0$  corresponds to the 26 electrons of Fe, while  $f'(E)$   $f''(E)$  represent the anomalous dispersion corrections of the iron ion. The values for  $f'(E)$  have been calculated in the energy range between 6000 and 7400 eV via Kramers-Kronig relation:<sup>149,150</sup>

$$(4.4) \quad f'(\omega) = \frac{2}{\pi} \mathcal{P} \int_0^\infty \frac{\omega' f''(\omega')}{\omega'^2 - \omega^2} d\omega'$$

with  $\mathcal{P}$  being the principal value of the integral and the frequency  $\omega$ . The values for  $f''(E)$  were obtained from the normalized absorption spectrum for cytochrome c as depicted in Figure 4.9 b. In a second step the values obtained from the principal value integral have been adjusted to results of Cromer-Liberman calculations in the limit of energies far apart from the K-absorption edge. The results for the anomalous dispersion corrections of  $f'(E)$  and  $f''(E)$  for  $\text{Fe}^{3+}$  are depicted in

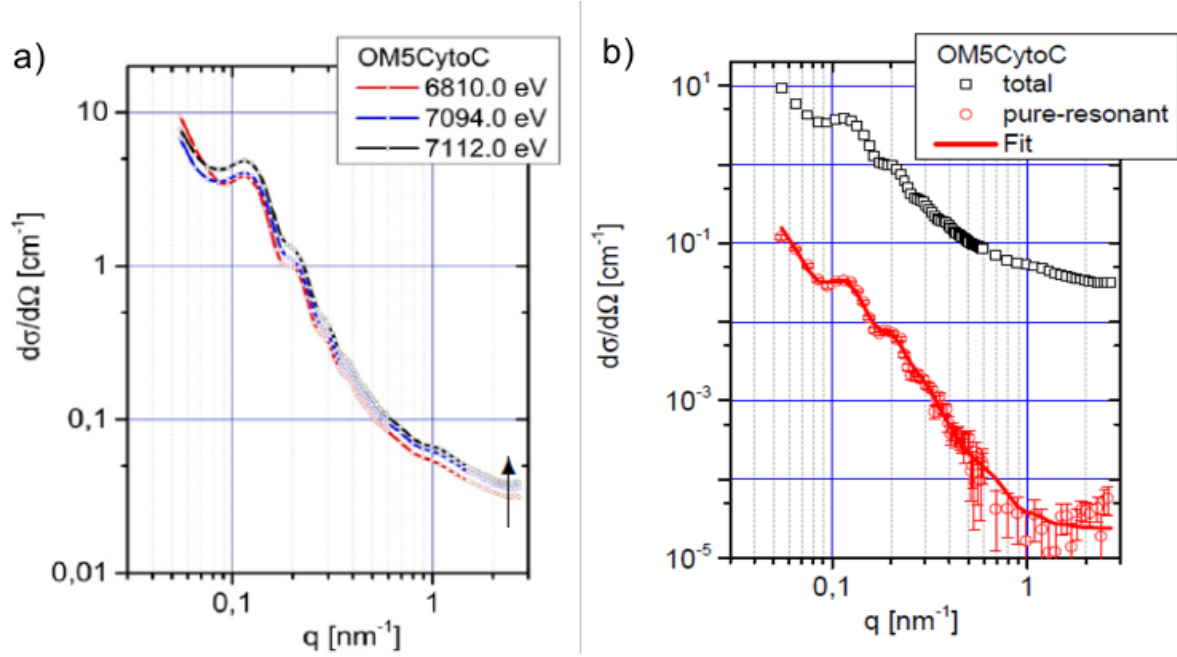


Figure 4.11: a) SAXS curves of microgel OM5UF loaded with cytochrome c measured at three different energies in the vicinity of the K-adsorption edge of  $\text{Fe}^{3+}$  at 7120 eV. b) Total scattering (black squares) and pure resonant scattering (red circles) contribution of the iron ion. The red line corresponds to the fit.

of  $0.1 \text{ nm}^{-1}$  to  $3 \text{ nm}^{-1}$  with the form factor of a spherical shell:

$$(4.5) \quad S_{\text{Fe}^{3+}}(q, R, D) = (K(q, R + D) - K(q, R))^2 + S_{bg}$$

with

$$(4.6) \quad K(q, R) = \frac{4}{3}\pi R^3 \frac{\sin(qR) - qR \cos(qR)}{(qR)^3}$$

Here  $R$  is the radius of the core,  $D$  denotes the thickness of the shell and  $S_{bg}$  the isotropic background scattering probably caused by non-adsorbed isolated proteins in the solvent. The fitting revealed an overall size of the particle  $R + D = 43 \text{ nm}$  with  $R = 30 \text{ nm}$ . Hence, the proteins distribute within a 13 nm thick part of the shell located close to the polystyrene core.

Figure 4.12 shows a sketch of the distribution and the concentration profile of cytochrome c in the shell of the uncharged microgel OM5UF. This thickness corresponds to approximately 4 layers of protein when a diameter of  $\sigma = 3.4 \text{ nm}$  is assumed for one cytochrome c. It can be concluded that most of the protein molecules are firmly bound to the inner layers of the spherical microgel, while the outer layers remain unoccupied. A similar observation was also made by Henzler et al. for the adsorption of  $\beta$ -lactoglobulin on spherical polyelectrolyte brushes.<sup>128</sup> The radius of the core is in good agreement with the hydrodynamic radius of the core  $R_{core} = 34 \text{ nm}$ . However,  $R + D$  as seen by SAXS shows significant deviations to the hydrodynamic radius as measured for the absolute dimensions of the microgel  $R_h \approx 85 \text{ nm}$ . The concentration of the adsorbed protein can be calculated from the number of Fe ions localized in the shell of the microgel. The number density can be derived from the resonant invariant of the Fe ions

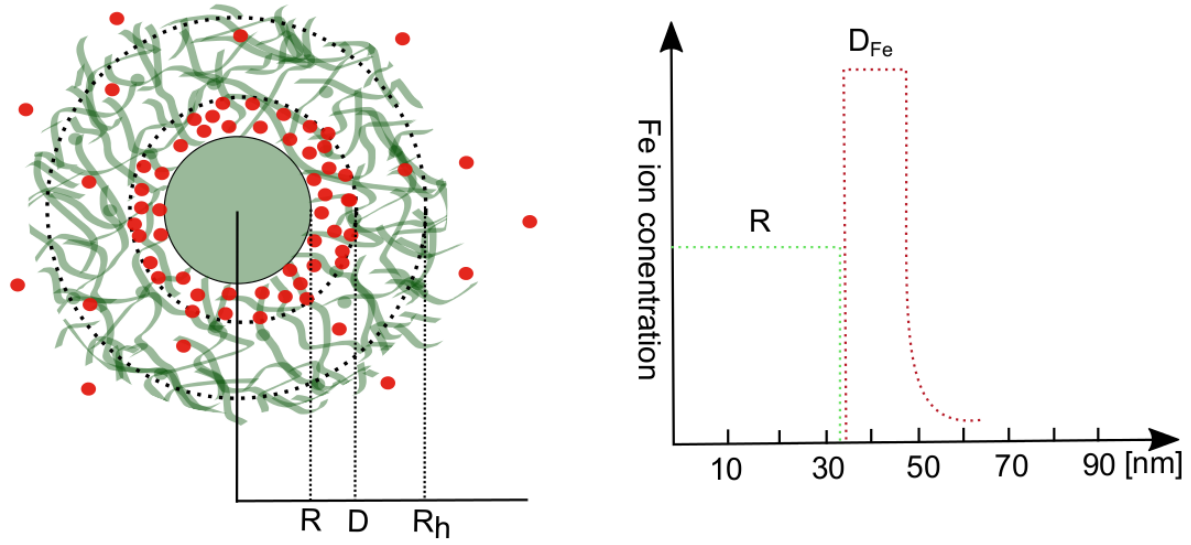


Figure 4.12: Sketch of the 2D microgel with the distribution of cytochrome c (left panel) and concentration profile of the protein (right panel). See further explanation in the text.

$Q_{Fe}$  as described in equation 3.29.  $Q_{Fe}$  is related to the number density of inhomogeneously distributed Fe-ions through the following relation

$$(4.7) \quad \bar{v}_{Fe} = \frac{1}{2V_{Fe}} \pm \sqrt{\frac{1}{4V_{Fe}^2} - \frac{1}{(2\pi)^3 r_0^2} \int_Q |A_{Fe}(q)|^2 d^3 q}$$

From this relation an amount of  $4.5 \times 10^{16} \text{ cm}^{-3}$  Fe-ions and therefore cytochrome c was calculated to be adsorbed onto the microgels. This corresponds to an amount of approximately 1000 protein molecules per microgel. This number is in very good agreement with the number of binding sites as obtained from ITC experiments (see Table 4.3).

## 4.4 Adsorption of Lysozyme as measured by AFM

In the following section the results of the AFM measurements are summarized. The AFM was operated in the tapping mode. The microgel OM6UF was immobilized on a silicon surface by submerging the wafer in a diluted microgel solution and evaporating the liquid film. Figure 4.13 a and b shows the height or topography profile of microgel OM6UF and OM6UF loaded with lysozyme respectively. Obviously, the topography image is neither able to resolve the core-shell structure nor to discriminate the size differences which are induced by protein adsorption. By comparing these values of approximately 250 nm with DLS data, one can conclude that the dried microgels on surfaces are strongly collapsed. In case of the unloaded

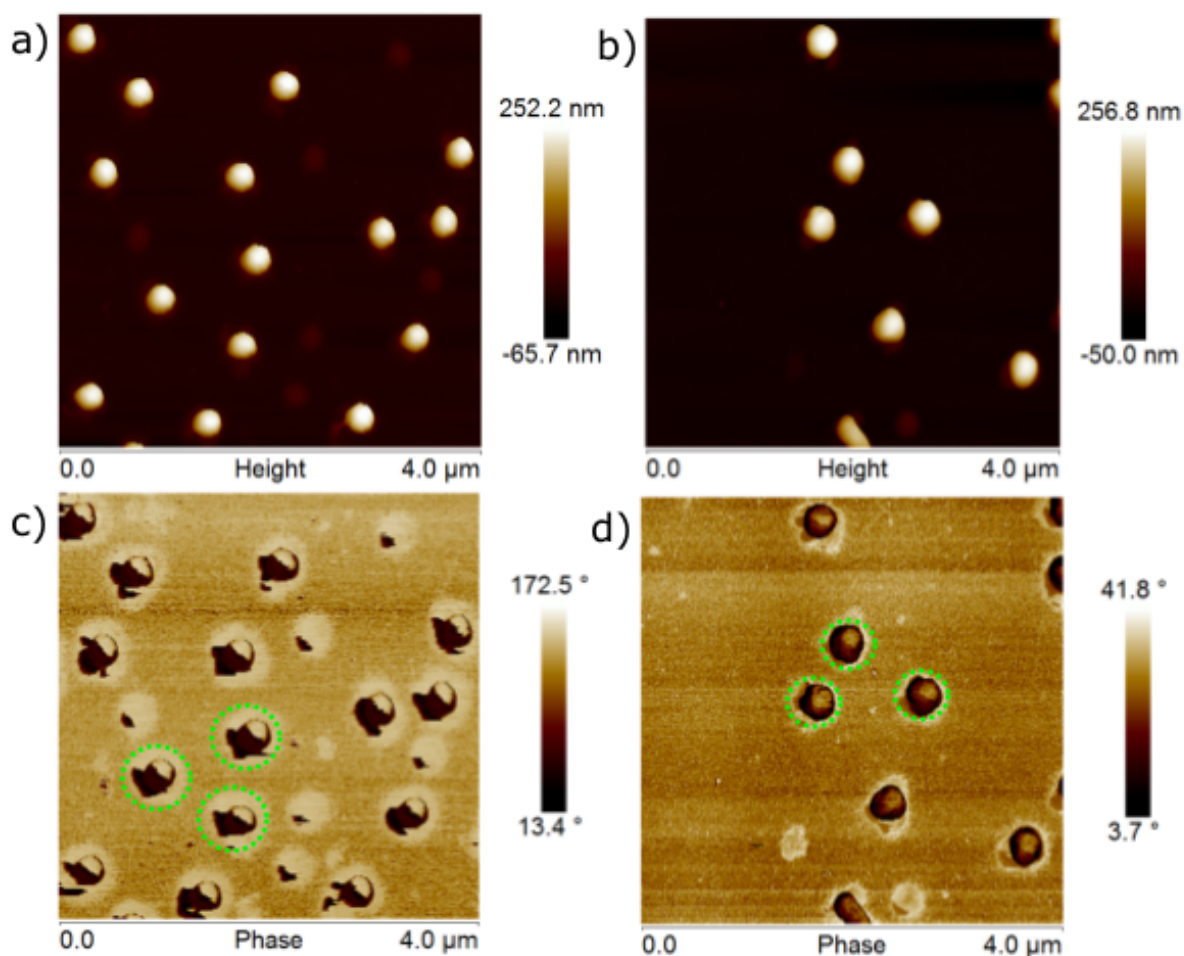


Figure 4.13: AFM images of a) 0.005% OM6UF microgel dried on a silicon wafer and b) 0.005% OM6UF microgel loaded with 0.025 mg/ml lysozyme (molar ratio  $x = 200.000$ ) dried on a silicon wafer; c) and d) corresponding phase of a) and b), respectively. The green circles indicate the lateral extension of the microgel.

OM6UF (Figure 4.13 a) the array can be best described as periodic loosely packed microgel array, which is in good agreement with the results on uncharged poly(NIPAM) microgels published by Horecha et al.<sup>151</sup> In contrast, the protein loaded OM6UF (Figure 4.13 b) seems to assemble in a less ordered array probably caused by a change in repulsive forces. In Figure 4.13 c and d the AFM phase is shown. Imaging the phase in AFM is a powerful tool that is sensitive to surface stiffness/softness and adhesion



between the tip and surface. It allows chemical mapping of surfaces based on these material differences. For both microgels the protein free and the protein loaded a strong phase contrast between the shell, the core and surrounding substrate is observed. There is also a significant phase contrast between the loaded and unloaded shell indicating a strong change in the stiffness/softness. It was already concluded from DLS data that the shell of the microgel shrinks upon protein adsorption leading to a more compact and stiffer structure. However, these measurements were done in air and a qualitative interpretation of these data remains ambiguous.

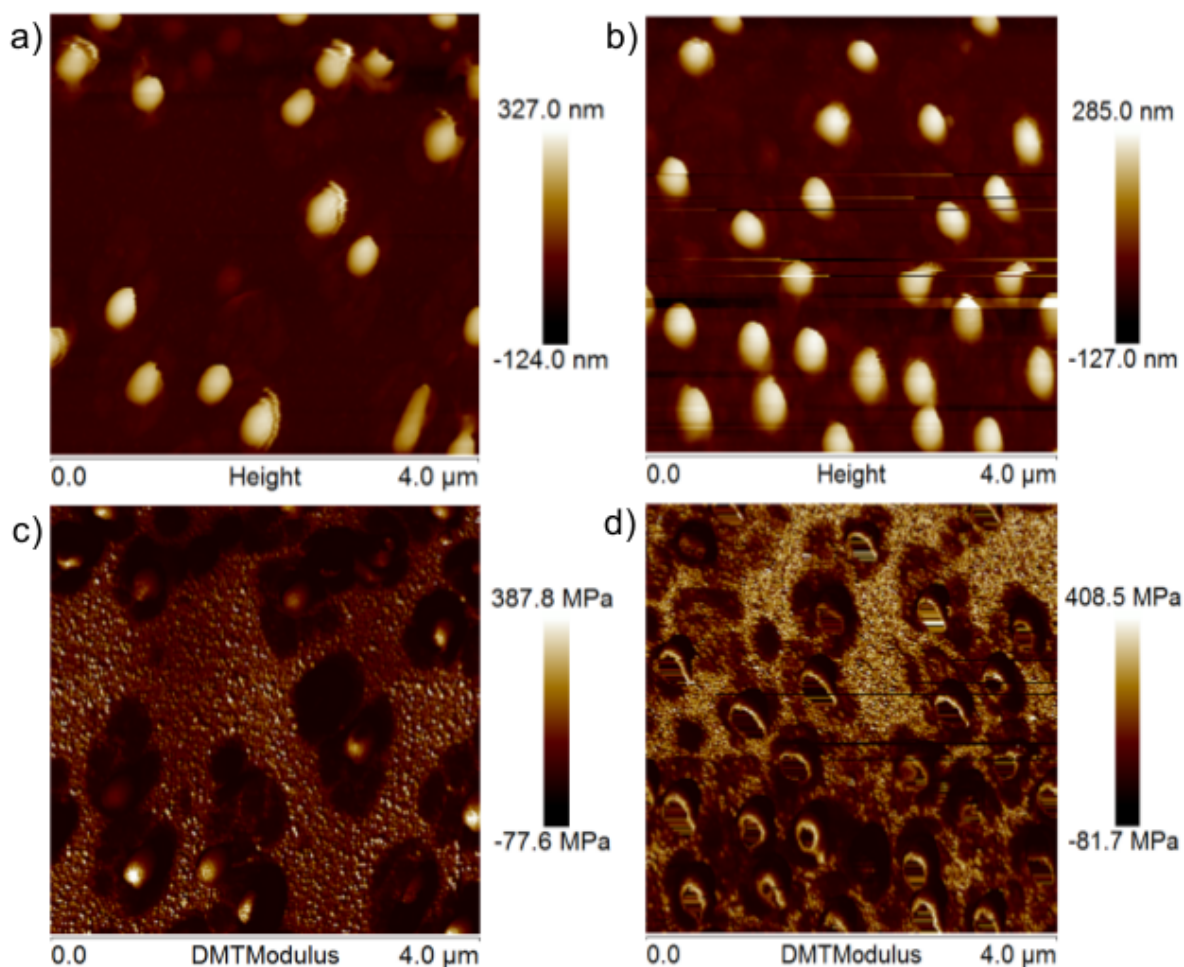


Figure 4.14: AFM images of a) 0.005% OM6UF microgel in 10 mM MOPS at pH = 7.2 immobilized on a poly-lysine coated silicon wafer and b) 0.005% OM6UF microgel loaded with 0.025 mg/ml lysozyme (molar ratio  $x = 200.000$ ) in 10 mM MOPS at pH = 7.2 immobilized on a poly-lysine coated silicon wafer; c) and d) corresponding elastic modulus (DMT).

Hence, AFM measurements in liquid were performed and the samples were rinsed in situ in the AFM fluid sample holder. The microgels will not immobilize on the surface by evaporation and were attached by electrostatic interactions. For this reason the silicon wafer was functionalized with APTES and Poly-L-Lysine (PLL). PLL is a polyelectrolyte and at pH = 7.2 is highly positively charged. It was found that PLL leads to a more firmly attachment of the negatively charged microgels. Figure 4.14 a and b shows the topography images of pure OM6UF and the protein loaded OM6UF, respectively. The



instrument was operated in the PeakForce Tapping Mode® (Bruker). This mode maps and distinguishes between nanomechanical properties - including modulus, adhesion, dissipation, and deformation while simultaneously imaging sample topography. In contrast, to the topography in air the data in liquid are more noisy indicating that the particles have a strong drift on the surface. The analysis of the sample topography reveals a decrease in size from 330 nm to 285 nm. Generally, the attachment of the microgels on the surface seems not to influence their shrinkage behaviour upon protein adsorption.

DLS data showed a decrease of the hydrodynamic radius  $R_h$  from 275 nm to 240 nm upon saturation with lysozyme (see section 4.1.1). DLS analysis generally gives an ensemble averaged value of  $R_h$  from the free particles in solution. In contrast, the height as determined by AFM is evaluated from one microgel particle or at least from a set of microgel particles attached to a surface. Consequently, the differences in the absolute size result from the attachment of the microgel to the surface. The interaction between the poly(NIPAM) shell and the substrate gives rise to a partial collapse upon adsorption as depicted in Figure 4.15

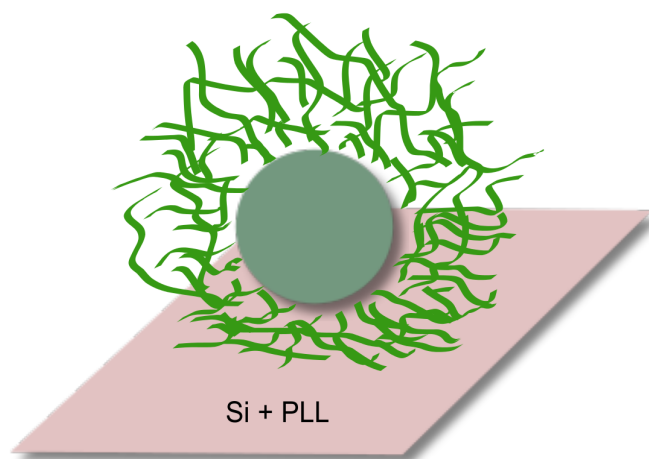


Figure 4.15: Scheme of a core-shell microgel attached to a PLL modified silicon surface. The attraction of the microgel leads to a partial collapse of the outer chains.

To conclude, AFM images in air revealed a strongly collapsed structure of the core-shell microgels on the silicon surface. The adsorption of the lysozyme onto the shell of the microgel changes the phase of the AFM image indicating a change in the mechanical properties. However, a quantitative assignment of these changes was not possible. For liquid AFM measurement it was shown that the microgels can be attached via electrostatic interactions with a functionalized silicon surface. Upon protein adsorption the shell of the surface attached microgels also began to shrink, but to a lesser extent as compared to the microgels in free solution.

## 5 Summary and Outlook

The focus of this thesis was a detailed investigation of protein adsorption onto weakly charged or uncharged core-shell microgels consisting of a solid polystyrene core and a poly(NIPAM) shell. The dimensions of the microgels were ranging between 100 and 300 nm.

First, adsorption isotherms of the proteins papain, lysozyme, Rnase A, cytochrome c and glucosidase were obtained by ITC. The use of ITC to characterize protein nanoparticle interactions was discussed critically. It was demonstrated that the stability of the protein plays a crucial role for these type of measurements. On the example of glucosidase it was shown that larger size proteins occurring as dimers and oligomers can cause problems in the interpretation of the adsorption isotherms. Furthermore, the residual enthalpy  $\Delta H_{res}$  was identified to explain the differences between the enthalpies  $\Delta H_{ITC}$  and the Van't Hoff enthalpy  $\Delta H_b$ . This residual enthalpy originates from protonation effect or conformational rearrangements of the protein during adsorption. More concretely, the binding enthalpy  $\Delta H_b$  of cytochrome c to a non-charged core-shell microgel was identified as endothermic, but was accompanied by strong exothermic reaction during the adsorption process which indicates a conformational rearrangement or protonation step.

In all these cases the protein adsorption isotherms were first fitted using the Langmuir model to reveal the thermodynamic parameters  $K$ ,  $N$  and  $\Delta H$ . However, it was shown that the Langmuir model is limited to these three parameter and the analysis is not fully quantitative, although the right trends can be derived. Thus, in a second step, the adsorption isotherms were analyzed with the CB-model. With the approach it was possible to separate the contributions of electrostatic and non-electrostatic interactions to the total binding energy and to discuss the binding isotherms on a more quantitative level. The binding model is virtually free of fit parameters and is easily expandable to protein mixtures adsorbing on polymeric surfaces. The only fit parameter is the intrinsic binding energy  $\Delta G_0$  which can be obtained by fitting the adsorption isotherm of the single type of protein. Using the CB-model it was possible to show that the stronger binding of lysozyme compared to cytochrome c results from the higher intrinsic binding energy of lysozyme.

In addition, the CB-model was able to predict the competitive adsorption from binary mixtures of a labeled lysozyme - lysozyme<sup>FITC</sup> and the proteins papain, lysozyme, Rnase A and cytochrome c. In the mixture lysozyme and lysozyme<sup>FITC</sup> it could be demonstrated that protein adsorption onto this type of core-shell microgels is a reversible process. The predictive power of the cooperative binding model contributes to important research areas in nano(bio)technology in which protein adsorptions play a pivotal role.

Secondly, in this work the spatial distribution of cytochrome c in a core-shell microgel was elucidated

by anomalous X-Ray scattering. By measuring at three different energies close to the K-edge of the iron ion it was possible to unveil the pure resonant scattering contribution. The scattering data revealed a core-shell structure where the proteins are located within a 13 nm thick shell close to the core. Moreover, by analyzing the invariant it was possible to quantify the amount of adsorbed protein. It was demonstrated that this amount is in good agreement with the number of binding sites as obtained from ITC.

The third part of this thesis was devoted to the interaction of core-shell microgels with charged surfaces. It could be shown that the microgels form a periodic loosely packed 2D array. Protein adsorption seems to change this order probably due to a change in repulsive forces between the particles. By analyzing the phase of the AFM signal it was possible to visualize the core-shell structure. Adsorption of lysozyme leads to a significant phase contrast indicating a change in the stiffness of the microgel. For the measurements in liquid the microgels were attached by electrostatic attractions with the poly-L-Lysine layer. The height image revealed a structure in which the microgels are partially collapsed along the contact area with the surface.

## 6 Materials and Methods

### 6.1 Materials

The initiator potassium peroxydisulfate (KPS), the monomers styrene, N-isopropylacrylamide (NIPAM), acrylic acid, N,N-methylenebisacrylamide (BIS) and sodium dodecyl sulfate (SDS) were purchased from Sigma Aldrich. Styrene is stabilized by tert-butyl catechol as an inhibitor to avoid an uncontrolled polymerization. Prior to the polymerization reaction with KPS the inhibitor was removed by flushing through a column filled with an inhibitor remover (Sigma Aldrich). Acrylic acid was distilled in a rotary evaporator under reduced pressure (1 mbar, 40-45 °C) in order to remove the hydroquinone stabilizer. The cleaned styrene and acrylic acid were stored at -4° C. All other chemicals for the synthesis of the core-shell microgel were used as received. The buffer was prepared using 10 mM 3-(N-morpholino) propane sulfonic acid (MOPS) (Sigma Aldrich) and 2 mM sodium azide (NaN<sub>3</sub>)(Sigma Aldrich) to avoid bacterial contamination. The pH was adjusted to 7.2 by dropwise addition of 1 M NaOH under stirring. The ionic strength was adjusted by adding sodium chloride (NaCl). For the protein labeling experiments fluorescein isothiocyanate (FITC) was bought from Serva. For the surface functionalizations Poly-L-Lysine hydrobromide was purchased from Sigma Aldrich (LOT # SLBM7099V) and used as received. 3-Aminopropyltriethoxysilane (APTES) was ordered from Gelest, PA, USA (Lot # 31-21874) and used as received. Silicon wafers 100 orientation were purchased from Virginia Semiconductors, VA, USA.

### 6.2 Proteins

Lysozyme from *chicken hen egg white*, papain from *carica papaya*, cytochrome c from *bovine heart*, RNase A from *bovine pancreas*, and  $\beta$ -D-Glucosidase from *almonds* were purchased from Sigma and dialyzed against the buffer used in the experiment.

### 6.3 Synthesis and Characterization of Core-Shell Microgels

#### 6.3.1 Synthesis of the Polystyrene Cores

The synthesis of the polystyrene cores were carried out using a 2 L three-necked flask equipped with stirrer, reflux condenser, and thermometer. In the first step styrene, NIPAM and the surfactant SDS were dissolved in water and the mixture was stirred at 300 rpm. Subsequently, the mixture was degassed for 10 minutes with nitrogen and heated up to 80 °C. The reaction was started by injection of the radical initiator KPS. The reaction was allowed to continue for 8 h under nitrogen atmosphere at 80 °C. Afterwards,

the viscous white suspension was cooled down to room temperature and filtered through glass wool afterwards to remove possible aggregates. Table 6.1 shows the amount of educts and solvent used for

Table 6.1: Overview of the amount of educts used for the synthesis of the polystyrene cores.

	PS1	PS2	PS3
m (styrene) [g]	200	30	30
m (NIPAM) [g]	10	1.5	1.63
m (SDS) [g]	1.83	0.45	0.1
m (KPS) [g]	0.392 (in 10 g H <sub>2</sub> O)	0.172 (in 5 g H <sub>2</sub> O)	0.3 (in 20 g H <sub>2</sub> O)
m (H <sub>2</sub> O)[g]	700	130	270
weight percentage (in % w/w)	14.7	10.46	5.96
Hydrodynamic radius $R_{core}$ [nm]	62.2±0.7	34 ±5	100 ±7

the synthesis of different polystyrene cores PS1, PS2 and PS3. The size of the cores was controlled by changing the amount of surfactant. The core particles were purified by ultrafiltration against water for approximately two weeks using a cellulose nitrate membrane (Schleicher and Schuell and Millipore) with pore size of 50 nm. Using this technique, unreacted monomers, surfactant molecules and extra ions can be removed from the particle dispersion. The purification process was monitored by measuring the conductivity of the extruded serum until a conductivity similar as ultrapure water is reached ( $\kappa < 0.7 \mu S/cm$ ). Afterwards, the PS particles were removed and their weight percentage was determined (see Table 6.1). The size of the PS particles was measured by dynamic light scattering using a Zetasizer (see section 6.3.5). The hydrodynamic radii for the PS cores listed in Table 6.1 under  $R_{core}$ .

### 6.3.2 Synthesis of the Shell

The seeded emulsion polymerisation of the core-shell microgels were done in a 2 L three-necked flask equipped with a stirrer, reflux condenser and thermometer. The amounts of the educts used for the synthesis of these particles are summarized in Table 6.2. The microgel NW15 has been synthesized in a previous work.<sup>81</sup> The seed latex, NIPAM, the cross-linker BIS, and water were added to the flask and degassed by flushing with nitrogen. The mixture was heated to 80 °C under nitrogen atmosphere while

Table 6.2: Overview of the amount of educts used for the synthesis of the core-shell microgels.

	NW15	OM5UF	OM6UF
m (PS-core) [g]	131.2 of 14.73 wt-% PS1	47.8 of 10.46 wt-% PS2	167.7 of 5.96 wt-% PS3
m (H <sub>2</sub> O) [g]	592	175	90
m (KPS) [g]	0.504 (in 20.3 g H <sub>2</sub> O)	0.182 (in 10 g H <sub>2</sub> O)	0.226 (in 20 g H <sub>2</sub> O)
m (NIPAM) [g]	23.8	3.8	10
m (BIS) [g]	1.62	0.28	0.68
m (AAc) [g]	0.64	0.24 (in 10 g H <sub>2</sub> O)	0.64 (in 20 g H <sub>2</sub> O)

stirring at 200 rpm. Subsequently, acrylic acid was added via a syringe. In the last step the initiator was added and the reaction was allowed to proceed for 5 h at the given temperature. Then the mixture was

cooled down to room temperature and filtered through glass wool. The microgels were purified in the same way as the seed latex with ultrafiltration using a cellulose nitrate membrane with a pore size of 100 nm. The serum was replaced against millipore water for about 4 weeks until a conductivity of ( $\kappa < 1 \mu \text{ S/cm}$ ) was reached. Afterwards, their weight percentage was determined and the molecular weight of the microgels was calculated using following formula:

$$(6.1) \quad M_{w, \text{microgel}} = (m_{\text{core}} + m_{\text{shell}})N_A = \frac{\rho_{\text{core}} \frac{4}{3} \pi R_{h, \text{core}}^3}{w_{\text{core}}} N_A$$

Here  $\rho_{\text{core}} = 1.055 \cdot 10^{-21} \text{ g/nm}^{-3}$  denotes the density of the PS core and  $R_{h, \text{core}}$  denotes the hydrodynamic radius of the PS core. The weight fraction  $w_{\text{core}} = w_{\text{core}}/w_{\text{core-shell}}$  can be calculated from the weight percentage of the purified PS core and core-shell particles. In Table 6.3 the properties of the three microgels NW15, OM5UF and OM6UF are summarized.

Table 6.3: Composition, size and molecular weight of the shell network of the microgels used for the protein adsorption studies.

microgel	NIPAM [mol-%]	BIS [mol-%]	AAC [mol-%]	$w_{\text{core}}$	$M_w$ [g/mol]	$R_h^a$ [nm]
NW15	85	5	10	0.54	$1.18 \cdot 10^9$	$185 \pm 50.2$
OM5UF	85	5	10	0.86	$1.21 \cdot 10^8$	$75 \pm 5$
OM6UF	85	5	10	0.58	$5.79 \cdot 10^9$	$284 \pm 7$

$R_h$  = Hydrodynamic radius as measured in millipore water after extensive ultrafiltration

### 6.3.3 Transmission Electron Microscopy (TEM)

TEM samples were prepared by putting approximately  $5 \mu\text{L}$  of a 0.0025 wt% solution on a TEM copper grid with carbon support film (200 mesh, Science Services, Munich, Germany). The carbon coated copper grids have been pretreated by 10 seconds of glow discharge. The excess of liquid was blotted with a filter paper after 2 minutes. The remaining liquid film on the TEM grid was dried at room temperature for at least one hour. The specimen was inserted into sample holder (EM21010, JEOL GmbH, Eching, Germany) and transferred to a JEOL JEM-2100 with a LaB6 cathode (JEOL GmbH, Eching, Germany). The TEM was operated at an acceleration voltage of 200 kV. All images were recorded digitally by a bottom-mounted 4k x 4k CMOS camera system (TemCam-F416, TVIPS, Gauting, Germany) and processed with a digital imaging processing system (EM-Menu 4.0, TVIPS, Gauting, Germany). Figure 6.1 shows the TEM images from the microgels NW15, OM5UF and OM6UF. The TEM sample preparation requires drying of the microgels and the core-shell structure is not clearly visible due to this process. Instead, the NIPAM shell collapses into a compact structure around the core which leads to visible deviations from the spherical shape. The size of these particles is similar to the size of the PS-cores as determined by DLS data. Unfortunately, microgel OM5UF shows higher polydispersity and aggregation. This probably can be traced backed to the smaller size of the particles.

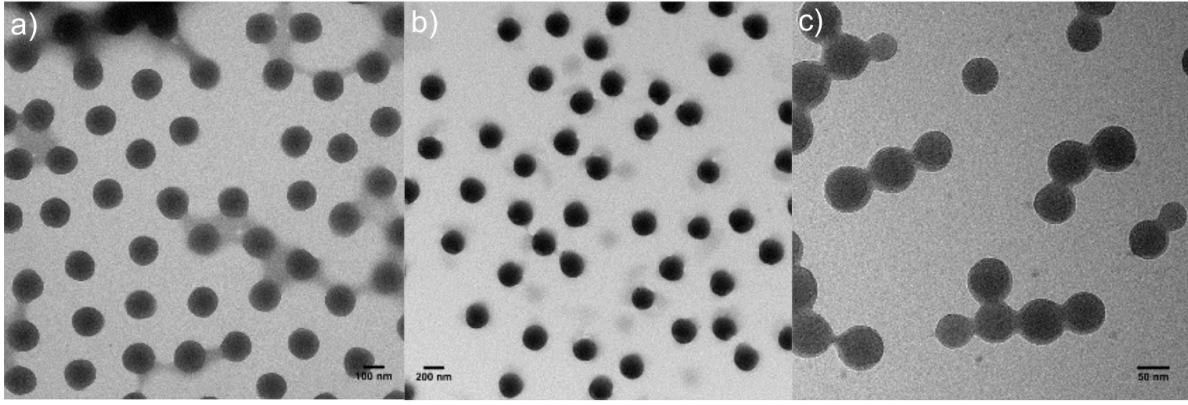


Figure 6.1: TEM images of core-shell microgels a) NW15, b) OM6UF and c) OM5UF. See further explanation in the text.

### 6.3.4 Conductometric and Potentiometric Titrations

Simultaneous conductometric and potentiometric measurements were performed using the 809 Titrand system (Metrohm Ion analysis, Herisau, Switzerland) equipped with an external dosing device (807 Dosing Unit, Metrohm Ion analysis), a stirrer (801 Stirrer, Metrohm Ion analysis), pH electrode (pH 0-14, Metrohm Ion analysis), and a conductivity module (856 Conductivity Module, Metrohm Ion analysis). The Titrand system was controlled by the tiamo 2.0 software (Metrohm Ion analysis). For the titration experiment, the microgel dispersion was diluted with water to a total concentration of 0.5%. Then, 20 mL of the microgel suspension were titrated with 0.01 M NaOH. The titrations were run in a thoroughly cleaned 50 mL beaker fitted with the pH and the conductivity electrode. The NaOH was added to the microgel suspension with a flow rate of 0.1 mL/min. This slow rate is necessary because of the longer relaxation time which is required to attain the equilibrium between the aqueous and the microgel phase. The potentiometric and conductometric titration curve of OM5UF and OM6UF are shown in Figure 6.2. From the equivalent point the titration curves the amount of acrylic acid polymerised into the microgel particles is determined. In addition, the dissociation degree  $\alpha_{diss}$  of the carboxylic acid functional groups can be calculated as a function of the amount of added NaOH and, thus, as a function of the pH according to

$$(6.2) \quad \alpha_{diss} = \frac{[V]_{pH}}{[V]_{eq}}$$

where  $[V]_{pH}$  and  $[V]_{eq}$  is the volume of added NaOH at a given pH value and at the equivalent point, respectively. To calculate the pKa value of the carboxylic acid functional groups as a function of the dissociation degree, the following equation is used:

$$(6.3) \quad pK_a = pH - \log\left(\frac{\alpha_{diss}}{1 - \alpha_{diss}}\right)$$

### 6.3.5 Dynamic Light Scattering (DLS)

Dynamic light scattering (DLS) experiments were performed at a single angle (173°) using a Zetasizer Nano ZS (Malvern Instruments). The instrument consists of a He-Ne-Laser at 633 nm wavelength and

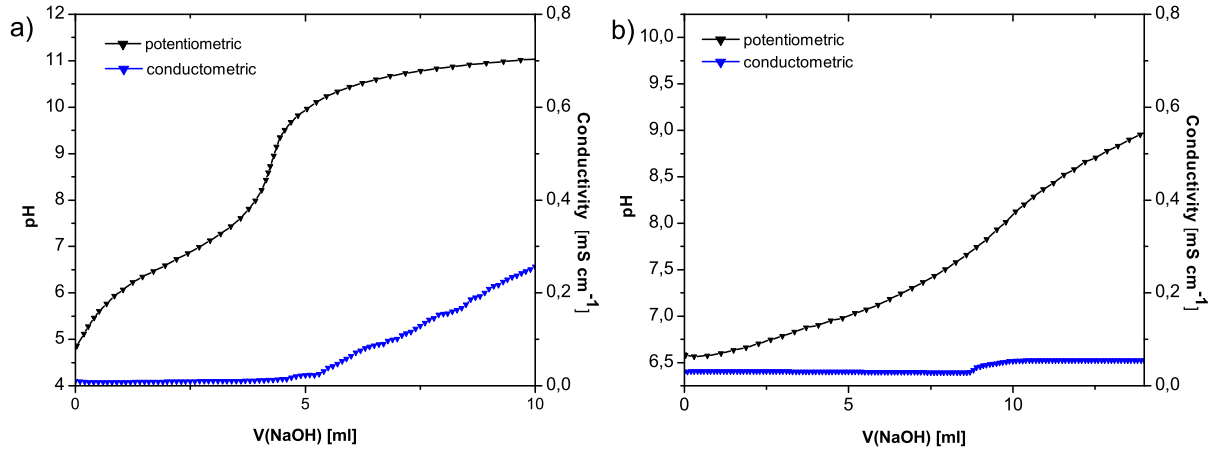


Figure 6.2: Potentiometric and conductometric titrations of a) OM6UF in millipore water and b) OM5UF in millipore water

can be used for the analysis of particles with diameters ranging from 0.3 nm and 10 nm according to the manufacturer's instructions. Prior to each measurement the microgel suspensions were diluted to a concentration of 0.01% w/w with MOPS buffer. In case of the protein loaded microgels stock solutions at different molar ratios were prepared and diluted to the same concentration. In case of the polystyrene cores the suspensions were diluted to a concentration of 0.01% w/w in millipore water. To prevent contamination with dust all samples were filtered through a 1.2  $\mu\text{m}$  polyethersulfone (PES) membrane. Before starting the measurements, the samples were incubated at the desired temperature for 5 min to attain thermal equilibration. Signals were correlated  $10 \times 10$  s.

The DLS data were analyzed with the software provided by the manufacturer to evaluate the hydrodynamic radius. Particle fluctuations in the dynamic light scattering experiment are described by a first-order auto-correlation function  $g^1(q, \tau)$ , where  $q$  is the wave vector and  $\tau$  is the decay time. For monodispersed particles  $g^1(q, \tau)$  is a single exponential decay:

$$(6.4) \quad g^1(q, \tau) = \exp(-\Gamma\tau)$$

with  $\Gamma$  being the decay rate. The decay rate is related to  $D_t$  via

$$(6.5) \quad \Gamma = D_t q^2$$

Finally, the analysis of the hydrodynamic radius  $R_h$  is derived from the translational diffusion coefficient  $D_t$  according to the Stokes-Einstein relation:

$$(6.6) \quad \langle D \rangle = \frac{k_B T}{6\pi\eta R_h}$$

## 6.4 Isothermal Titration Calorimetry

ITC experiments were performed using a VP-ITC instrument (MicroCal, GE Healthcare, Freiburg, Germany) equipped with a degassing unit. The instrument is controlled by the VPViewer software (MicroCal). The instrument consists of a sample cell and a reference cell composed of Hastelloy® Alloy C-276



which is a highly efficient thermal conductive material and is inert to many different solvents. The former one is usually filled with the nanoparticle suspension and the latter one is filled with ultrapure water. Before each titration the two cells need to be equilibrated in such a way that the temperature difference between the cells approaches zero and the applied reference power  $dP$  of the feedback system shows a stable baseline.

The sample preparation occurred as follows: Prior before each measurement samples have been degassed for 5 minutes at 1 K below the experimental temperature to avoid formation of air bubbles during the ITC experiment. Then a fixed volume of 1.4 mL of the microgel suspension was filled into the sample cell and a volume of 280  $\mu\text{L}$  buffer matched protein solution was soaked up in the syringe. For all measurements the reference power was set to 10  $\mu\text{cal/sec}$  and the stirring speed in the sample cell was 307 rpm. Then the protein solution was titrated successively into the sample cell and  $Q'$  was evaluated for each injection step. Afterward, the same protein solution was titrated into the pure buffer system to account for the heat of dilution. After each experiment the sample cell and the syringe were cleaned thoroughly using surfactant, 15 vol-% hydrogen peroxide, ultrapure water and acetone successively. Table 6.4 summarizes the experimental conditions. The injection program was adjusted to obtain good quality data near the inflection point of the isotherm. For all measurements listed in Table 6.4 the  $C$ -parameter was in a reliable range (see section 3.2.1).

Table 6.4: Overview of ITC parameters used in the experiments

System	Ionic strength [mM]	T [K]	c(protein) [mM]	c(microgel) [mM]	Injections
NW15 + lysozyme	7	298	0.695	$8.47 \cdot 10^{-7}$	20×3 $\mu\text{L}$ + 48×5 $\mu\text{L}$
NW15 + RNase	7	298	1.0204	$8.47 \cdot 10^{-7}$	40×2 $\mu\text{L}$ + 44×5 $\mu\text{L}$
NW15 + Glucosidase	7, 17, 32	298	0.088	$8.47 \cdot 10^{-7}$	20×3 $\mu\text{L}$ + 40×6 $\mu\text{L}$
NW15 + papain	7	298	0.523	$8.47 \cdot 10^{-7}$	69×4 $\mu\text{L}$
NW15 + cytochrome c	7, 17, 32	298	0.598	$8.47 \cdot 10^{-7}$	20×3 $\mu\text{L}$ + 48×5 $\mu\text{L}$
OM5UF + cytochrome c	7	293, 298, 303	0.598	$8.26 \cdot 10^{-6}$	20×3 $\mu\text{L}$ + 28×5 $\mu\text{L}$
OM6UF + lysozyme	7	298	0.695	$1.73 \cdot 10^{-7}$	75×4 $\mu\text{L}$

## 6.5 Fluorescence Spectroscopy

### 6.5.1 Labeling with Fluorescein isothiocyanate

Because the coupling of an amine group to the fluorophore is most efficient at basic conditions, a amount of 10 mg/ml Lysozyme (0.695 mM) is dissolved in 50 mM bicarbonate buffer at pH = 8.85. In the next step an equimolar amount of FITC was added from a freshly prepared stock solution of 5 mg/ml FITC

in anhydrous DMSO. The solution was diluted to aliquots of 1 mg/ml lysozyme using the bicarbonate buffer and shaken moderately for 1 h in an Eppendorf shaker. The protein was isolated via size exclusion chromatography using a Sephadex G25 column (GE healthcare) equilibrated with 10 mM MOPS and 2 mM  $\text{NaN}_3$  at pH 7.2. By this means, excess FITC is removed from the reaction mixture and the labeled protein is transferred in the desired buffer for further experiments. The collected fractions were analyzed by UV-vis. Fractions showing a higher extinction than  $E_{278} \geq 0.2$  were unified and the degree of labeling was calculated using following equation:

$$(6.7) \quad \frac{n(\text{FITC})}{n(\text{Protein})} = \frac{E_{495}}{\epsilon_{495, \text{FITC}} \cdot c_p}$$

with  $c_p = \frac{E_{278} - E_{495}CF}{\epsilon_{278, \text{Protein}}}$

Figure 6.3a shows the UV-vis spectrum of the purified Lysozyme<sup>FITC</sup>, where the signal at 278 nm is originating from aromatic aminoacids and the signal at 495 nm can be traced back solely to the excitation of the fluorescein moiety.  $E_{278}$  and  $E_{495}$  are the extinction values at both positions in the spectrum. The values  $\epsilon_{278, \text{protein}}$  and  $\epsilon_{495, \text{FITC}}$  are the molar extinction coefficients of the protein and the unbound FITC ( $37047$  and  $47106 \text{ M}^{-1} \text{ cm}^{-1}$ , respectively). CF is a correction factor  $CF = E_{278}/E_{495} = 0.43$ . All values have been measured in 10 mM MOPS at pH 7.2 at 298 K. The labeling degree of Lysozyme<sup>FITC</sup> was calculated to  $\approx 1$ , that means on average every protein molecule is assigned with exactly one fluorophore molecule.

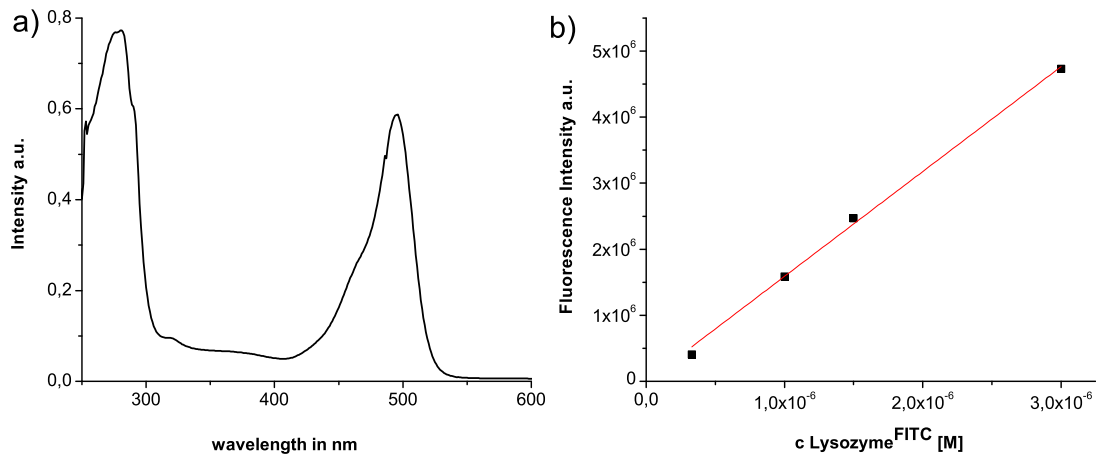


Figure 6.3: a) UV-vis spectrum of Lysozyme<sup>FITC</sup> in 10 mM MOPS buffer at 298 K. The peak at 278 nm results from the excitation of aromatic amino acids and the peak at 495 nm is the excitation wavelength  $\lambda_{ex}$  of the fluorescein moiety. b) Fluorescence emission intensity at  $\lambda_{em} = 518 \text{ nm}$  of Lysozyme<sup>FITC</sup> depending on the concentration of the protein. Spectra were recorded in 10 mM MOPS buffer at pH = 7.2 at 293 K at the excitation wavelength  $\lambda_{ex} = 495 \text{ nm}$ .

Figure 6.3 b shows the calibration line of lysozyme<sup>FITC</sup> in 10 mM MOPS at pH = 7.2 and 298K. The calibration is necessary to determine the amount of labelled protein adsorbed on the microgel.

### 6.5.1.1 Experimental Setup for a Binary Protein Mixture

Fluorescence spectra were recorded with a Fluoro-Max-3 spectrometer (JY-Horiba) at a slit width of 1.5 nm and an optical path length of 1 cm. In the first step the microgel was loaded to  $\approx 60\%$  with lysozyme<sup>FITC</sup>. For this purpose a solution of 0.8  $\mu\text{M}$  lysozyme<sup>FITC</sup> in 10 mM MOPS at pH = 7.2 was filled in an optical quartz cell and  $2.4 \times 10^5 \mu\text{M}$  of buffer-matched microgel suspension was added under moderate stirring. At the same time the fluorescence peak at 518 nm was monitored. Immediately, after adding the microgel the fluorescence signal is quenched to a large extent, which means that Lysozyme<sup>FITC</sup> has penetrated the polymeric layer. In the next step the concentration of the second competing protein was increased successively by multiple injections from a protein stock solution of well-defined concentration. After each injection the system was allowed to equilibrate for 5 min. If a second protein competes for binding sites, lysozyme<sup>FITC</sup> will be desorbed from the microgel and as a consequence the fluorescence signal increases proportional to the number of liberated labelled proteins. This effect can be used to quantify the number of bound lysozyme<sup>FITC</sup> as a function of a second competing protein. In particular, the amount of adsorbed lysozyme<sup>FITC</sup> is simply the difference between the total protein concentration  $c_p^{\text{tot}}$  and the concentration of non-adsorbed protein  $c_i$ , which can be calculated from the calibration line easily (intensity vs. protein concentration).

## 6.6 Atomic Force Microscopy

### 6.6.1 Substrate Preparation

Silicon wafers (1.5 mm $\times$ 1.5 mm) were cleaned for 24 h by submersion in piranha etch (70% v/v sulfuric acid 98% with 30% v/v hydrogen peroxide, 30% aqueous solution) at room temperature. Afterwards, the wafers were rinsed extensively with Milli-Q water (Millipore Corp.) and ethanol and dried under nitrogen airflow.

For the silanization the cleaned wafers were submerged in a 15% APTES solution in dry ethanol for 12 h. After washing the wafers alternately with ethanol and Milli-Q water, they were centrifuged at 600 rpm for  $\approx 2$ -3 minutes in order to remove the residual liquid film and to facilitate the formation of a uniform APTES layer. In the last step the wafers were dried in an oven preset to 125° C.

Poly-L-lysine hydrobromide (PLL) coated silicon wafers were fabricated by dip coating as described previously by Hasmi et al.<sup>110</sup> The clean wafers were submerged with a buffered solution of 10 mg/ml PLL (10 mM MOPS, 2 mM NaN<sub>3</sub> and 100 mM NaCl at pH = 7.2) and the solution was allowed to soak for 2 h. Then the wafers were thoroughly rinsed with Milli-Q water and dried under nitrogen airflow.

Wafers containing the microgel particles were prepared by placing one drop of  $\approx 1 \mu\text{L}$  of a 0.005 % w/w microgel solution on the APTES and PLL functionalized wafers. The wafers were then dried under room temperature until the drop evaporates and a thin uniform white film emerges on the surface. In the last step the wafers were washed again with Milli-Q water and dried under nitrogen airflow. For measurements in liquid, a drop of the same microgel solution was dipped onto the wafer and placed in the AFM liquid cell *in situ*.

## 6.6.2 AFM Measurements and Analysis

Atomic Force Microscopy was used as an additional method to confirm the morphology of the core-shell microgel on a surface. Images were recorded under room temperature with a multimode AFM microscope (Bruker Nanoscope V Multimode®8) using tapping mode in air and silicon nitride cantilever ( $k_F = 0.350$  N/m,  $f_0 = 65$  kHz,  $R_{tip} = 20$  nm, Bruker model DNP-10). Mechanical properties were obtained using Peak Force mode in liquid. Raw data of cantilever deflection vs. piezoelectric driver displacement was converted to force vs. distance by defining the deflection sensitivity from a clean bare silica surface in aqueous solution without microgels present. The images and height profiles have been analyzed with NanoScope Analysis Version 1.50 (Bruker).

## 6.7 SAXS

SAXS measurements were done on a SAXSess mc<sup>2</sup> instrument (Anton Paar, Austria). The instrument was equipped with a Cu K $\alpha$  slit-collimated radiation source which was operated at 40 kV. A fluid flow cell with 1 mm quartz capillary was used for all samples. Samples of 20, 30, 40 and 50 mg/ml glucosidase in 10 mM MOPS and 2 mM NaN<sub>3</sub> at pH = 7.2 were prepared. The ionic strength was adjusted to I = 107 mM with NaCl. Data reduction and desmearing was done using the Saxsquant 3.50 software.

## 6.8 ASAXS

### 6.8.1 Sample Preparation

Following samples were prepared for the ASAXS measurements: i) 1%(w/w) microgel ii) 1%(w/w) microgel loaded with 5mg mL<sup>-1</sup> cytochrome c corresponding to a saturated system at a molar ratio of approximately 4.800 and iii) 5mg mL<sup>-1</sup> cytochrome c. All samples were prepared in 10mM MOPS, 2 mM NaN<sub>3</sub> at pH = 7.2 and tempered to 293K.

### 6.8.2 Technical Details

ASAXS measurements were performed using the 7T-MPW-SAXS beam line at BESSY II58 within an energy range of 300 eV in the vicinity of the K-absorption edge of Fe at 7112 eV. With sample detector distances of 1000 mm and 3344 mm a q-range from 0.06 nm<sup>-1</sup> to 3 nm<sup>-1</sup> was covered, which corresponds to structural sizes between 2 nm and 100 nm. All data sets have been corrected for background scattering, detector sensitivity, detector dead time and dark current. After normalization to the primary flux the scattering curves are calibrated into macroscopic scattering cross sections in units of cross section per unit volume [ $\text{cm}^2/\text{cm}^3$ ]=[ $\text{cm}^{-1}$ ].

## 7 Appendix

### 7.1 Frequently used variables for the derivation of the Cooperative Binding Model

Table 7.1: Overview of frequently used variables for the derivation of the cooperative binding model.

variable	meaning
$R_h$	gel radius
$V_g$	gel volume
$R_i$	radius of $i$ -th protein
$z_i$	valency of $i$ -th protein
$c_g$	charge monomer concentration in the gel
$c_s$	bulk salt concentration
$\kappa_g$	inverse Debye length in gel
$\kappa_b$	inverse Debye length in bulk
$c_p^{tot}$	total protein concentration
$c_i^{tot}$	total concentration of $i$ -th protein
$c_i$	equilibrium bulk concentration of $i$ -th protein
$c_m$	microgel concentration
$x$	molar ratio $c_p^{tot}/c_m$
$N_i$	number of protein $i$ bound to the gel (CB-model)
$N_b$	number of protein $i$ bound to the gel (Langmuir)
$N$	Total number of binding sites
$\theta$	binding fraction $N_i/N$
$\bar{\phi}$	Donnan potential
$K$	binding constant
constant	meaning
$R_{core} = 62.2 \text{ nm}$	core radius
$N_g = 4.9 \cdot 10^5$	number of charged monomers per colloid
$z_g = -1$	monomer charge
$l_B = 0.7 \text{ nm}$	Bjerrum length in water

## 8 Bibliography

- [1] Xu, X.; ; Lenhoff, A. M. A Predictive Approach to Correlating Protein Adsorption Isotherms on Ion-Exchange Media. *The Journal of Physical Chemistry B* **2008**, *112*, 1028–1040.
- [2] Almeida, J. R.; Vasconcelos, V. Natural antifouling compounds: Effectiveness in preventing invertebrate settlement and adhesion. *Biotechnology Advances* **2015**, *33*, 343 – 357.
- [3] Gittens, J. E.; Smith, T. J.; Suleiman, R.; Akid, R. Current and emerging environmentally-friendly systems for fouling control in the marine environment. *Biotechnology Advances* **2013**, *31*, 1738 – 1753.
- [4] Nurioglu, A. G.; Esteves, A. C. C.; de With, G. Non-toxic, non-biocide-release antifouling coatings based on molecular structure design for marine applications. *J. Mater. Chem. B* **2015**, *3*, 6547–6570.
- [5] Kottke-Marchant, K.; Anderson, J.; Umemura, Y.; Marchant, R. Effect of albumin coating on the in vitro blood compatibility of Dacron arterial prostheses. *Biomaterials* **1989**, *10*, 147—155.
- [6] Kossovsky, N.; Millett, D.; Juma, S.; Little, N.; Briggs, P. C.; Raz, S.; Berg, E. In vivo characterization of the inflammatory properties of poly(tetrafluoroethylene) particulates. *Journal of Biomedical Materials Research* **1991**, *25*, 1287–1301.
- [7] W, C. R. Surface-mediated defense reactions: the plasma contact activation system. *J Clin Invest* **1984**, *73*, 1249–1253.
- [8] B, J.; G, P.; G, P. Mechanisms and clinical relevance of bacterial adhesion to polymers. *J Biomater Appl.* **1987**, *2*, 520–543.
- [9] Hu, W. J.; Eaton, J. W.; Ugarova, T. P.; Tang, L. Molecular basis of biomaterial-mediated foreign body reactions. *Blood* **2001**, *98*, 1231–8.
- [10] Hucknall, A.; Kim, D.-H.; Rangarajan, S.; Hill, R. T.; Reichert, W. M.; Chilkoti, A. Simple Fabrication of Antibody Microarrays on Nonfouling Polymer Brushes with Femtomolar Sensitivity for Protein Analytes in Serum and Blood. *Advanced Materials* **2009**, *21*, 1968–1971.
- [11] Vroman, L. Effect of Adsorbed Proteins on the Wettability of Hydrophilic and Hydrophobic Solids. *Nature* **1962**, *196*, 476–477.

- [12] Vroman, L.; Adams, A. L. Findings with the recording ellipsometer suggesting rapid exchange of specific plasma proteins at liquid/solid interfaces. *Surface Science* **1969**, *16*, 438–446.
- [13] Vroman, L.; Adams, A. L. Identification of rapid changes at plasma solid interfaces. *Journal of Biomedical Materials Research* **1969**, *3*, 43–67.
- [14] Vroman, L.; Adams, A.; Fischer, G.; Munoz, P. Interaction of high molecular weight kininogen, factor XII, and fibrinogen in plasma at interfaces. *Blood* **1980**, *55*, 156–159.
- [15] Holmberg, M.; Hou, X. Competitive Protein Adsorption of Albumin and Immunoglobulin G from Human Serum onto Polymer Surfaces. *Langmuir* **2009**, *26*, 938–942.
- [16] Ortega-Vinuesa, J. L.; Hidalgo-Alvarez, R. Sequential adsorption of F(ab)<sub>2</sub> and BSA on negatively and positively charged polystyrene latexes. *Biotechnology and Bioengineering* **1995**, *47*, 633–639.
- [17] Norde, W.; Giacomelli, C. E. BSA structural changes during homomolecular exchange between the adsorbed and the dissolved states. *Journal of Biotechnology* **2000**, *79*, 259 – 268.
- [18] Norde, W.; Giacomelli, C. E. Conformational changes in proteins at interfaces: From solution to the interface, and back. *Macromolecular Symposia* **1999**, *145*, 125–136.
- [19] Green, R. J.; Davies, M. C.; Roberts, C. J.; Tendler, S. J. B. Competitive protein adsorption as observed by surface plasmon resonance. *Biomaterials* **1999**, *20*, 385–391.
- [20] Ying, P.; Yu, Y.; Jin, G.; Tao, Z. Competitive protein adsorption studied with atomic force microscopy and imaging ellipsometry. *Colloids and Surfaces B: Biointerfaces* **2003**, *32*, 1–10.
- [21] Gun'ko, V. M.; Mikhalovska, L. I.; Tomlins, P. E.; Mikhalovsky, S. V. Competitive adsorption of macromolecules and real-time dynamics of Vroman-like effects. *Physical Chemistry Chemical Physics* **2011**, *13*, 4476–4485.
- [22] Lassen, B.; Malmsten, M. Competitive Protein Adsorption at Plasma Polymer Surfaces. *Journal of Colloid and Interface Science* **1997**, *186*, 9–16.
- [23] Huang, R.; Carney, R. R.; Ikuma, K.; Stellacci, F.; Lau, B. L. T. Effects of Surface Compositional and Structural Heterogeneity on Nanoparticle-Protein Interactions: Different Protein Configurations. *ACS NANO* **2014**, *8*, 5402–5412.
- [24] Huang, Y.; Lai, X.; Qian, W.; Tang, Z.; Zhong, Y. Competitive protein adsorption on biomaterial surface studied with reflectometric interference spectroscopy. *Acta Biomaterialia* **2010**, *6*, 2083–2090.
- [25] Riedel, T.; Riedelova-Reicheltova, Z.; Majek, P.; Rodriguez-Emmenegger, C.; Houska, M.; Dyr, J. E.; Brynda, E. Complete Identification of Proteins Responsible for Human Blood Plasma Fouling on Poly(ethylene glycol)-Based Surfaces. *Langmuir* **2013**, *29*, 3388–3397.

- [26] Mohr, K.; Sommer, M.; Baier, G.; Schöttler, S.; Okwieka, P.; Tenzer, S.; Katharina, L.; Mailänder, V.; Schmidt, M.; Georg Meyer, R. Aggregation Behavior of Polystyrene-Nanoparticles in Human Blood Serum and its Impact on the in vivo Distribution in Mice. *Journal of Nanomedicine & Nanotechnology* **2014**,
- [27] Tenzer, S.; Docter, D.; Kuharev, J.; Musyanovych, A.; Fetz, V.; Hecht, R.; Schlenk, F.; Fischer, D.; Kiouptsi, K.; Reinhardt, C.; Landfester, K.; Schild, H.; Maskos, M.; Knauer, S. K.; Stauber, R. H. Rapid formation of plasma protein corona critically affects nanoparticle pathophysiology. *Nat Nano* **2013**, *8*, 772–781.
- [28] Aggarwal, P.; Hall, J. B.; McLeland, C. B.; Dobrovolskaia, M. A.; McNeil, S. E. Nanoparticle interaction with plasma proteins as it relates to particle biodistribution, biocompatibility and therapeutic efficacy. *Adv Drug Deliv Rev* **2009**, *61*, 428–37.
- [29] Mahmoudi, M.; Lynch, I.; Ejtehadi, M. R.; Monopoli, M. P.; Bombelli, F. B.; Laurent, S. Protein-Nanoparticle Interactions: Opportunities and Challenges. *Chemical Reviews* **2011**, *111*, 5610–5637.
- [30] Monopoli, M. P.; Aberg, C.; Salvati, A.; Dawson, K. A. Biomolecular coronas provide the biological identity of nanosized materials. *Nat Nano* **2012**, *7*, 779–786.
- [31] Walkey, C. D.; Chan, W. C. Understanding and controlling the interaction of nanomaterials with proteins in a physiological environment. *Chem Soc Rev* **2012**, *41*, 2780–99.
- [32] Walkey, C. D.; Olsen, J. B.; Guo, H.; Emili, A.; Chan, W. C. W. Nanoparticle Size and Surface Chemistry Determine Serum Protein Adsorption and Macrophage Uptake. *Journal of the American Chemical Society* **2012**, *134*, 2139–2147.
- [33] Walczyk, D.; Bombelli, F. B.; Monopoli, M. P.; Lynch, I.; Dawson, K. A. What the Cell Sees in Bionanoscience. *Journal of the American Chemical Society* **2010**, *132*, 5761–5768.
- [34] Wei, Q.; Becherer, T.; Angioletti-Uberti, S.; Dzubiella, J.; Wischke, C.; Neffe, A. T.; Lendlein, A.; Ballauff, M.; Haag, R. Protein interactions with polymer coatings and biomaterials. *Angew Chem Int Ed Engl* **2014**, *53*, 8004–31.
- [35] Winzen, S.; Schoettler, S.; Baier, G.; Rosenauer, C.; Mailänder, V.; Landfester, K.; Mohr, K. Complementary analysis of the hard and soft protein corona: sample preparation critically effects corona composition. *Nanoscale* **2015**, *7*, 2992–3001.
- [36] Milani, S.; Bombelli, F. B.; Pitek, A. S.; Dawson, K. A.; Rädler, J. Reversible versus Irreversible Binding of Transferrin to Polystyrene Nanoparticles: Soft and Hard Corona. *ACS Nano* **2012**, *6*, 2532–2541.
- [37] Rocker, C.; Potzl, M.; Zhang, F.; Parak, W. J.; Nienhaus, G. U. A quantitative fluorescence study of protein monolayer formation on colloidal nanoparticles. *Nat Nano* **2009**, *4*, 577–580.



- [38] Maffre, P.; Nienhaus, K.; Amin, F.; Parak, W. J.; Nienhaus, G. U. Characterization of protein adsorption onto FePt nanoparticles using dual-focus fluorescence correlation spectroscopy. *Beilstein Journal of Nanotechnology* **2011**, 2, 374–383.
- [39] Deng, Z. J.; Liang, M.; Monteiro, M.; Toth, I.; Minchin, R. F. Nanoparticle-induced unfolding of fibrinogen promotes Mac-1 receptor activation and inflammation. *Nat Nano* **2011**, 6, 39–44.
- [40] Hoshino, Y.; Koide, H.; Furuya, K.; Haberaecker, W. W.; Lee, S.-H.; Kodama, T.; Kanazawa, H.; Oku, N.; Shea, K. J. The rational design of a synthetic polymer nanoparticle that neutralizes a toxic peptide in vivo. *Proceedings of the National Academy of Sciences* **2012**, 109, 33–38.
- [41] Salvati, A.; Pitek, A. S.; Monopoli, M. P.; Prapainop, K.; Bombelli, F. B.; Hristov, D. R.; Kelly, P. M.; Aberg, C.; Mahon, E.; Dawson, K. A. Transferrin-functionalized nanoparticles lose their targeting capabilities when a biomolecule corona adsorbs on the surface. *Nat Nano* **2013**, 8, 137–143.
- [42] Karakoti, A. S.; Das, S.; Thevuthasan, S.; Seal, S. PEGylated Inorganic Nanoparticles. *Angewandte Chemie International Edition* **2011**, 50, 1980–1994.
- [43] Jokerst, J. V.; Lobovkina, T.; Zare, R. N.; Gambhir, S. S. Nanoparticle PEGylation for Imaging and Therapy. *Nanomedicine* **2011**, 6, 715–728.
- [44] Hamad, I.; Al-Hanbali, O.; Hunter, A. C.; Rutt, K. J.; Andresen, T. L.; Moghimi, S. M. Distinct Polymer Architecture Mediates Switching of Complement Activation Pathways at the Nanosphere-Serum Interface: Implications for Stealth Nanoparticle Engineering. *ACS Nano* **2010**, 4, 6629–6638.
- [45] Yang, W.; Zhang, L.; Wang, S.; White, A. D.; Jiang, S. Functionalizable and ultra stable nanoparticles coated with zwitterionic poly(carboxybetaine) in undiluted blood serum. *Biomaterials* **2009**, 30, 5617 – 5621.
- [46] Rosen, J. E.; Gu, F. X. Surface Functionalization of Silica Nanoparticles with Cysteine: A Low-Fouling Zwitterionic Surface. *Langmuir* **2011**, 27, 10507–10513.
- [47] Moyano, D. F.; Saha, K.; Prakash, G.; Yan, B.; Kong, H.; Yazdani, M.; Rotello, V. M. Fabrication of Corona-Free Nanoparticles with Tunable Hydrophobicity. *ACS Nano* **2014**, 8, 6748–6755.
- [48] Jackson, M. B. *Molecular and Cellular Biophysics*; Cambridge University Press: New York, 2006.
- [49] Latour, R. A. The langmuir isotherm: A commonly applied but misleading approach for the analysis of protein adsorption behavior. *Journal of Biomedical Materials Research Part A* **2015**, 103, 949–958.
- [50] LeDuc, C. A.; Vroman, L.; Leonard, E. F. A Mathematical Model for the Vroman Effect. *Industrial & Engineering Chemistry Research* **1995**, 34, 3488–3495.

- [51] Dell’Orco, D.; Lundqvist, M.; Oslakovic, C.; Cedervall, T.; Linse, S. Modeling the Time Evolution of the Nanoparticle-Protein Corona in a Body Fluid. *PLoS ONE* **2010**, *5*, e10949.
- [52] Dell’Orco, D.; Lundqvist, M.; Linse, S.; Cedervall, T. Mathematical modeling of the protein corona: implications for nanoparticulate delivery systems. *Nanomedicine (Lond)* **2014**, *9*, 851–8.
- [53] Brooks, C. A.; Cramer, S. M. Steric mass-action ion exchange: Displacement profiles and induced salt gradients. *AIChE Journal* **1992**, *38*, 1969–1978.
- [54] Noh, H.; Vogler, E. A. Volumetric interpretation of protein adsorption: Competition from mixtures and the Vroman effect. *Biomaterials* **2007**, *28*, 405–422.
- [55] Vogler, E. A. Protein adsorption in three dimensions. *Biomaterials* **2012**, *33*, 1201 – 1237.
- [56] Su, X.-L.; Sun, Y. Thermodynamic model for nonlinear electrostatic adsorption equilibrium of protein. *AIChE Journal* **2006**, *52*, 2921–2930.
- [57] Fang, F.; Szleifer, I. Competitive adsorption in model charged protein mixtures: Equilibrium isotherms and kinetics behavior. *The Journal of Chemical Physics* **2003**, *119*, 1053–1065.
- [58] Vilaseca, P.; Dawson, K. A.; Franzese, G. Understanding and modulating the competitive surface-adsorption of proteins through coarse-grained molecular dynamics simulations. *Soft Matter* **2013**, *9*, 6978–6985.
- [59] Yigit, C.; Welsch, N.; Ballauff, M.; Dzubiella, J. Protein sorption to charged microgels: Characterizing binding isotherms and driving forces. *Langmuir* **2012**, *28*, 14373–85.
- [60] Tanaka, T.; Fillmore, D. J. Kinetics of swelling of gels. *The Journal of Chemical Physics* **1979**, *70*, 1214–1218.
- [61] Hendrickson, G. R.; Smith, M. H.; South, A. B.; Lyon, L. A. Design of Multiresponsive Hydrogel Particles and Assemblies. *Advanced Functional Materials* **2010**, *20*, 1697–1712.
- [62] Hendrickson, G. R.; Andrew Lyon, L. Bioresponsive hydrogels for sensing applications. *Soft Matter* **2009**, *5*, 29–35.
- [63] Saxena, S.; Hansen, C. E.; Lyon, L. A. Microgel Mechanics in Biomaterial Design. *Accounts of Chemical Research* **2014**, *47*, 2426–2434.
- [64] Kratz, K.; Hellweg, T.; Eimer, W. Structural changes in PNIPAM microgel particles as seen by SANS, DLS, and EM techniques. *Polymer* **2001**, *42*, 6631 – 6639.
- [65] Hoare, T.; Pelton, R. Highly pH and Temperature Responsive Microgels Functionalized with Vinylacetic Acid. *Macromolecules* **2004**, *37*, 2544–2550.

- [66] Sershen, S. R.; Westcott, S. L.; Halas, N. J.; West, J. L. Temperature-sensitive polymeric nanoshell composites for photothermally modulated drug delivery. *Journal of Biomedical Materials Research* **2000**, *51*, 293–298.
- [67] Duracher, D.; Sauzedde, F.; Elaassari, A.; Pichot, C.; Nabzar, L. Cationic amino-containing N-isopropyl- acrylamide-styrene copolymer particles: 2-surface and colloidal characteristics. *Colloid and Polymer Science* **1998**, *276*, 920–929.
- [68] Welsch, N.; Becker, A. L.; Dzubiel, J.; Ballauff, M. Core-shell microgels as smart carriers for enzymes. *Soft Matter* **2012**, *8*, 1428–1436.
- [69] Kubota, K.; Fujishige, S.; Ando, I. Single-chain transition of poly(N-isopropylacrylamide) in water. *The Journal of Physical Chemistry* **1990**, *94*, 5154–5158.
- [70] Heskins, M.; Guillet, J. E. Solution Properties of Poly(N-isopropylacrylamide). *Journal of Macromolecular Science: Part A - Chemistry* **1968**, *2*, 1441–1455.
- [71] Ballauff, M.; Lu, Y. Smart nanoparticles: Preparation, characterization and applications. *Polymer* **2007**, *48*, 1815 – 1823.
- [72] Jones, C. D.; Lyon, L. A. Synthesis and characterization of multiresponsive core-shell microgels. *Macromolecules* **2000**, *33*, 8301–8306.
- [73] Crassous, J. J.; Wittemann, A.; Siebenbürger, M.; Schrinner, M.; Drechsler, M.; Ballauff, M. Direct imaging of temperature-sensitive core-shell latexes by cryogenic transmission electron microscopy. *Colloid and Polymer Science* **2008**, *286*, 805–812.
- [74] Crassous, J. J.; Rochette, C. N.; Wittemann, A.; Schrinner, M.; Ballauff, M.; Drechsler, M. Quantitative Analysis of Polymer Colloids by Cryo-Transmission Electron Microscopy. *Langmuir* **2009**, *25*, 7862–7871.
- [75] Dingenouts, N.; Norhausen, C.; Ballauff, M. Observation of the Volume Transition in Thermosensitive Core-Shell Latex Particles by Small-Angle X-ray Scattering. *Macromolecules* **1998**, *31*, 8912–8917.
- [76] N. Dingenouts, .; M. Patel, .; S. Rosenfeldt, .; D. Pontoni, .; T. Narayanan, .; ; M. Ballauff\*, . Counterion Distribution around a Spherical Polyelectrolyte Brush Probed by Anomalous Small-Angle X-ray Scattering. *Macromolecules* **2004**, *37*, 8152–8159.
- [77] Dingenouts, N.; Seelenmeyer, S.; Deike, I.; Rosenfeldt, S.; Ballauff, M.; Lindner, P.; Narayanan, T. Analysis of thermosensitive core-shell colloids by small-angle neutron scattering including contrast variation. *Phys. Chem. Chem. Phys.* **2001**, *3*, 1169–1174.
- [78] Crassous, J. J.; Siebenbürger, M.; Ballauff, M.; Drechsler, M.; Henrich, O.; Fuchs, M. Thermosensitive core-shell particles as model systems for studying the flow behavior of concentrated colloidal dispersions. *The Journal of Chemical Physics* **2006**, *125*.

- [79] Lu, Y.; Proch, S.; Schrunner, M.; Drechsler, M.; Kempe, R.; Ballauff, M. Thermosensitive core-shell microgel as a nanoreactor for catalytic active metal nanoparticles. *J. Mater. Chem.* **2009**, *19*, 3955–3961.
- [80] Welsch, N. Interactions of Proteins with Soft Polymeric Surfaces: Driving Forces and Kinetics. Ph.D. thesis, Reports of the Helmholtz Centre Berlin (HZB-Berichte), 2012.
- [81] Welsch, N.; Wittemann, A.; Ballauff, M. Enhanced Activity of Enzymes Immobilized in Thermoresponsive Core-Shell Microgels. *The Journal of Physical Chemistry B* **2009**, *113*, 16039–16045.
- [82] Kawaguchi, H.; Fujimoto, K.; Mizuhara, Y. Hydrogel microspheres III. Temperature-dependent adsorption of proteins on poly-N-isopropylacrylamide hydrogel microspheres. *Colloid and Polymer Science* **1992**, *270*, 53–57.
- [83] Cole, M. A.; Voelcker, N. H.; Thissen, H.; Horn, R. G.; Griesser, H. J. Colloid probe AFM study of thermal collapse and protein interactions of poly(N-isopropylacrylamide) coatings. *Soft Matter* **2010**, *6*, 2657–2667.
- [84] Grabstain, V.; Bianco-Peled, H. Mechanisms Controlling the Temperature-Dependent Binding of Proteins to Poly(N-isopropylacrylamide) Microgels. *Biotechnology Progress* **2003**, *19*, 1728–1733.
- [85] Lindman, S.; Lynch, I.; Thulin, E.; Nilsson, H.; Dawson, K. A.; Linse, S. Systematic Investigation of the Thermodynamics of HSA Adsorption to N-iso-Propylacrylamide/N-tert-Butylacrylamide Copolymer Nanoparticles. Effects of Particle Size and Hydrophobicity. *Nano Letters* **2007**, *7*, 914–920.
- [86] Johansson, C.; Gernandt, J.; Bradley, M.; Vincent, B.; Hansson, P. Interaction between lysozyme and colloidal poly(NIPAM-co-acrylic acid) microgels. *Journal of Colloid and Interface Science* **2010**, *347*, 241 – 251.
- [87] Smith, M. H.; Lyon, L. A. Tunable Encapsulation of Proteins within Charged Microgels. *Macromolecules* **2011**, *44*, 8154–8160.
- [88] Flory, P. J. *Principles of Polymer Chemistry*; Cornell University Press: Ithaca, NY, 1953, 1953.
- [89] Huo, D.; Li, Y.; Qian, Q.; Kobayashi, T. Temperature and pH sensitivity of bovine serum albumin protein-microgels based on cross-linked poly(N-isopropylacrylamide-co-acrylic acid). *Colloids and Surfaces B: Biointerfaces* **2006**, *50*, 36 – 42.
- [90] Yan, C.; Elaissari, A.; Pichot, C. Loading and Release Studies of Proteins Using Poly(N-isopropylacrylamide) Based Nanogels. *Journal of Biomedical Nanotechnology* **2006**, *2*, 208–216.

- [91] Becker, A. L.; Welsch, N.; Schneider, C.; Ballauff, M. Adsorption of RNase A on Cationic Polyelectrolyte Brushes: A Study by Isothermal Titration Calorimetry. *Biomacromolecules* **2011**, *12*, 3936–3944.
- [92] Wittemann, A.; Haupt, B.; Ballauff, M. Adsorption of proteins on spherical polyelectrolyte brushes in aqueous solution. *Physical Chemistry Chemical Physics* **2003**, *5*, 1671–1677.
- [93] Lund, M.; Akesson, T.; Jonsson, B. Enhanced Protein Adsorption Due to Charge Regulation. *Langmuir* **2005**, *21*, 8385–8388.
- [94] Lund, M.; Jonsson, B. On the Charge Regulation of Proteins. *Biochemistry* **2005**, *44*, 5722–5727.
- [95] Longo, G. S.; de la Cruz, M. O.; Szleifer, I. Molecular Theory of Weak Polyelectrolyte Gels: The Role of pH and Salt Concentration. *Macromolecules* **2011**, *44*, 147–158.
- [96] Biesheuvel, P. M.; Wittemann, A. A Modified Box Model Including Charge Regulation for Protein Adsorption in a Spherical Polyelectrolyte Brush. *The Journal of Physical Chemistry B* **2005**, *109*, 4209–4214.
- [97] Bysell, H.; Hansson, P.; Malmsten, M. Effect of Charge Density on the Interaction between Cationic Peptides and Oppositely Charged Microgels. *The Journal of Physical Chemistry B* **2010**, *114*, 7207–7215.
- [98] Welsch, N.; Dzubiella, J.; Graebert, A.; Ballauff, M. Protein binding to soft polymeric layers: a quantitative study by fluorescence spectroscopy. *Soft Matter* **2012**, *8*, 12043–12052.
- [99] Angioletti-Uberti, S.; Ballauff, M.; Dzubiella, J. Dynamic density functional theory of protein adsorption on polymer-coated nanoparticles. *Soft Matter* **2014**, *10*, 7932–7945.
- [100] Buschmann, M. D.; Grodzinsky, A. J. A molecular model of proteoglycan-associated electrostatic forces in cartilage mechanics. *J Biomech Eng* **1995**, *117*, 179–92.
- [101] Dubrovskii, S.; Rakova, G.; Lagutina, M.; Kazanskii, K. Osmotic properties of poly(ethylene oxide) gels with localized charged units. *Polymer* **2001**, *42*, 8075 – 8083.
- [102] Horkay, F.; Zrinyi, M. Studies on the mechanical and swelling behavior of polymer networks based on the scaling concept. 4. Extension of the scaling approach to gels swollen to equilibrium in a diluent of arbitrary activity. *Macromolecules* **1982**, *15*, 1306–1310.
- [103] Rubinstein, M.; ; Colby, R. H.; Dobrynin, A. V.; Joanny, J.-F. Elastic Modulus and Equilibrium Swelling of Polyelectrolyte Gels. *Macromolecules* **1996**, *29*, 398–406.
- [104] Hu, Z.; Li, C.; Li, Y. The scaling exponents of polyacrylamide and acrylamide and sodium acrylate copolymer gels. *The Journal of Chemical Physics* **1993**, *99*, 7108–7114.
- [105] Horkay, F.; Tasaki, I.; Basser, P. J. Osmotic Swelling of Polyacrylate Hydrogels in Physiological Salt Solutions. *Biomacromolecules* **2000**, *1*, 84–90.

- [106] Fernandes, P. A. L.; Schmidt, S.; Zeiser, M.; Fery, A.; Hellweg, T. Swelling and mechanical properties of polymer gels with cross-linking gradient. *Soft Matter* **2010**, *6*, 3455–3458.
- [107] Geissler, E.; Horkay, F.; Hecht, A.-M. Structure and thermodynamics of flexible polymer gels. *The Journal of Chemical Physics* **1994**, *100*, 8418–8424.
- [108] Lu, Y.; Drechsler, M. Charge-Induced Self-Assembly of 2-Dimensional Thermosensitive Microgel Particle Patterns. *Langmuir* **2009**, *25*, 13100–13105.
- [109] Höfl, S.; Zitzler, L.; Hellweg, T.; Herminghaus, S.; Mugele, F. Volume phase transition of smart microgels in bulk solution and adsorbed at an interface: A combined AFM, dynamic light, and small angle neutron scattering study. *Polymer* **2007**, *48*, 245 – 254.
- [110] Hashmi, S. M.; Dufresne, E. R. Mechanical properties of individual microgel particles through the deswelling transition. *Soft Matter* **2009**, *5*, 3682–3688.
- [111] Linse, S.; Cabaleiro-Lago, C.; Xue, W.-F.; Lynch, I.; Lindman, S.; Thulin, E.; Radford, S. E.; Dawson, K. A. Nucleation of protein fibrillation by nanoparticles. *Proceedings of the National Academy of Sciences* **2007**, *104*, 8691–8696.
- [112] Henzler, K.; Haupt, B.; Lauterbach, K.; Wittemann, A.; Borisov, O.; Ballauff, M. Adsorption of beta-Lactoglobulin on Spherical Polyelectrolyte Brushes: Direct Proof of Counterion Release by Isothermal Titration Calorimetry. *Journal of the American Chemical Society* **2010**, *132*, 3159–3163.
- [113] Hu, F.; Chen, K.; Xu, H.; Gu, H. Functional short-chain zwitterion coated silica nanoparticles with antifouling property in protein solutions. *Colloids and Surfaces B: Biointerfaces* **2015**, *126*, 251–256.
- [114] Chakraborti, S.; Joshi, P.; Chakravarty, D.; Shanker, V.; Ansari, Z. A.; Singh, S. P.; Chakrabarti, P. Interaction of Polyethyleneimine-Functionalized ZnO Nanoparticles with Bovine Serum Albumin. *Langmuir* **2012**, *28*, 11142–11152.
- [115] Fleischer, C. C.; Payne, C. K. Secondary Structure of Corona Proteins Determines the Cell Surface Receptors Used by Nanoparticles. *The Journal of Physical Chemistry B* **2014**, *118*, 14017–14026.
- [116] Baier, G.; Costa, C.; Zeller, A.; Baumann, D.; Sayer, C.; Araujo, P. H. H.; Mailänder, V.; Musyanovych, A.; Landfester, K. BSA Adsorption on Differently Charged Polystyrene Nanoparticles using Isothermal Titration Calorimetry and the Influence on Cellular Uptake. *Macromolecular Bioscience* **2011**, *11*, 628–638.
- [117] Li, X.; Chen, M.; Yang, W.; Zhou, Z.; Liu, L.; Zhang, Q. Interaction of bovine serum albumin with self-assembled nanoparticles of 6-O-cholesterol modified chitosan. *Colloids and Surfaces B: Biointerfaces* **2012**, *92*, 136–141.

- [118] Zhao, T.; Chen, K.; Gu, H. Investigations on the Interactions of Proteins with Polyampholyte-Coated Magnetite Nanoparticles. *The Journal of Physical Chemistry B* **2013**, *117*, 14129–14135.
- [119] Henzler, K.; Wittemann, A.; Breininger, E.; Ballauff, M.; Rosenfeldt, S. Adsorption of Bovine Hemoglobin onto Spherical Polyelectrolyte Brushes Monitored by Small-Angle X-ray Scattering and Fourier Transform Infrared Spectroscopy. *Biomacromolecules* **2007**, *8*, 3674–3681.
- [120] Wang, S.; Chen, K.; Li, L.; Guo, X. Binding between Proteins and Cationic Spherical Polyelectrolyte Brushes: Effect of pH, Ionic Strength, and Stoichiometry. *Biomacromolecules* **2013**, *14*, 818–827.
- [121] Sanchez-Moreno, P.; Buzon, P.; Boulaiz, H.; Peula-Garcia, J.; Ortega-Vinuesa, J.; Luque, I.; Salvati, A.; Marchal, J. Balancing the effect of corona on therapeutic efficacy and macrophage uptake of lipid nanocapsules. *Biomaterials* **2015**, *61*, 266 – 278.
- [122] Oberle, M.; Yigit, C.; Angioletti-Uberti, S.; Dzubiella, J.; Ballauff, M. Competitive Protein Adsorption to Soft Polymeric Layers: Binary Mixtures and Comparison to Theory. *The Journal of Physical Chemistry B* **2015**, *119*, 3250–3258.
- [123] Atkins, P. W.; De., P. J. *Atkins' Physical Chemistry 7th Ed.*; Oxford: Oxford University Press, 2006.
- [124] Lide, D. R., Ed. *CRC Handbook of Chemistry and Physics 90th Edition*; Taylor & Francis Ltd., 2009.
- [125] Ladbury, J. E.; Chowdhry, B. Z. *Biocalorimetry*; John Wiley&Sons, 1998.
- [126] Turnbull, W. B.; Daranas, A. H. On the value of c: Can low affinity systems be studied by isothermal titration calorimetry? *J. Am. Chem. Soc.* **2003**, *125*, 14859–14866.
- [127] Yu, S.; Xu, X.; Yigit, C.; van der Giet, M.; Zidek, W.; Jankowski, J.; Dzubiella, J.; Ballauff, M. Interaction of human serum albumin with short polyelectrolytes: a study by calorimetry and computer simulations. *Soft Matter* **2015**, *11*, 4630–4639.
- [128] Henzler, K.; Haupt, B.; Rosenfeldt, S.; Harnau, L.; Narayanan, T.; Ballauff, M. Interaction strength between proteins and polyelectrolyte brushes: a small angle X-ray scattering study. *Phys. Chem. Chem. Phys.* **2011**, *13*, 17599–17605.
- [129] Mackie, A. R.; Mingins, J.; North, A. N. Characterisation of adsorbed layers of a disordered coil protein on polystyrene latex. *J. Chem. Soc., Faraday Trans.* **1991**, *87*, 3043–3049.
- [130] Vauthier, C.; Lindner, P.; Cabane, B. Configuration of bovine serum albumin adsorbed on polymer particles with grafted dextran corona. *Colloids and Surfaces B: Biointerfaces* **2009**, *69*, 207 – 215.

- [131] Rosenfeldt, S.; Wittemann, A.; Ballauff, M.; Breininger, E.; Bolze, J.; Dingenouts, N. Interaction of proteins with spherical polyelectrolyte brushes in solution as studied by small-angle x-ray scattering. *Phys. Rev. E* **2004**, *70*, 061403.
- [132] Henzler, K.; Rosenfeldt, S.; Wittemann, A.; Harnau, L.; Finet, S.; Narayanan, T.; Ballauff, M. Directed Motion of Proteins along Tethered Polyelectrolytes. *Phys. Rev. Lett.* **2008**, *100*, 158301.
- [133] Bharti, B.; Meissner, J.; Findenegg, G. H. Aggregation of Silica Nanoparticles Directed by Adsorption of Lysozyme. *Langmuir* **2011**, *27*, 9823–9833, PMID: 21728288.
- [134] Goerigk, G.; Schweins, R.; Huber, K.; Ballauff, M. The distribution of Sr <sup>2+</sup> counterions around polyacrylate chains analyzed by anomalous small-angle X-ray scattering. *EPL (Europhysics Letters)* **2004**, *66*, 331–337.
- [135] Patel, M.; Rosenfeldt, S.; Ballauff, M.; Dingenouts, N.; Pontoni, D.; Narayanan, T. Analysis of the correlation of counterions to rod-like macroions by anomalous small-angle X-ray scattering. *Phys. Chem. Chem. Phys.* **2004**, *6*, 2962–2967.
- [136] Guilleaume, B.; Blaul, J.; Ballauff, M.; Wittemann, M.; Rehahn, M.; Goerigk, G. The distribution of counterions around synthetic rod-like polyelectrolytes in solution. *The European Physical Journal E* **2002**, *8*, 299–309.
- [137] Goerigk, G.; Huber, K.; Mattern, N.; Williamson, D. L. Quantitative anomalous small-angle X-ray scattering – The determination of chemical concentrations in nano-scaled phases. *Eur. Phys. J. Special Topics* **2012**, *208*, 259–274.
- [138] Boulos, S. P.; Davis, T. A.; Yang, J. A.; Lohse, S. E.; Alkilany, A. M.; Holland, L. A.; Murphy, C. J. Nanoparticle Protein Interactions: A Thermodynamic and Kinetic Study of the Adsorption of Bovine Serum Albumin to Gold Nanoparticle Surfaces. *Langmuir* **2013**, *29*, 14984–14996.
- [139] Bunz, U. H. F.; Rotello, M., Vincent Gold Nanoparticle-Fluorophore Complexes: Sensitive and Discerning Noses for Biosystems Sensing. *Angewandte Chemie International Edition* **2010**, *49*, 3268–3279.
- [140] Ohkuma, S.; Poole, B. Fluorescence probe measurement of the intralysosomal pH in living cells and the perturbation of pH by various agents. *Proceedings of the National Academy of Sciences of the United States of America* **1978**, *75*, 3327–3331.
- [141] Hungerford, G.; Benesch, J.; Mano, J. F.; Reis, R. L. Effect of the labelling ratio on the photo-physics of fluorescein isothiocyanate (FITC) conjugated to bovine serum albumin. *Photochem. Photobiol. Sci.* **2007**, *6*, 152–158.
- [142] Chen, R. F.; Knutson, J. R. Mechanism of fluorescence concentration quenching of carboxyfluorescein in liposomes: Energy transfer to nonfluorescent dimers. *Analytical Biochemistry* **1988**, *172*, 61 – 77.



- [143] Hansen, J. P.; McDonald, I. R. *Theory of Simple Liquids*; Academic Press: London, 2006.
- [144] Filatova, L. Y.; Oxenoyt, Y. S.; Yakovleva, K. S.; Ivanova, N. I.; Klyachko, N. L. Investigation of the activity and stability of papain in different micellar systems. *Moscow University Chemistry Bulletin* **2010**, 65, 80–86.
- [145] Hamill, A. C.; Wang, S.-C.; Lee, C. T. Probing Lysozyme Conformation with Light Reveals a New Folding Intermediate. *Biochemistry* **2005**, 44, 15139–15149.
- [146] Oleinikova, A.; Sasisanker, P.; Weingaertner, H. What Can Really Be Learned from Dielectric Spectroscopy of Protein Solutions? A Case Study of Ribonuclease A. *The Journal of Physical Chemistry B* **2004**, 108, 8467–8474.
- [147] Wilkins, D. K.; Grimshaw, S. B.; Receveur, V.; Dobson, C. M.; Jones, J. A.; Smith, L. J. Hydrodynamic Radii of Native and Denatured Proteins Measured by Pulse Field Gradient NMR Techniques. *Biochemistry* **1999**, 38, 16424–16431.
- [148] Giachini, L.; Francia, F.; Cordone, L.; Boscherini, F.; Venturoli, G. Cytochrome c in a Dry Trehalose Matrix: Structural and Dynamical Effects Probed by X-Ray Absorption Spectroscopy. *Biophysical Journal* **2007**, 92, 1350 – 1360.
- [149] Cromer, D. T.; Liberman, D. A. Anomalous dispersion calculations near to and on the long-wavelength side of an absorption edge. *Acta Crystallographica Section A* **1981**, 37, 267–268.
- [150] Cromer, D. T.; Liberman, D. Relativistic Calculation of Anomalous Scattering Factors for X Rays. *The Journal of Chemical Physics* **1970**, 53, 1891–1898.
- [151] Horecha, M.; Senkovskyy, V.; Synytska, A.; Stamm, M.; Chervanyov, A. I.; Kiriy, A. Ordered surface structures from PNIPAM-based loosely packed microgel particles. *Soft Matter* **2010**, 6, 5980–5992.

## 9 List of Abbreviations

AAc	Acrylic acid
AFM	Atomic Force Microscopy
APTES	3-Aminopropyl)triethoxysilane
ASAXS	Anamalous Small Angle X-Ray Scattering
BAM	N-tert-butylacrylamide
BIS	N,N'-Methylenebisacrylamide
BLG	$\beta$ -Lactoglobulin
BSA	Bovine Serum Albumin
CB-Model	Cooperative Binding Model
DMSO	Dimethylsulfoxide
DLS	Dynamic Light Scattering
FCS	Fluorescence Correlation Spectroscopy
FITC	Fluoresceinisothiocyanate
Fgn	Fibrinogen
HSA	Human Serum Albumin
ITC	Isothermal Titration Calorimetry
KPS	Potassium peroxodisulfate
LCST	Lower Critical Solution Temperature
MOPS	3-(N-morpholino)propanesulfonic acid
NIPAM	N-isopropylacrylamide
NPs	Nanoparticles
PAA	Polyacrylic acid
PDB	Protein Data Base
PEG	Polyethylene glycol
PLL	Poly-L-Lysine
PNIPAM	Poly(N-isopropylacrylamide)
PS	Polystyrene
PSS	Polystyrene Sulfonate
RET	Resonance Energy Transfer
SANS	Small Angle Neutron Scattering
SAXS	Small Angle X-Ray Scattering
SDS	Sodium dodecyl sulfate

SPB	Spherical Polyelectrolyte Brush
TEM	Transmission Electron Microscopy
VPTT	Volume Phase Transition

## 10 List of Figures

1.1	Protein adsorptions occurring in different technological fields . . . . .	2
1.2	Illustration of the Vroman effect . . . . .	3
1.3	Nanoparticle forming a corona interacting on a cellular level . . . . .	4
1.4	Scheme of a typical protein adsorption isotherm and Langmuir Lattice . . . . .	6
3.1	Scheme of stimuli responsive core-shell microgel with a solid core structure . . . . .	10
3.2	Cryo-TEM image of a negatively charged poly(NIPAM) core-shell microgel . . . . .	10
3.3	Scheme of the two-step synthesis of core-shell microgels . . . . .	11
3.4	Donnan potential and charge regulation . . . . .	12
3.5	Field-emission scanning electron microscope images of positively and negatively charged microgel particles assembled on a mica surface . . . . .	15
3.6	Schematic representation of an isothermal titration calorimeter . . . . .	16
3.7	ITC titration of lysozyme binding to microgel NW15 . . . . .	18
3.8	The shape of ITC curves: Problems and Pitfalls . . . . .	20
3.9	Distribution of $\beta$ -lactoglobulin in SPB and electron density profile as derived from SAXS . . . . .	22
3.10	Scheme of the model used for the calculation of the scattering function of the composite system consisting of a spherical nanoparticle and adsorbed protein. See further explanations in the text . . . . .	24
3.11	General scheme of the fluorescence-based competitive adsorption experiment in the case of a binary protein mixture . . . . .	28
3.12	Simplified scheme of the Cooperative Binding Model (CB-Model) applied in the one-component and multi-component case . . . . .	29
3.13	Sketch of the core-shell microgel in a binary mixture of proteins . . . . .	29
4.1	Adsorption isotherms for cytochrome c onto NW15 and OM5UF microgel particles at different temperatures and van't Hoff plot . . . . .	35
4.2	Adsorption isotherms for cytochrome c and glucosidase onto NW15 microgel particles . . . . .	37
4.4	Heats of dilution for glucosidase measured by ITC . . . . .	38
4.3	SAXS intensity profiles $I(q)$ for Glucosidase . . . . .	39
4.5	Adsorption isotherm for lysozyme onto OM6UF microgel particles . . . . .	40
4.6	Adsorption isotherms of lysozyme, cytochrome c, RNase A and papain onto NW15 microgel particles . . . . .	41

4.7	Analysis of the total free energy . . . . .	42
4.8	Competitive protein adsorption measured with fluorescence spectroscopy . . . . .	44
4.9	Crystal structure of cytochrome c and the normalized adsorption spectrum of an iron foil and for cytochrome c . . . . .	46
4.10	Anomalous dispersion correction by Cromer-Lieberman calculations . . . . .	47
4.11	SAXS curves of the uncharged microgel OM5UF loaded with cytochrome c measured at three different energies and separation of the formfactor for the pure resonant scattering .	48
4.12	Sketch of the 2D microgel with the distribution of cytochrome c and concentration profile of the protein . . . . .	49
4.13	AFM images of OM6UF and OM6UF with lysozyme measured in air . . . . .	50
4.14	AFM images of OM6UF and OM6UF with lysozyme measured in liquid . . . . .	51
4.15	Scheme of a core-shell microgel attached to a PLL modified silicon surface . . . . .	52
6.1	Overview of TEM images of the core-shell microgels . . . . .	58
6.2	Potentiometric and conductometric titrations of microgels . . . . .	59
6.3	UV-vis and fluorescence spectrum of Lysozyme <sup>FITC</sup> . . . . .	61

# 11 List of Tables

3.1	Overview on ITC measurements used to obtain protein adsorption isotherms onto various types of nanoparticles (NPs) . . . . .	17
4.1	Microgels Overview . . . . .	34
4.2	Overview: Protein-microgel combinations for ITC Experiments . . . . .	34
4.3	Thermodynamic parameters for the adsorption of cytochrome c onto microgels NW15 and OM5UF at different temperatures . . . . .	35
4.4	Thermodynamic parameters for the adsorption of cytochrome c and glucosidase . . . . .	36
4.5	Results for the adsorption isotherms of single proteins onto NW15 microgel particles lysozyme, cytochrome c, RNase A and papain using the cooperative binding model . . . .	41
6.1	Overview of the amount of educts used for the synthesis of the polystyrene cores . . . . .	56
6.2	Overview of the amount of educts used for the synthesis of the core-shell microgels . . . .	56
6.3	Composition, size and molecular weight of the shell network of synthesized microgels . .	57
6.4	Overview of ITC parameters used in the experiments . . . . .	60
7.1	Overview of frequently used variables for the derivation of the cooperative binding model	64

## 12 List of Publications and Presentations

Oberle, M.; Yigit, C.; Angioletti-Uberti, S.; Dzubiella, J.; Ballauff, M. Competitive Protein Adsorption to Soft Polymeric Layers: Binary Mixtures and Comparison to Theory. *The Journal of Physical Chemistry B* **2015**, 119, 3250–3258.

Petzhold, A.; Oberle, M.; Lemke, K.; Goerigk G.; Ballauff M. Cytochrome C Adsorption onto Core-Shell Microgels analysed by Anomalous Small-Angle X-ray Scattering. **2016** in preparation

89th ACS Colloid & Surface Science Symposium, Pittsburgh, PA, USA, June 15-17, 2015, Oral presentation: Colloidal Microgels as Model Systems to Study Protein (Ad)sorptions

248th ACS National Meeting and Exposition, San Francisco, CA, USA, August 10-14, 2014, Poster presentation: Competitive Protein Adsorption onto Functional Polymeric Materials predicted by a Multicomponent Binding Model

IRTG 1524 Annual Meeting 2013 New Bern, NC, USA, Sept 29-Oct 03, 2013, Oral presentation: Measuring and Modelling Protein adsorption onto polymeric networks.

HVI-Methodenworkshop, Institut für Biomaterialforschung (HZG Teltow), Teltow, April 30, 2013, Oral Presentation: Small-Angle Scattering with X-Rays and Neutrons: Studying Structures on a Mesoscopic Scale.

# 13 Danksagung

Die Doktorarbeit war für mich ein großes Ziel im Leben, welches durch die Hilfe und Unterstützung anderer Menschen nicht ohne Weiteres zu erreichen wäre.

Ich möchte daher an erster Stelle meinen Dank an Prof. Dr. Matthias Ballauff richten, der es mir ermöglichte auf einem anspruchsvollen, innovativem und interessanten Gebiet zu forschen und dort auch zu neuen Erkenntnissen beizutragen. Insbesondere danke ich Herrn Ballauff für seine Diskussionsbereitschaft und das fortwährende Interesse an meiner Arbeit sowie sein Vertrauen und auch die Flexibilität, die mir für meine Ideen gelassen wurden. Ich habe viel Wichtiges gelernt!

Mein Dank gilt gleichermaßen Prof. Joachim Dzubiella und Dr. Cemil Yigit aus der Theoriegruppe für deren Diskussionsbereitschaft und Vertrauen. Insbesondere bedanke ich mich hier für deren maßgebliche Hilfe bei der Analyse, Interpretation und Vorhersage der experimentellen Daten der kompetitiven Proteinadsorption sowie für die tolle Zusammenarbeit bei der Veröffentlichung. Ferner danke ich Dr. Günther Goerigk und Dr. Albrecht Petzhold für die ASAXS Messzeit und die hervorragende Hilfe bei der Auswertung und Interpretation der Messdaten - auch im Hinblick auf die noch ausstehende Publikation.

Ebenfalls möchte ich mich sehr herzlich bei Prof. Dr. Stefan Zauscher und seinen Mitarbeitern bedanken. Während meines Aufenthalts in dessen Arbeitskreis in den USA habe ich sehr lehrreiche und wertvolle Erfahrung sammeln können. Es war eine unvergessliche und schöne Zeit!

Für die finanzielle Unterstützung danke ich der Deutschen Forschungsgemeinschaft (DFG), in deren Graduiertenkolleg IRTG-1524 ich Stipendiat war und welche mir auch meinen Auslandsaufenthalt ermöglichte. An dieser Stelle möchte ich mich nochmal sehr herzlich bei den Organisatoren und Mitarbeitern des IRTG-1524, namentlich Prof. Dr. Martin Schoen, Dr. Daniela Fliegner, Petra Erdmann und Beatrix Thiele bedanken. Für die Anliegen der Stipendiaten hatten sie stets ein offenes Ohr und wertvolle Ratschläge. Überdies möchte ich ein Dankeschön an das Helmholtz-Zentrum Berlin richten, welches mir eine zusätzliche Finanzierung zur Fertigstellung dieser Arbeit ermöglichte.

Ein weiterer Dank gilt allen meinen Kollegen und Kolleginnen des Helmholtz-Zentrums Berlin, der TU Berlin und der Duke University. Diese haben wesentlich zu einem angenehmen und inspirierenden Arbeitsklima beigetragen.

Ein abschließender und spezieller Dank geht an meine wertvollen Freunde, die mich auch durch schwierige Phasen im Leben begleitet haben.

Denn die richtigen Personen verändern dich nicht, sie verbessern dich!